Shapley-based Utility Allocation and Analytical Uncertainty Management in Power Grids

Zur Erlangung des akademischen Grades eines

Doktors der Ingenieurwissenschaften

von der KIT-Fakultät für Informatik
des Karlsruher Instituts für Technologie (KIT)

genehmigte

Dissertation

von

Rebecca Bauer

Tag der mündlichen Prüfung:	29.01.2026
Hauptreferent:	Prof. Dr. Veit Hagenmeyer
	Karlsruher Institut für Technologie (KIT)
Korreferent:	Prof. Dr. Christoph Weber
	Universität Duisburg-Essen

Kurzfassung

Die Energiewende verändert die Struktur und den Betrieb von Stromversorgungssystemen grundlegend. Der wachsende Anteil erneuerbarer Energiequellen (EEQ), die zunehmende Dezentralisierung der Erzeugung und der damit verbundene Bedarf an überregionaler Koordination stellen neue Anforderungen an die Übertragungsnetzbetreiber (ÜNB). Zwei Herausforderungen stehen dabei im Mittelpunkt: die Unsicherheit der EEQ-Erzeugung im Netzbetrieb angemessen zu berücksichtigen und mehr Transparenz über die Rolle einzelner Netzkomponenten zu schaffen.

Diese Arbeit adressiert beide Herausforderungen mithilfe analytischer Methoden, die auf Optimierung und der kooperativen Spieltheorie basieren.

In Teil I wird ein einfacher, analytisch lösbarer, stochastischer Mehrperioden-Optimaler-Lastfluss (OPF) entwickelt, um zu untersuchen, wie Batterie-Energiespeichersysteme (BESS) die Unsicherheit von EEQ ausgleichen können. Die Unsicherheiten werden mithilfe von Gaußprozessen modelliert. Das Modell wird sowohl an Standardtestnetzen als auch an einem realistischen türkischen Übertragungsnetz validiert.

Teil II widmet sich Transparenz und Erklärbarkeit im Netzbetrieb, ausgehend vom Redispatch-Kontext. Der Shapley-Wert wird auf Stromnetze angewendet, analysiert und erweitert, um seine Einsatzmöglichkeiten im Netzbetrieb systematisch zu untersuchen. Dafür wird der lineare Lastfluss durch ein nichtlineares AC-OPF ersetzt; ein Vergleich zeigt deutliche Unterschiede bei Engpässen und Kosten und unterstreicht die Relevanz des nichtlinearen Modells. Zum Schutz sensibler Daten wird ein verteilter AC-OPF-Algorithmus (basierend auf ALADIN) integriert. Der Shapley-Wert wird anschließend von einem Kostenschlüssel zu

einer allgemeinen Nutzenfunktion verallgemeinert und auf ein multiperiodisches OPF angewendet. Eine Robustheitsanalyse zeigt, dass der Ansatz auch bei Netzänderungen belastbar bleibt. Die stärksten Umverteilungen ergeben sich für Leitungen, gefolgt von Speichern; für Generatoren stimmen Shapley-Wert und Realleistung am besten überein.

Insgesamt bieten die entwickelten Ansätze einfache und zugleich transparente Werkzeuge zur Unterstützung der Netzanalyse, einer fairen Kosten- und Nutzenverteilung sowie einer erklärbaren Netzplanung. Sie zeigen, dass der Shapley-Wert nicht nur zur Allokation von Kosten, sondern auch zur Messung des technischen Einflusses einzelner Komponenten genutzt werden kann, und leisten damit einen Beitrag, ÜNBs bei der Bewältigung der zunehmenden Komplexität und Unsicherheit moderner Stromnetze zu unterstützen.

Abstract

The energy transition is fundamentally reshaping the structure and operation of power systems. The rising share of renewable energy sources (RES), the increasing decentralization of generation, and the resulting need for inter-regional coordination impose new requirements on Transmission System Operators (TSOs). Two central challenges emerge: accounting for RES-induced uncertainty in system operation, and creating greater transparency regarding the role of individual components in the grid.

This thesis addresses both challenges using analytical methods rooted in optimization and cooperative game theory.

In Part I, a simple, analytically tractable, stochastic multi-period Optimal Power Flow (OPF) model is developed to simulate how Battery Energy Storage Systems (BESS) can balance RES uncertainty. The method represents uncertainty using Gaussian processes and is validated on standard test systems as well as a realistic Turkish transmission network.

Part II focuses on transparency and explainability in power system operation, starting from the context of redispatch. The Shapley value is applied to power networks, analyzed, and extended to explore its use in power system analysis systematically. To improve physical realism, the linear power flow is replaced by a nonlinear AC OPF; a comparison shows clear differences in congestion and costs, underscoring the relevance of the nonlinear model. To ensure data privacy, a distributed AC OPF algorithm (based on ALADIN) is integrated. The Shapley value is then generalized from a cost-allocation rule to a utility metric and applied to a multi-period OPF. A robustness analysis shows that the method remains reliable under grid changes. The strongest redistributions occur for transmission

lines, followed by storage, while Shapley values and real power align most closely for generators.

Together, these contributions provide transparent and straightforward tools to support system analysis, fair cost allocation, and explainable grid planning. They demonstrate how the Shapley value can be used not only for cost allocation but also to quantify technical influence, helping TSOs manage the complexity and uncertainty of modern power systems.

Contents

Acronyms and symbols

Acronyms

RES	Renewable Energy Source
QP	Quadratic Program
NLP	Non-Linear Problem
MINLP	Mixed-Integer Non-Linear Problem
PF	Power Flow
OPF	Optimal Power Flow
MP-OPF	Multi-Period Optimal Power Flow
TSO	Transmission System Operator

Indices and sizes

T	Horizon Length
N_b	Number of Buses
N_g	Number of Generators
N_s	Number of Storage Units
N_d	Number of Loads

N_l	Number of Lines
N_d^{RES}	Number of Renewable Energy Sources (RES)
i	Bus
d_i	Load
g_i	Generator
s_i	Storage
g_i^{RES}	Renewable Energy Source (RES) Generator
g_i^{curt}	Curtailment Generator

Sets

$\mathcal{T}$	Set of Time Periods
$\mathcal{N}$	Set of Buses
$\mathcal{G}$	Set of Generators
$\mathcal{L}$	Set of Lines
$\mathcal{S}$	Set of Storage Units
$\mathcal{D}$	Set of Loads
$\mathcal{D}^{RES}$	Set of RES Demands

Deterministic Power Variables

$P_{G,i}, Q_{G,i}$	Active/Reactive Power of Generation at Bus i
$P_{D,i}, Q_{D,i}$	Active/Reactive Power of Demand at Bus i
$P_{S,i}, Q_{S,i}$	Active/Reactive Storage Power (Positive Into the Grid)

$P_{S,i}^{CH}, Q_{S,i}^{CH}$	Active and Reactive Power of Storage Charging
$E_{S,i}$	Storage Energy at Bus i
$\eta_{S,i}^{CH}, \eta_{S,i}^{DC}, \eta_{S,i}^{SDC}$	Storage Charge, Discharge, and Self-Discharge Efficiencies
$P_{Curt,i}, Q_{Curt,i}$	Active/Reactive RES Curtailment at Bus i
F_{ij}	Apparent Power Line Flow From Bus i to Bus j
F_{ji}	Apparent Power Line Flow From Bus j to Bus i
S_{ij}, S_{ji}	Apparent Power Flow S From Bus i to Bus j / From Bus j to Bus i
v_i, θ_{ij}	Voltage Magnitude at Bus i and Angle θ_{ij}

Random Variables

g_i	Random Generator Power at Bus i
d_i	Random Demand at Bus i
d_i^{RES}	Random RES Demand at Bus i
s_i	Random Storage Power at Bus i
e_i	Random Storage Energy at Bus i
p_i	Random Net Power at Bus i (Injection/Withdrawal)
f_{ij}	Random Line Flow on Line $(i,j) = l \in \mathcal{L}$
Ξ	Generic Gaussian Germ

Mean / Variance Decompositions (time-indexed concepts)

$\hat{P}_{G,i}^t, \tilde{P}_{G,i}^t$	Expected and Uncertain Generation at Bus i (Time t)

$\hat{P}^t_{S,i}, \tilde{P}^t_{S,i}$	Expected and Uncertain Storage Dispatch at Bus i (Time t)
$\hat{F}^t_{ij}, \tilde{F}^t_{ij}$	Expected and Uncertain Line Flow for Line (i,j) (Time t)
$\hat{P}^t_{D,i}, \tilde{P}^t_{D,i}$	Expected and Uncertain Demand at Bus i (Time t)
$\hat{P}^{RES,t}_{D,i}, \tilde{P}^{RES}_{D,i}$	Expected and Uncertain RES Demand at Bus i (Time t)

Costs

C	Total Cost
$C_{G,i}$	Generation Cost at Bus i
c_i, b_i, a_i	Generation Cost Coefficients (Constant, Linear, Quadratic)
$C_{Curt,i}$	RES Curtailment Cost at Bus i

Network Parameters

$\mathcal{A}$	Grid
G_{ij}	Line Conductance on Line $(i,j) = l \in \mathcal{L}$
B_{ij}	Line Susceptance on Line $(i,j) = l \in \mathcal{L}$
R_{ij}	Line Resistance on Line $(i,j) = l \in \mathcal{L}$
X_{ij}	Line Reactance on Line $(i,j) = l \in \mathcal{L}$

Limits and Bounds

$\underline{P}_{G,i}, \overline{P}_{G,i}$	Min/Max Active Power Generation at Bus i
$\underline{Q}_{G,i}, \overline{Q}_{G,i}$	Min/Max Reactive Power Generation at Bus i
$\underline{P}_{S,i}, \overline{P}_{S,i}$	Min/Max Active Power Storage at Bus i

$\underline{Q}_{S,i}, \overline{Q}_{S,i}$	Min/Max Reactive Power Storage at Bus i
$\overline{P}^{t}_{Curt,i}$	Max RES Curtailment at Bus i
$\underline{v}_i, \overline{v}_i$	Min/Max Voltage Magnitude at Bus i
$\underline{\theta}_{ij}, \overline{\theta}_{ij}$	Min/Max Voltage Angle at Bus i
$\underline{F}_{ij}, \overline{F}_{ij}$	Min/Max Line Flow on Line $(i,j) = l \in \mathcal{L}$
$\overline{S}_{ij}$	Max Apparent Power Flow on Line $(i,j) = l \in \mathcal{L}$
$\underline{E}_{S,i}, \overline{E}_{S,i}$	Min/Max Storage Energy at Bus i
E_{IC}, E_{BC}	Initial/Boundary Conditions for Storage Energy
$\mathsf{E}_{IC}, \mathsf{E}_{BC}$	Random Initial/Boundary Storage Energy

Game-Theoretic (Shapley)

p	Player
$\mathcal{P}$	Set of Players
Ω	Coalition
Φ	Coalition Cost Function
Ψ	Shapley Value

1 Introduction

As the energy transition proceeds, the structure of the power system is changing fundamentally. Conventional generation is being replaced by wind and solar, while electricity demand increases and large, controllable power plants are giving way to smaller, scattered units and prosumers. This creates a system that is more distributed and subject to more uncertainty. As a result, it is harder to plan, predict, and operate. The backbone of coordination is still the transmission grid, but the role of transmission system operators (TSOs) is becoming more demanding. To maintain stability and efficiency, grid operators need both greater flexibility to respond to variability and more transparency to understand which components or actors influence system behavior and costs. With appropriate models and analytical tools, we can begin to address these needs—coming from the growing uncertain generation and structural complexity.

This thesis addresses two core aspects of modern power system operation. On the one hand, it focuses on the role of flexibility—how resources like battery energy storage systems (BESS) can help stabilize the system under increasing variability and uncertainty and how we can model that. On the other hand, it addresses the growing demand for transparency—asking how to assess and compare the influence of individual components on system behavior and costs. Research questions for both parts are visualized in Figure 1.1. Together, these two perspectives contribute to a deeper understanding of grid flows and provide analytical tools for more informed, targeted decision-making.

Before introducing the technical research gaps, we zoom in on the evolving context of system complexity—from high-level drivers of change to their concrete implications and solution strategies at the grid and operator level.

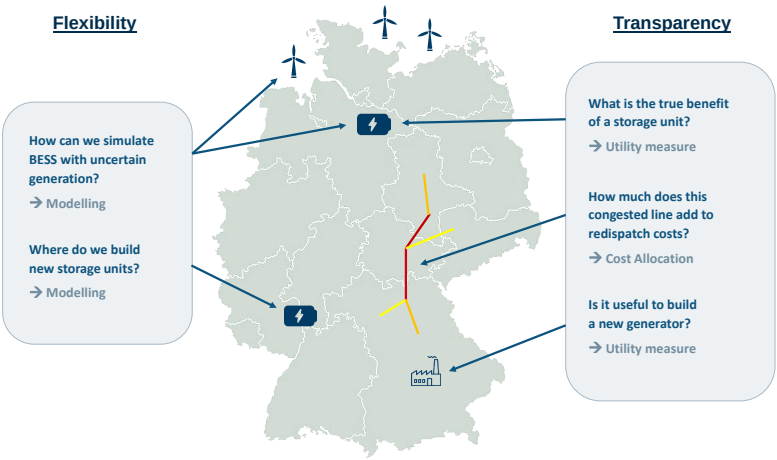

Figure 1.1: Overview of the questions to flexibility and transparency addressed in this thesis.

1.1 Problem Setting

Energy Transition Among the main causes of today's more complex grid conditions is the rapid expansion of renewable energy sources (RES), particularly wind and solar. Policy targets like the Green Deal and REPowerEU, combined with the desire for energy independence from Russian gas, have accelerated the buildout (SIMSON 2023, ENTSO-E 2023). Germany has its own ambitious targets of 80% of RES by 2030 (for Economic Affairs and Climate 2022, BMWK 2023a). In 2023, RES supplied 53.3% of Germany's electricity production—251.2 TWh—and nearly 59% across the EU. While deployment is progressing rapidly, integration is lagging behind since RES are not without challenges: Their volatility, spatial disconnect from load centers, and temporal mismatch with load put stress on the grid. Flexible loads, controllable generation, and grid expansion are not yet scaled to match this change. As a result, system balance must be maintained under increasingly complex conditions.

In Germany, the effects are particularly visible. Wind generation is concentrated in the north, while most load and solar generation lie in the south and west.

Combined with Germany's central role in the European grid, this leads to large cross-country and transit power flows, resulting in frequent congestion and a greater lack of transparency in the power flows. Dealing with this challenge will require not only expanding grid capacity physically, but also developing better tools for monitoring, coordination, and fair cost allocation.

Challenges for Grid Operators The electricity grid is becoming a central actor in the energy transition, and it must evolve alongside it. As the IEA warns, they "are becoming the weak link of clean energy transitions" (International Energy Agency 2023). Increasing shares of renewable generation, the rise of flexible and electrified loads such as electric vehicles and heat pumps, and the growing number of active market participants are putting the grid under more pressure than ever. The most critical issues are the fast-changing, unpredictable power flows and a lack of inherent buffer capacity. What was once passive infrastructure is now a dynamic system that must absorb fluctuations, balance supply and load in real time, and maintain stability under uncertainty. The transmission grid acts as a coordination layer in a system with limited controllability and growing volatility. As a result, grid operators must not only ensure physical stability but also maintain an overview of an increasingly complex and distributed system.

Transmission system operators (TSOs) are at the center of this operational shift. In Germany, four TSOs manage the transmission grid, while nearly 900 distribution system operators (DSOs) handle local power grids, with distinct responsibilities. DSOs handle voltage control and the customer side, including metering, distributed photovoltaic (PV), and electric vehicles (EVs). On the other hand, TSOs are responsible for system stability, long-term planning, market integration, and coordination across regions and countries. As RES grow and inertia from synchronous generators declines, TSOs have to increasingly integrate new actors into markets and improve coordination with DSOs and other TSOs—across national borders in the pan-European grid.

Two challenges are particularly pressing: a lack of flexibility and transparency. First, the grid is so heavily loaded that congestion has become a daily operational issue. Due to a lack in flexibility, redispatch measures are used regularly and at

scale, with €4 billion in costs and 25 TWh of rescheduled energy in 2022 alone (TenneT and TransnetBW 2024). This underlines the need to understand who or what is responsible for specific power flows and resulting costs.

Second, there is a growing issue of limited transparency, which mainly arises from a heavily loaded grid. Even with metering and simulation, it remains difficult to determine which components or actors drive effects such as congestion or losses, particularly in large, meshed networks where interactions are complex and causality is indirect. For operators and regulators, however, such insight is essential. Knowing the influence of individual generators, lines, or storage units enables more informed operational decisions, targeted investments, and better-justified redispatch and tariff structures. As the grid becomes more decentralized and interconnected, explainability at the component level has become a prerequisite for both system operation and regulatory legitimacy.

Strategy for Flexibility The current strategy, however, is grid expansion to simply gain more capacity. To deal with the uncertain and fast-changing power flows introduced by RES, transmission grids need more flexibility. One way to add capacity is to physically expand the grid. Across Europe, over 46,000 km of new transmission lines are planned, with around 6,600 km in Germany alone (50Hertz et al. 2023). Projects like *Suedlink* aim to connect generation in the north with load centers in the south. Although the construction of new lines is necessary, it is often slow, expensive, and comes with regulatory or local opposition. This option offers long-term relief but limited short-term agility.

A more immediate and versatile option for adding flexibility to the grid is battery energy storage systems (BESS). These units can be deployed quickly, scaled modularly, and installed in a wide range of locations. Their rapid response capability makes them well-suited for stabilizing power flows and buffering fluctuations in power, such as from renewable generation. Storage units can also buffer the uncertainty that stems from unpredictable RES generation by providing free capacity and stored electricity. The typical modelling choice for uncertainty is random variables with a deterministic mean plus some variance.

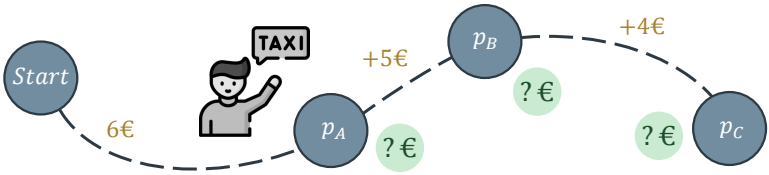

Figure 1.2: The Taxi Game; an example application of the Shapley value.

While BESS are originally used for capacity support and grid boosting, BESS are now being deployed for a growing range of system services, including reactive power control, black-start capability, and congestion relief. In Germany, major projects such as the *grid boosters* are treated as being of "overriding public interest" (BMWK 2023a, Nguyen et al. 2024), and are firmly integrated into national and European grid development plans (ENTSO-E 2020, BMWK 2023b). Large-scale installations (some exceeding 250 MWh) are already under development, and small-scale adoption is growing (TransnetBW 2024, TenneT 2024).

The challenge is no longer about justifying the need for storage, but about determining where and how it can have the greatest system impact. This requires tools that can assess the role of storage in the grid and allow comparisons across different placement and sizing options.

To make the impact of storage interpretable and comparable, across time, location, and configuration, we need metrics that quantify its operational value in a consistent and system-wide way. One such tool, originally developed in cooperative game theory for fair cost sharing, is the *Shapley value*.

Approach for Transparency The Shapley value was initially developed to distribute gains or costs among participants who work together, depending on their individual contributions across all combinations of players. More precisely, it is an allocation rule from cooperative game theory, designed to fairly assign the total cost (or benefit) of a game among individual players based on their marginal contributions to all coalitions. One example game is a shared taxi ride visualized

in Figure 1.2, in which the players have to determine their share of the total ride costs. Individually, every player would pay 6€, 11€, and 15€. Together, the whole ride costs 15€. The question is what the ideal way to share the 15€ is, so that each passenger pays less than getting a taxi for themselves.

What makes the Shapley value particularly appealing is that it satisfies key fairness properties: symmetry, efficiency, null player, and additivity. Originally used in economics, it has since gained traction in fields such as explainable AI and network analysis (Titz et al. 2024, Narayanam and Narahari 2011)—wherever individual contributions in a complex system need to be compared.

In power systems, the Shapley value provides an analytic way to quantify the contribution of individual components, e.g., generators, lines, or storage units, to the overall system performance. Its application is, however, not as wide-spread, and focuses primarily on distribution grids (Varenhorst et al. 2024, Sharma and Abhyankar 2017). More recently, the Shapley value has been introduced for cost allocation in redispatch and congestion management at the transmission level (Voswinkel et al. 2022). This work serves as a starting point for this thesis, which extends the concept beyond cost allocation. In particular, we reinterpret the Shapley value as a broader utility metric—measuring how much individual components contribute to the system's operational behavior. This opens the door to assessing not just who causes costs, but who provides value, and in what context. Such an approach allows us to compare the technical influence of components, such as storage or new grid infrastructure, on system performance, supporting both fairness and transparency in planning and operation.

1.2 Modeling

To apply these tools in realistic power system settings, we require a modeling framework that captures system physics, component constraints, and operational

objectives. This includes both the technical operation of battery storage systems under uncertainty and the evaluation of component influence through cost attribution.

A common analytical approach is to model the power grid as a graph and simulate its behavior using optimization, including all relevant components: generators, loads, transmission lines, RES, and battery storage units. The standard tool for this is the Optimal Power Flow (OPF), which minimizes total generation costs subject to technical constraints, including generator limits, voltage bounds, and line thermal limits. Another standard tool is power flow (PF) to compute power flows given loads and generation by solving a (non-)linear system of equations.

Depending on the desired accuracy, we use DC, AC, or multi-period OPF formulations, and extend them to incorporate uncertainty and storage. To account for distributed actors or privacy constraints, we also implement distributed AC-OPF methods in certain parts. This framework allows us to analyze the system's response to different configurations and to quantify the effect of storage. In addition to standard forms, we propose our own DC stochastic model.

All models are implemented in open-source Julia packages using JuMP.jl and PowerModels.jl. To ensure reproducibility, we provide the whole code, experimental setups, and input data in an open-source package written in Julia.

With this modeling framework, we can now identify the specific research challenges in modeling and analyzing, and outline how this thesis addresses them.

1.3 Contributions

This thesis investigates how to make transmission grids both *more manageable under uncertainty* and *more explainable in operation*. The focus lies on two complementary challenges: On the one hand, we examine Battery Energy Storage Systems (BESS) as a way to provide flexibility for stabilizing power flows. On the other hand, we address the need for *transparency* by applying the Shapley

value to quantify and attribute the influence of individual components in the grid. Together, they respond to a practical challenge for TSOs: the need for models that are tractable enough for operational use, and that support fair, data-informed decision-making.

Part I: Analytical Uncertainty Management Part I asks how BESS should respond to uncertain renewable generation and where they are most effective. Methodologically, we provide a reformulation of a chance-constrained multi-period DC-OPF model. The model includes uncertain RES generation, which is modeled with Gaussian processes. To counteract the uncertainty from RES, we include storage components. To direct the interaction of BESS and generators with the uncertainty, affine policies are used. The resulting model is *tractable* and *analytically exact*. As it is based on DC-OPF, it is simple enough to be used by system operators.

Additionally, faced with grid data scarcity, we build and publish our own 61-bus model of the Turkish transmission grid. This enables an evaluation of how BESS absorbs and reallocate variability to flatten conventional generation profiles and relieve the network in the face of a high share of RES.

In Part I, we answer the following two research questions:

RQ1 *How can we model OPF including uncertainty and BESS in the electricity grid in an analytically exact way?*

→ *Contribution.* We formulate a tractable, analytically exact, chance-constrained multi-period DC-OPF with affine policies under Gaussian uncertainty.

RQ2 *What influence does BESS placement have on managing uncertainty in the grid?*

→ *Contribution.* We use the model mentioned above to quantify how BESS absorbs and reallocates RES uncertainty over time. The approach is validated on standard IEEE cases. We also provide a realistic Turkish transmission grid model and experimentally test various storage locations.

Part II: Transparency through Shapley Part II examines how the Shapley value can be used in transmission grids for *fair cost allocation* and for *transparent, explainable component influence*. We begin with redispatch cost sharing across congested lines and operators, moving from the common DC approximation to the full non-convex AC-OPF.

A first practical challenge is data access. Grid data is distributed across TSOs, and sharing internal models raises privacy concerns. The Shapley workflow, therefore, needs a way to preserve data privacy while keeping allocations stable, motivating a *privacy-preserving distributed AC-OPF*.

A second issue concerns model accuracy. While DC-OPF is widely used for speed, it ignores reactive power and can misrepresent feasible operating points. To ensure fairness, allocations should reflect AC physics. This raises the question of whether DC-OPF-based Shapley calculations are sufficient or whether results change noticeably once full AC-OPF is used.

Beyond redispatch, TSOs also need a principled metric to quantify the operational value of flexibility assets. As BESS deployment grows, simple energy-based indicators fall short, since they ignore network effects and temporal coupling. This motivates extending Shapley from cost sharing to a notion of *component utility* for storage and other devices.

Finally, any metric must withstand real-world variability. Parameters are uncertain, operating points shift, and ideal assumptions do not always hold. The question is how robust the Shapley value remains under such perturbations, and how stable its insights are across changing grid conditions.

These issues boil down to the following four research questions in Part II:

RQ3 *How can we preserve data privacy between grid regions when computing the Shapley value?*

→ *Contribution.* We implement a privacy-preserving distributed AC-OPF (based on ALADIN) within the Shapley workflow to allocate redispatch costs while

preserving data locality across grid partitions. The resulting allocations are consistent and scalable for large meshed networks.

RQ4 *How does the use of AC-OPF affect the results and fairness of the Shapley value compared to DC-OPF?*

→ *Contribution.* We compare the Shapley calculation with AC-OPF against DC-OPF across small and large grids, and show that there are substantial differences in congested lines, redispatch costs, and resulting allocations, underlining that DC is insufficient for cost allocation.

RQ5 *How can the Shapley value be used to quantify the utility of individual BESS units in the transmission grid?*

→ *Contribution.* We adapt the Shapley value to a multi-period AC-OPF including BESS and use it as a utility measure that attributes system cost reduction and other metrics (including effects linked to reactive power) to individual units. We demonstrate its interpretability on a radial and meshed test system.

RQ6 *How robust is the Shapley value in its application to electricity grids in the face of perturbations in grid parameters?*

→ *Contribution.* We perform an experimental robustness analysis. First, we compute the Shapley values of the storage units and alter their own properties. Afterwards, we compute the Shapley values for storage units, generators, and branches, and alter the properties of all grid components with Monte Carlo sampling. We show that the Shapley value changes continuously, and that the perturbations have varying strong effects on different components.

1.4 Outline

This thesis is structured in a fundamentals chapter followed by two parts: Chapter 2 introduces the optimal power flow formulations—DC-OPF, AC-OPF, and MP-OPF —and the BESS model. Part I containing Chapters 3 and 4 answers the

research questions **RQ1** and **RQ2** on the modeling and placement of BESS under Gaussian uncertainty, building on the publications Bauer et al. (2023b, 2022). Part II containing Chapters 7-10 covers the research questions **RQ3-6** and builds on the publications Bauer et al. (2023a, 2024, 2025). The sensitivity analysis in Chapter 10 is yet unpublished.

2 Fundamental Notions for Grid Modeling and OPF

The Optimal Power Flow (OPF) problem constitutes the mathematical foundation of modern grid operation and planning. It enables system operators to determine economically and technically feasible operating points of the power system under a wide range of network and generation constraints. It is a vital instrument for voltage control, generator scheduling, and directing power flows. Thereby, TSOs can ensure efficient operation, reliable supply, and system stability.

OPF is becoming more important with the grid getting more interconnected and complex due to RES, AC-DC coupling and HVDC lines, smart grid applications, and prosumers. Additionally, historically, after the full EU market liberalization in 2009, distribution and transmission grids have been managed separately, when they have to be thought and optimized increasingly combined, especially with the focus shifting from central management to the consumer side in the future. This thesis, however, focuses on transmission grids only.

OPF optimizes the power flows in the electricity grid. There are several optimization goals; mostly, however, generation costs or transmission losses are minimized. When curtailment of RES comes into play, it can be added to the objective as well. The objective is subject to several constraints, amongst them most prominently the Power Flow Equation (PFE) that preserves the balance of load and demand in the grid at every point and, thus, also keeps the frequency stable at 50Hz. Other constraints are the technical limits of all components. Generally, as long as the OPF is feasible, an optimal solution exists, but does not have to be unique.

This chapter successively develops three OPF formulations of increasing complexity and realism: first, the classical nonlinear AC-OPF; second, its linearized DC approximation; and finally, a multi-period AC-OPF that captures temporal coupling effects such as RES variability and storage operation.

The DC-OPF is a linear approximation of AC power flows in high-voltage transmission systems, not a model of direct current (DC) networks. It is used instead of the AC-OPF, especially for large grids when the nonlinear AC-OPF fails to converge or becomes computationally intractable for large-scale systems. While AC-OPF is mostly non-linear and non-convex and, thereby, hard to solve, DC-OPF is easier to solve as it is linear and, thus, convex. Still, DC-OPF solutions are never AC feasible (Baker 2021) as the DC-OPF has very different feasibility regions (Wang and Chiang 2021). The problem also has several equivalent formulations, splitting into rectangular and polar coordinates (Frank and Rebennack 2016). In this thesis, we use the bus injection model, contrary to the branch flow model. The voltage is represented in polar coordinates and the admittance in rectangular form. According to Frank and Rebennack (2016), polar coordinates for the voltage yield fewer variables and fewer nonlinear constraints, although, contrary to rectangular coordinates, they introduce $\sin$ and $\cos$ functions in the power flow equations.

Typical OPF solvers use interior-point or sequential quadratic programming methods for nonlinear AC formulations, while linear or quadratic DC approximations are solved with simplex or interior-point algorithms. There is a manifold of solvers, depending on whether a convex, non-convex, or mixed-integer problem is to be solved (Frank and Rebennack 2016). In this work, the convex DC-OPF is solved using the HiGHS solver, which is integrated via the JuMP optimization framework in Julia. The nonlinear AC-OPF problems are solved using IPOPT, and mixed-integer variants employ Juniper.

This chapter first introduces the grid model, then derives the DC-OPF, gives the AC-OPF, and finally gives the multi-period AC-OPF (MP-OPF). All formulations are based on the book “Power Generation, Operation and Control” (Wood et al. 2014).

Table 2.1: AC-OPF variables.

Variable	Meaning	Unit	Type
$P_{D,i}$	Active power load	MW	Fixed
$Q_{D,i}$	Reactive power load	MVAr	
$V_{slack} = 1$	Voltage magnitude at the slack bus	p.u.	
$\theta_{slack} = 0$	Voltage angle at the slack bus	deg.	
$P_{G,i}$	Active power generation	MW	Free
$Q_{G,i}$	Reactive power generation	MVAr	
F_{ij}	Line flows	MVA	
v_i	Voltage magnitude	p.u.	
θ_i	Voltage angle	deg. (°)	

2.1 Grid Model

The power grid is modeled as a graph $\mathcal{A} = (\mathcal{N}, \mathcal{L})$ with a set of nodes $\mathcal{N} = \{1, \ldots, N_b\}$ and a set of edges $\mathcal{L} = \{1, \ldots, N_l\}$, with cardinalities $N_b = |\mathcal{N}|$ and $N_l = |\mathcal{L}|$. Given the setting of a power system, nodes are called buses, and edges represent lines. Each bus i can contain a load d_i, or a generator g_i. In an extended formulation, a bus can also contain a curtailment generator g_i^{curt} or a storage unit s_i. A line (i, j) from bus i to bus j is typically an AC line or a transformer, depending on the chosen case file.

2.2 OPF Formulations

2.2.1 AC-OPF

In the AC model of power flows, every load and generator has an active and a reactive power component P and Q, respectively. While P performs real work, the reactive power is necessary to create electromagnetic fields that keep the electrical

flows running and, thereby, enable electricity transmission. The variables in the grid are given in Table 2.1. Active and reactive power $P_{D,i}, Q_{D,i}$ for the loads are fixed and have to be met by generation. At the slack bus, the voltage angle θ_i and a voltage magnitude v_i are fixed with $\theta_{slack} = 0$ and $V_{slack} = 1$ p.u. and are free otherwise. Active and reactive power generation $P_{G,i}, Q_{G,i}$ are free, as well as the line flows F_{ij}. Hence, the decision variables are summarized as a vector of vectors $x = (\theta,\, v,\, P_G,\, Q_G)$ with each entry in $\mathbb{R}^{N_b}$. Concerning the type of lines, this formulation assumes no DC lines as they may be included in real grids. The AC-OPF formulation is based on Frank and Rebennack (2016).

Power Flows

The power flows in the grid are derived from the fixed line parameters. Each line has an admittance Y_{ij}, and its reciprocal, the impedance Z_{ij}

$$Y_{ij} = G_{ij} + jB_{ij}, \quad Z_{ij} = R_{ij} + jX_{ij}, \qquad \forall (i,j) \in \mathcal{L}, \tag{2.1}$$

with conductance G_{ij}, susceptance B_{ij}, resistance R_{ij} and reactance X_{ij} (capacitive and inductive) on line (i,j). Given the definition of the power, i.e., $S = V \cdot I^*$ with voltage $V_i = v_i \angle \theta_i$ and current I, we can derive the active and reactive power components as

$$P_{ij} = \; v_i^2 G_{ij} - v_i v_j \left(G_{ij} \cos \Delta\theta_{ij} + B_{ij} \sin \Delta\theta_{ij}\right), \quad \forall (i,j) \in \mathcal{L} \tag{2.2a}$$

$$Q_{ij} = -v_i^2 G_{ij} - v_i v_j \left(G_{ij} \sin \Delta\theta_{ij} - B_{ij} \cos \Delta\theta_{ij}\right), \quad \forall (i,j) \in \mathcal{L} \tag{2.2b}$$

where v_i is the voltage magnitude at bus i, and $\Delta\theta_{ij} = \theta_i - \theta_j$ the voltage angle difference. The active and reactive power equations yield the real and imaginary parts of the apparent power:

$$S_{ij} = P_{ij} + jQ_{ij}, \qquad \forall (i,j) \in \mathcal{L}. \tag{2.3}$$

The absolute line flow is then defined as the Euclidean norm of the apparent power:

$$|F_{ij}| = \sqrt{P_{ij}^2 + Q_{ij}^2}, \qquad \forall (i,j) \in \mathcal{L}. \tag{2.4}$$

In the implementation, these power flows are described by two variables each: the *from-bus* power flow and the *to-bus* power flow, before and after the losses. Since power can flow in both directions, these variables can be positive and negative.

Optimization Problem Formulation

The objective minimizes the total generation cost c given by the sum of the generation costs, over all decision variables $x = (\theta,\, v,\, P_G,\, Q_G)$:

$$\min_x \; c(P) = \sum_{i \in \mathcal{N}} \left(a_i \cdot (P_{G,i})^2 + b_i \cdot (P_{G,i}) + c_i \right), \tag{2.5}$$

with constant, linear, and quadratic cost coefficients c_i, b_i, a_i, respectively. Since the active power P is the usable part of the apparent power, only P is included in the cost function.

The Kirchhoff's laws (Wood et al. 2014) stem from the first law of thermodynamics, representing the concept of preservation of energy, and yield the power flow equations for each bus i and for active and reactive power:

$$P_{G,i} - P_{D,i} = v_i \sum_{j \in \mathcal{N}} v_j \left(G_{ij} \cos \Delta\theta_{ij} + B_{ij} \sin \Delta\theta_{ij} \right), \qquad \forall i \in \mathcal{N} \tag{2.6a}$$

$$Q_{G,i} - Q_{D,i} = v_i \sum_{j \in \mathcal{N}} v_j \left(G_{ij} \sin \Delta\theta_{ij} - B_{ij} \cos \Delta\theta_{ij} \right), \qquad \forall i \in \mathcal{N} \tag{2.6b}$$

saying that the generation $P_{G,i}$ and $Q_{G,i}$ minus the demand $P_{D,i}$ and $Q_{D,i}$ at each bus i must equal the incoming power from the adjacent lines, i.e., $P_{ji} - P_{ij}$ and $Q_{ji} - Q_{ij}$. These equations capture both the electrical and topological structure of the network. These nonlinear relations between voltage magnitudes v_i, voltage

angles θ_{ij}, and the resulting active and reactive power flows are the main source of nonconvexity in the AC-OPF. Consequently, the problem may exhibit multiple local optima, which complicates its numerical solution.

Remaining are the physical limits for all technical components of the power grid. The generators are bounded with a minimum and maximum capacity:

$$\underline{P}_{G,i} \leq P_{G,i} \leq \overline{P}_{G,i}, \qquad \forall i \in \mathcal{N} \tag{2.7}$$

$$\underline{Q}_{G,i} \leq Q_{G,i} \leq \overline{Q}_{G,i}, \qquad \forall i \in \mathcal{N} \tag{2.8}$$

where the minimum limit of the active power $\underline{P}_{G,i}$ is not necessarily zero, e.g., in case the generator supplies the base load, and the minimum limit for the reactive power $\underline{Q}_{G,i}$ can even be negative. The line flows F_{ij} are given limits as well:

$$|F_{ij}| \leq \overline{F}_{ij}, \qquad \forall (i,j) \in \mathcal{L} \tag{2.9}$$

which is often called *Rate A* and is the normal static line rating. Together, equations (2.5) up to (2.9) provide the following nonlinear and nonconvex AC-OPF optimization problem:

$$\begin{aligned} &\min \text{ (2.5)} \\ &\text{s.t. (2.6)} - \text{(2.9)}. \end{aligned} \tag{2.10}$$

2.2.2 DC-OPF

The DC-OPF problem formulation is a much used approximation of the AC-OPF problem given in Equation (2.10). It especially suits well high-voltage grids, as they have fewer losses, which are ignored in the DC-OPF formulation. There are various ways to formulate the DC-OPF, e.g., flow-based, PTDF-based, cycle-based, angle-based (Hörsch et al. 2017). This thesis uses the Kirchhoff-based formulation, as above for the AC-OPF, and as introduced in Frank and Rebennack (2016). The variables are given in Table 2.2 with the active power generation

Table 2.2: DC-OPF variables.

Variable	Meaning	Unit	Type
$P_{D,i}$	Active power load	MW	Fixed
$v_i = 1$ p.u.	Voltage magnitude	p.u.	
$\theta_{slack} = 0$	Voltage angle at the slack bus	deg. (°)	
$P_{G,i}$	Active power generation	MW	Free
F_{ij}	Line flows	MVA	
θ_i	Voltage angle	deg. (°)	

$P_{G,i}$, line flows F_{ij}, and voltage angles θ_i as free variables, and the load $P_{D,i}$ and voltage angle and magnitude at the slack bus fixed.

Derivation

Three assumptions are made to simplify the power flow equations into a linear form. First, line resistance R is neglected, which implies zero conductance $G = 0$ while the reactance X remains, as it defines the line susceptance $B = 1/X$. Second, all voltage magnitudes are fixed to $= 1$ per unit. Third, the trigonometric functions in the power flow equations are linearized by assuming small voltage angle differences. These justify the approximations $\sin(\theta_i - \theta_j) \approx \theta_i - \theta_j$ and $\cos(\theta_i - \theta_j) \approx 1$, which linearize the trigonometric terms in the power flow equations. Together, these assumptions linearize the nonlinear power flow equations and eliminate reactive power, yielding a convex quadratic optimization problem suitable for large-scale transmission networks.

Neglecting line resistance R_{ij} implies zero conductance $G_{ij} = 0$, leaving only the susceptive component of the admittance. Reactive power is ignored, and the power flow equations reduce to:

$$P_{G,i} - P_{D,i} = \sum_{j \in \mathcal{N}} B_{ij} \, (\Delta\theta_{ij}), \quad \forall i \in \mathcal{N} \tag{2.11}$$

with $\Delta\theta_{ij} = \theta_i - \theta_j$. Adding the linear power flow equation (2.11), the complete DC-OPF formulation can be defined. The derivation of the DC-OPF from the AC-OPF is detailed in Zhu (2015) and Wood et al. (2014).

Optimization Problem Formulation

The DC-OPF formulation is, apart from the power flow equations, the same as the AC-OPF, while neglecting reactive power. The objective function minimizes, as previously, the generation costs:

$$\min_P \; c(P) = \sum_{i \in \mathcal{N}} \left(a_i \cdot (P_{G,i})^2 + b_i \cdot (P_{G,i}) + c_i \right). \tag{2.12}$$

The power flow equation are as in Equation (2.11):

$$P_{G,i} - P_{D,i} = \sum_{j \in \mathcal{N}} \left(B_{ij} \cdot \theta_{ij} \right). \qquad \forall i \in \mathcal{N} \tag{2.13}$$

Since there is no reactive power, the line flows reduce to:

$$F_{ij} = P_{ij}. \qquad \forall (i,j) \in \mathcal{L} \tag{2.14}$$

The physical limits reflect the generator limits of active power:

$$\underline{P}_{G,i} \leq P_{G,i} \leq \overline{P}_{G,i}, \qquad \forall i \in \mathcal{N} \tag{2.15a}$$

and the line limits:

$$|F_{ij}| \leq \overline{F}_{ij}. \qquad \forall (i,j) \in \mathcal{L} \tag{2.15b}$$

Equations (2.12) until (2.15) yield the following DC-OPF formulation:

$$\begin{aligned} &\min \text{ (2.12)} \\ &\text{s.t. (2.11)} - \text{(2.15)}. \end{aligned} \tag{2.16}$$

Table 2.3: Multi-period AC-OPF variables.

Variable	Meaning	Unit	Type
$P^t_{D,i}$	Active power load	MW	Fixed
$Q^t_{D,i}$	Reactive power load	MVAr	
$P^{RES,t}_{D,i}$	Active power RES generation	MW	
$Q^{RES,t}_{D,i}$	Reactive power RES generation	MVAr	
$V^t_{slack} = 1$	Voltage magnitude at the slack bus	p.u.	
$\theta^t_{slack} = 0$	Voltage angle at the slack bus	deg. (°)	
$P^t_{G,i}$	Active power generation	MW	Free
$Q^t_{G,i}$	Reactive power generation	MVAr	
$P^t_{Curt,i}$	Active power curtailment	MW	
$Q^t_{Curt,i}$	Reactive power curtailment	MVAr	
$P^{t,CH}_{S,i}$	Storage active power charging	MW	
$Q^{t,CH}_{S,i}$	Storage reactive power charging	MVAr	
$P^{t,DC}_{S,i}$	Storage active power discharging	MW	
$Q^{t,DC}_{S,i}$	Storage reactive power discharging	MVAr	
$E^t_{S,i}$	Storage energy	MWh	
F_{ij}	Line flows	MVA	
v_i	Voltage magnitude	p.u.	
θ_i	Voltage angle	deg. (°)	

Problem (2.16) is linear and convex.

2.2.3 Multi-Period AC-OPF

A Multi-Period OPF (MP-OPF) is necessary whenever system operators want to simulate the grid over time, e.g., for generation scheduling or grid planning. A MP-OPF is especially needed with a high share of RES, since for the security of supply, RES and its uncertainty needs to be forecasted such that generation can be

scheduled. The MP-OPF is based on the AC-OPF with an added time dimension. All variables are optimized over a time horizon $\mathcal{T}$, minimizing the total system costs and connecting the time steps via coupling constraints. This formulation contains RES curtailment. The formulation of the MP-OPF in this thesis is based on Nguyen et al. (2015), Gutermuth and Giuntoli (2020), Dai et al. (2024) and Usman and Capitanescu (2021). All variables are given in Table 2.3.

The objective is similar to Equation (2.5), while the costs are summed over the horizon:

$$c(P^t_{G,i}, P^t_{Curt,i}) = \sum_{t=1}^{T} \sum_{i=1}^{N_b} C_{G,i}(P^t_{G,i}) + C_{Curt,i}(P^t_{Curt,i}), \tag{2.17}$$

where $C_{G,i}$ and $C_{Curt,i}$ are linear or quadratic cost functions, e.g.:

$$C_{G,i}(P^t_{G,i}) = a_i \cdot (P^t_{G,i})^2 + b_i \cdot (P^t_{G,i}) + c_i$$

with constant, linear, and quadratic cost coefficients a_i, b_i, c_i, respectively. This thesis mainly uses linear cost functions for better comprehensibility. The term $C_{Curt,i}$ accounts for the cost of curtailed renewable generation. It penalizes the reduction of available RES output and thereby promotes the use of renewable energy whenever feasible.

The power flow equations hold for every bus i and every point in time t, yielding the active power balance:

$$P^t_{G,i} - P^t_{D,i} = \sum_{j=1}^{N_b} v^t_i v^t_j \left(G_{ij} \cos\theta^t_{ij} + B_{ij} \sin\theta^t_{ij}\right), \qquad \forall i \in \mathcal{N}, \forall t \in \mathcal{T} \tag{2.18a}$$

and the reactive power nodal balance:

$$Q^t_{G,i} - Q^t_{D,i} = \sum_{j=1}^{N_b} v^t_i v^t_j \left(G_{ij} \sin\theta^t_{ij} - B_{ij} \cos\theta^t_{ij}\right), \quad \forall i \in \mathcal{N}, \forall t \in \mathcal{T} \tag{2.18b}$$

where v^t_i and θ^t_{ij} denote the voltage magnitude at bus i and the voltage angle difference on line (i, j) at time t, respectively. As before, the susceptance B_{ij} and conductance G_{ij} represent the real and imaginary parts of the complex admittance Y_{ij}, respectively.

The physical limits for generation are the same as before, only for every time step t:

$$\underline{P}_{G,i} \leq P^t_{G,i} \leq \overline{P}_{G,i}, \qquad \forall i \in \mathcal{N}, \forall t \in \mathcal{T} \tag{2.19a}$$
$$\underline{Q}_{G,i} \leq Q^t_{G,i} \leq \overline{Q}_{G,i}, \qquad \forall i \in \mathcal{N}. \forall t \in \mathcal{T} \tag{2.19b}$$

Constraints (2.19a)–(2.19f) define the technical feasibility region for all components, while equations (2.18) ensure power balance at every time step. The curtailment generators are the only decision variables whose limits change with every time step t since the amount of curtailable RES generation changes:

$$-P^{RES,t}_{D,i} \leq P^t_{Curt,i} \leq 0, \qquad \forall i \in \mathcal{N}. \forall t \in \mathcal{T} \tag{2.19c}$$

The negative sign indicates that curtailment reduces the available RES generation rather than adding new production. The maximum curtailment equals the available RES generation, and since this artificial generator cannot inject power into the grid, its upper limit is set to zero.

The limits for voltage magnitude and the angle differences are as before:

$$\underline{v}_i \leq v^t_i \leq \overline{v}_i, \qquad \forall i \in \mathcal{N}, \forall t \in \mathcal{T} \tag{2.19d}$$
$$\underline{\theta}_{ij} \leq \theta^t_{ij} \leq \overline{\theta}_{ij}, \qquad \forall (i,j) \in \mathcal{L}. \forall t \in \mathcal{T} \tag{2.19e}$$

as are the limits for the power flows:

$$|F_{ij}^t| \leq \overline{F}_{ij}. \qquad \forall (i,j) \in \mathcal{L},\, \forall t \in \mathcal{T} \tag{2.19f}$$

The MP-OPF is given by Equations (2.17) until (2.19):

$$\begin{aligned} &\min \text{ (2.17)} \\ &\text{s.t. (2.18) and (2.19).} \end{aligned} \tag{2.20}$$

Problem (2.20) is nonlinear and nonconvex.

Part I

Analytical Uncertainty Management

Introduction

The shift towards Renewable energy sources (RES) is a vital building block of the energy transition as it reduces fossil electricity generation. However, it also brings the challenge of uncertain generation, making electricity generation less predictable and less controllable.

There are several ways to respond to uncertain generation. Loads can shift their electricity demand to when the wind blows and the sun shines, via demand side management (DSM). System operators can ramp up conventional generators every time when the RES do not produce. What is more difficult, however, is keeping the exact balance between generation and demand at every time step, and hence also keeping the frequency at 50 Hz. Conventional generators cannot be ramped up that quickly, except for gas power plants, which are too expensive for fast control.

An essential strategy for keeping the load and frequency balance is to introduce a buffer that can shift electricity in place and time. Battery energy storage systems (BESS) can provide such a buffer. They can take on excess electricity from RES, and feed it back into the grid during a period of supply shortage. As BESS can charge and discharge electricity quickly without much cost, it is an effective measure to influence the generation and load balance in the grid. Depending on the size of the storage unit and the number of units in the grid, the BESS can cover a short period of several hours. This is, however, just enough for conventional generators to ramp up slowly, or e.g., industrial load to be shifted. In Germany, large-scale BESS integration is well underway, and even small-scale BESS requests exceed expectations.

This part of the thesis focuses on how distributed storage can take on the uncertainty from RES that would otherwise have to be managed by conventional generators and loads, and its effects on conventional generation.

We take on the perspective of the transmission system operators (TSOs). To operate their electricity grids, computing the cost-optimal generation and power flows is an everyday essential task. To do that, the models of the grid on which optimal power flow (OPF) is performed, as well as OPF models themselves, need to be developed further. In the course of current developments, OPF models need to incorporate the stochastic uncertainty from RES (Vrakopoulou and Hiskens 2017, Roald et al. 2013), as well as new components for BESS. Solving a stochastic OPF is generally a difficult task. And for TSOs, this often needs to be done quickly and with increasing precision. This is the gap where this chapter sets in.

There is a growing body of research on uncertainty-aware OPF formulations, including stochastic, robust, and chance-constrained, static and multi-period approaches (Mühlpfordt et al. 2018, Vrakopoulou and Hiskens 2017, Summers et al. 2015). Many of these methods incorporate affine policies to capture how generators or storage units respond to forecast errors (Bucher et al. 2017). However, much of the existing work relies on scenario-based methods or static, single-period formulations that can limit both tractability and interpretability in operational planning.

For the following two chapters, we use the linear DC formulation introduced in Chapter 2 with multiple time periods, as it is used by many grid operators and in literature as a good approximation for AC-OPF for fast computing. The uncertainty from RES is modeled using Gaussian Processes (GPs), which describe distributions over functions and are commonly used to model time series with uncertainty (Schulz et al. 2018). Based on that, we derive an analytical model formulation including stochasticity that can be solved exactly. In the second chapter, we apply this formulation to our newly built Turkish transmission grid to show that it works equally well on a larger, more realistic meshed power grid, and compare several placement strategies for BESS.

3 Analytical Uncertainty Propagation

Publication reference for this chapter

Bauer, R. and Mühlpfordt, T. and Ludwig, N. and Hagenmeyer, V. (2023). "Analytical Uncertainty Propagation for Multi-Period Stochastic Optimal Power Flow". *Sustainable Energy, Grids and Networks (SEGAN)*, vol. 33. DOI: 10.1016/j.segan.2022.100969

The integration of BESS requires good and exact models that can be used to solve an optimal power flow (OPF). Using a DC-OPF formulation, we develop a model that incorporates uncertainty from both renewable energy sources (RES) and BESS components, addressing the following research question:

RQ1 *How can BESS stabilize the electricity generation with a high share of uncertain RES generation in the grid?*

To investigate this question more systematically, we refine it into three sub-questions:

- *What influence does BESS have on the conventional generation?*
- *What influence do variance constraints have on generators?*
- *How does the method scale?*

Additional aspects discussed in the original publication (Bauer et al. 2023b), such as risk[1] sensitivity and the distinction between local and global balancing are omitted here for clarity.

In short, to answer these questions, we formulate a DC stochastic OPF that is initially not analytically solvable, then reformulate it under the assumption of Gaussian processes to make it tractable.

Modeling an OPF with stochastic uncertainty and solving it efficiently is a difficult task. The computational complexity arises not only from the grid size, but also from how uncertainty is represented. Necessarily, there is an inherent trade-off between the richness of the uncertainty model, the exactness of results, and computational speed. In this chapter we opt for analytically exact results by using a simplified, but justified, model for RES uncertainty, while accepting reasonable computational speed.

The central modeling choice is how to represent forecast errors for renewable sources. We model RES uncertainty using Gaussian Processes (GPs). While individual generators can behave non-Gaussian, the spatial and temporal aggregation of many plants typically yields approximately Gaussian profiles due to the central limit theorem (Hemmati et al. 2016). GPs are well-suited for power system time series because they naturally capture temporal and spatial correlations (Mitrentsis and Lens 2021, Roberts et al. 2012). They are also closed under linear transformations, which makes them analytically compatible with the linear structure of DC OPF constraints (Schulz et al. 2018) and thus preserves tractability. Using Gaussian Process Regression (GPR), GPs can be fitted to historical RES data, providing both the predictive mean and covariance that fully characterize the uncertainty and integrate directly into the stochastic OPF.

In addition to the uncertainty model, the formulation in this chapter relies on three further ingredients. First, we use chance constraints that limit the probability of violating physical bounds, in analogy to dynamic line ratings. Second, we employ

[1] This risk is applied to the chance constraints and is not to be confused with the risk of the cost function as in Hemmati et al. (2016).

affine control policies that determine how generators and storage units react to forecast errors. Third, we introduce a multi-period time horizon to model the storage behaviour. The combination of Gaussian uncertainty, affine policies, and a multi-period DC OPF with chance constraints forms the core of the approach.

3.1 Related Work

Previous research has addressed subsets of the aspects considered here, but few combine all elements into a unified and tractable framework.

Several studies investigate multi-period stochastic OPF with Gaussian uncertainty and storage, but often omit chance constraints and instead rely on scenario trees (Hemmati et al. 2016). Other works approximate chance constraints (Summers et al. 2015, Li and Mathieu 2015), which may compromise accuracy.

The concept of an "analytical reformulation" of chance constraints has been explored in earlier work on joint chance constraints, for example, in Liu et al. (2020).

Gaussian processes have been widely used in forecasting applications relevant to power systems, including wind power (Kou et al. 2013, Chen et al. 2014), solar energy (Sheng et al. 2018), and electricity demand (Mori and Ohmi 2008, Leith et al. 2004, Lloyd 2014, Rogers et al. 2011, Blum and Riedmiller 2013, McLoughlin et al. 2013). These studies highlight the suitability of GPs for modeling temporal and spatial correlations, which motivates their use in uncertainty modeling for stochastic OPF.

Exact reformulations of chance constraints have been studied in static settings (Bienstock et al. 2012) and partially extended to power systems without storage (Roald et al. 2013) or affine policies (Sjödin et al. 2012). Some second-order cone formulations exist (Zhang et al. 2017, Xie and Ahmed 2018), but they too are either static, omit storage, or use a different class of constraints (Warrington et al. 2013).

Table 3.1: Data and test grids for Chapter 3.

Data Type	Details
Grids	IEEE 5, 39, 57, 118, 300-bus
Time Series	ENTSO-E Wind Generation Data (2014-2021), *Northwind* (De Felice 2021), synthetic wind & load data

Affine policies have been used in reserve planning (Ding et al. 2016, Bucher et al. 2017), distribution grids (Fabietti et al. 2017, 2018), and stochastic OPF (Vrakopoulou et al. 2013, Louca and Bitar 2016, Munoz-Alvarez et al. 2014). However, these works typically lack a multi-period treatment, storage integration, or do not provide an exact analytical reformulation of chance constraints.

Uncertainty propagation techniques such as scenario-based methods and Monte Carlo sampling (Capitanescu et al. 2012, Fabietti et al. 2017, Vrakopoulou and Hiskens 2017), as well as Polynomial Chaos Expansion (PCE) (Mühlpfordt et al. 2016, 2017, 2018), can be computationally expensive and may lack analytical traceability. Robust and distributionally robust approaches avoid distributional assumptions, but typically yield more conservative solutions.

In summary, this thesis provides a unified and tractable multi-period chance-constrained DC stochastic OPF framework that brings together three elements rarely combined in existing work: Gaussian uncertainty modeling, distributed energy storage, and affine control policies. By integrating these components into a single analytical formulation, the approach addresses a gap in the literature and enables a more realistic and scalable treatment of uncertainty in power system operation.

3.2 Methodology

Analyzing uncertainty in power systems over time requires a multi-period stochastic OPF formulation. However, directly including chance constraints in such a

model often makes it computationally intractable. To obtain a tractable formulation, we rely on the DC approximation of the AC-OPF, which is well-established for high-voltage transmission systems (Wood et al. 2014). We build on the analytical reformulation of chance constraints for static DC-OPF (Bienstock et al. 2012) and its extension to storage in (Mühlpfordt 2020), and generalize it to a multi-period setting as a second-order cone program (SOCP) that is both exact and tractable.

The uncertainty is modeled through Gaussian Processes, using GPR to obtain predictive means and covariances. The GP structure is preserved under the linear operators of the DC OPF, which enables all uncertain quantities—generation, storage power, nodal injections, and line flows—to be described by affine transformations of a Gaussian vector, which again is Gaussian. This allows the chance constraints to be expressed in closed form, leading to a second-order cone program (SOCP).

To handle forecast errors produced by GPR (Schulz et al. 2018), the decision variables of generators and storage units react to RES generation with affine control policies, which are linear functions (matrices). Affine policies are simple to implement, preserve the feasibility of power balance in every realization, and ensure that the power balance constraints decompose nicely across the time steps (Mühlpfordt et al. 2018).

The multi-period formulation captures storage charging, discharging, and energy dynamics, while chance constraints enforce that thermal limits, voltage angle limits, and storage bounds are satisfied with high probability.

The key contribution of this methodology is the integration of Gaussian uncertainty modeling, affine control policies, and multi-period chance-constrained DC OPF into a unified, fully analytical, and tractable optimization framework, which simultaneously incorporates probabilistic forecasts, uncertainty modeling, distributed energy storage, and a multi-period OPF formulation.

Figure 3.1 summarizes the model inputs and outputs. The formulation allows variance constraints to be imposed and the locations of uncertain generation and

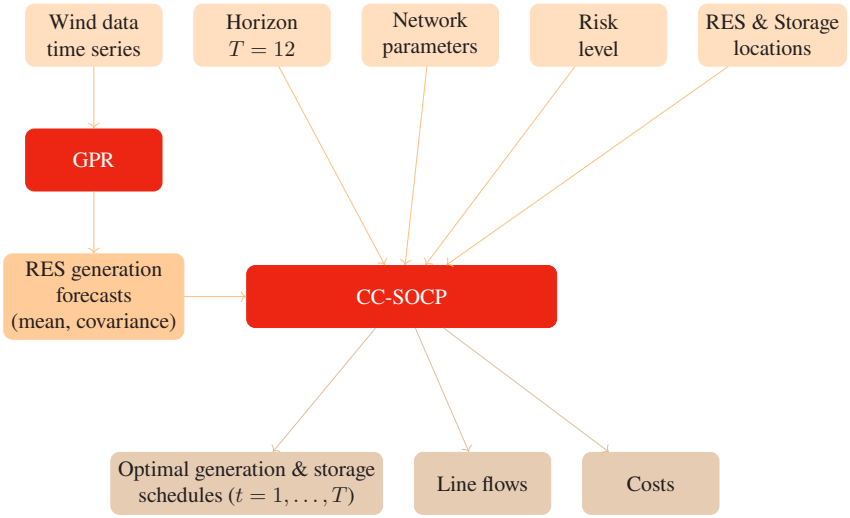

Figure 3.1: Inputs and Outputs of the CC-SOCP model with Gaussian Processes (GPs) forecasted with Gaussian Process Regression (GPR) (Bauer et al. 2022).

storage units to be specified. Solving the resulting chance-constrained second-order cone problem (CC-SOCP) yields optimal generation schedules, storage operation, line flows, and total generation costs.

Model

Following the notation in Section 2.1, the power grid is represented as a graph $\mathcal{A} = (\mathcal{N}, \mathcal{L})$, where $\mathcal{N}$ denotes the set of buses and $\mathcal{L}$ the set of transmission lines. Each bus $i \in \mathcal{N}$ can host various components: a fixed deterministic load $d_i, i \in \mathcal{D}$, a stochastic renewable energy source (RES) injection $d_i^{RES}, i \in \mathcal{D}^{\text{RES}}$ (modeled as a negative load), a conventional generator $g_i, i \in \mathcal{G}$, or a storage unit $s_i, i \in \mathcal{S}$. To reduce modeling complexity, we assume that each bus contains either a RES unit or a storage device, but not both simultaneously. This simplification does not limit the applicability of the model to the test systems considered and helps keep the formulation structurally straightforward.

Note: Both generators and storage units are treated as *stochastic decision variables*. While their operational setpoints are determined by the OPF solution, their actual outputs depend on how they respond dynamically to fluctuations in renewable generation. This distinction is critical in a stochastic framework: generators adjust to balance system variability, while storage units provide localized buffering to partially offset RES uncertainty at their respective buses. Thus, all controllable devices actively contribute to managing the variability introduced by stochastic renewable generation.

The basic OPF formulation for minimizing generation costs without any uncertainty is formulated as the following optimization problem:

$$
\begin{aligned}
\min_{\mathbf{g}_i(t),\mathbf{s}_i(t)} \; & \sum_{t\in\mathcal{T}}\sum_{i\in\mathcal{N}} C(P_{G,i}(t)) \\
\text{s.t.} \; & \sum_{i\in\mathcal{N}} P_{D,i}(t) + P_{G,i}(t) + P_{S,i}(t) = 0 \\
& E_{S,i}(t+1) = E_{S,i}(t) - h\,P_{S,i}(t),\; E_{S,i}(1) = E_{S,i}^{\text{ic}} \\
& \mathbb{P}(x(t) \le \overline{x}) \ge 1-\varepsilon,\; \mathbb{P}(x(t) \ge \underline{x}) \ge 1-\varepsilon \\
& 0 \le \sqrt{\mathbb{V}(x)} \le \sigma_{\overline{x}} \\
& \forall\, x \in \{F_{ij}, P_{G,i}, \Delta P_{G,i}, E_{S,i}, P_{S,i}\}
\end{aligned}
$$

$\forall i \in \mathcal{N}, t, \tau \in \mathcal{T}$, where $P_{G,i}, P_{D,i}, P_{S,i}$, and $E_{S,i}$ are active power variables, $\Delta P_{G,i}$ is the generation ramping constraint, and F_{ij} the line flows. Since RES generation contains uncertainty, we need to reformulate all variables into stochastic random variables. We do that with Gaussian processes because their distributional form is preserved under linear transformations. We reformulate as follows.

Variables as Gaussian Processes To model this uncertainty over time, we use GPs. There are many types of random variables to model stochasticity. GPs are especially suitable for our use case due to two reasons: They are simple, with only mean and variance as parameters, and this parameterization is preserved under linear transformations (Schulz et al. 2018). As such, they are flexible tools

for representing time series with probabilistic structure. Hence, all stochastic variables are modeled as Gaussian processes (Schulz et al. 2018):

$$\mathsf{p}(t) \sim \mathcal{GP}(\mu, \Sigma),$$

denoted by the random variable p, where $\mu = \mathbb{E}(\mathsf{p})$ denotes the mean vector, and $\Sigma = \mathbb{V}(\mathsf{p})$ the covariance matrix. In practice, Σ can be obtained by discretizing a continuous covariance function $k(t, t'), t \in \mathcal{T}$ defined over the time horizon $\mathcal{T}$. This is justifiable since forecasted Gaussian processes are typically continuous in time, and k captures the temporal correlation structure of the process.

To model uncertainty over time, we represent each stochastic variable as a Gaussian process p with a given mean vector $\hat{P}$ and covariance matrix Σ. To ensure a *causal* structure—i.e., where current values depend only on past and current noise—we apply a Cholesky decomposition $\Sigma = \Sigma^L {\Sigma^L}^\top$ and use the *lower-triangular* matrix Σ^L to generate the noise term with causal temporal dependence. This results in a process of the form:

$$\mathsf{p}(t) \sim \mathcal{GP}(\hat{P}, \tilde{P}) \quad \text{with} \quad \tilde{P} := \Sigma^L \Xi,\ \Xi \sim \mathcal{N}(0, I),$$

where $\tilde{P}$ is a zero-mean correlated noise vector. To improve numerical stability, a small positive multiple of the identity matrix (e.g., $10^{-7} I$) is added to Σ before decomposition if necessary (a technique known as *whitening*). The Gaussian process p is modeled as:

$$\mathsf{p} = \hat{P} + \sum_k [\tilde{P}]_k \, [\Xi]_k,$$

or written with an added time dimension as

$$\mathsf{p}(t) = \hat{P}^t + \sum_{k=1}^{t} [\tilde{P}^t]_{tk} \, [\Xi]_k, \quad t \in \mathcal{T}$$

with mean $\mu = \hat{P}^t$, covariance $\Sigma^L = \sum_{k=1}^{t} [\tilde{P}^t]_{tk}^2$, and the stochastic germ $\Xi \sim \mathcal{N}(0, 1)$.

Following this form, a RES load d_i^{RES} is then described as the GP $\{\mathsf{d}_i^{\mathrm{RES},t} \forall t \in \mathcal{T}\}$ with

$$\mathsf{P}_{D,i}^{RES}(t) = [\hat{P}_{D,i}^{RES,t}] + \sum_{k=1}^{t} [\tilde{P}_{D,i}^{RES,t}]_{tk} \, [\Xi]_k, \quad t \in \mathcal{T} \tag{3.1}$$

for all buses $i \in \mathcal{N}$ where $\hat{P}_{D,i}^{RES,t} \in \mathbb{R}^T$ is the mean and $[\tilde{P}_{D,i}^{RES,t}]_{tk}^2 \in \mathbb{R}^{T \times T}$ the covariance.

With the optimization goal of minimizing generation cost and thus using as much RES generation as possible, conventional generation and storage are the two decision variables. As RES generation is stochastic, generation and storage need to be stochastic as well. Hence, we also write them as realizations of (affine) random processes $\{\mathsf{g}_i(t) \forall t \in \mathcal{T}\}$ and $\{\mathsf{s}_i(t) \forall t \in \mathcal{T}\}$. To react to the uncertainty of RES loads, we introduce affine policies that yield feedback of the form

$$\mathsf{g}_i(t) = \hat{P}_{G,i}^t + \sum_{j \in \mathcal{N}} \tilde{P}_{G,i}^t \, \Xi_j \tag{3.2}$$

and

$$\mathsf{s}_i(t) = \hat{P}_{S,i}^t + \sum_{j \in \mathcal{N}} \tilde{P}_{S,i,j}^t \, \Xi_j, \tag{3.3}$$

respectively. Note that the feedback is causal, as they cannot react to future uncertainties.

The fixed load d_i has no covariance, i.e., $\Sigma = 0$, and hence reduces to $\mathsf{d} = \mathcal{GP}(P_{D,i}, 0)$ with $\mathsf{d}_i(t) = \hat{P}_{D,i}^t$.

With all variables modeled as Gaussian processes, the net power of bus i then sums up to

$$\mathsf{p}_i(t) = \mathsf{d}_i(t) + \mathsf{d}_i^{\mathrm{RES}}(t) + \mathsf{g}_i(t) + \mathsf{s}_i(t). \quad \forall t \in \mathcal{T} \tag{3.4}$$

Note that the net power implicitly contains the voltage angles ϕ_i, [2]

The mapping between the power injections $\mathsf{p}_i, i \in \mathcal{N}$, and line flows $\mathsf{f}_l, l \in \mathcal{L}$, in a DC setting can be expressed by the Power Transfer Distribution Factor (PTDF) $\Phi : \mathbb{R}^{N_b} \to \mathbb{R}^{N_l}$ as

$$\mathsf{f}_{ij}(t) = \Phi_{ij} \cdot \mathsf{p}_i(t). \tag{3.5}$$

Furthermore, we can derive the equation for the generation ramping constraints from the definitions of generation in Equation (3.2) as

$$\Delta \mathsf{g}_i(t) = \mathsf{g}_i(t) - \mathsf{g}_i(t-1), \tag{3.6}$$

From Equation (3.3), we can derive the storage state as the discrete-time integrator

$$\mathsf{e}_i(t+1) = \mathsf{e}_i(t) - h \cdot \mathsf{s}_i(t), \tag{3.7}$$

with initial condition $\mathsf{e}_i(1) = \mathsf{E}_{IC}$ and $h > 0$ as the discretization time interval. Thereby, (+/-)$\mathsf{s}_i(t)$ is the discharge/charge of the storage unit $i \in \mathcal{S}$ from time t to $t+1$. Additionally, we assume that storage systems have a prescribed final state $\mathsf{e}_i(T)$. For simplicity, we do not use different variables or efficiencies for charging and discharging in this setting.

Objective function The objective function of the optimal power flow problem is the quadratic generation cost

$$C_i(\mathsf{g}_i(t)) = \gamma_{i,2}\mathsf{g}_i(t)^2 + \gamma_{i,1}\mathsf{g}_i(t) + \gamma_{i,0}, \quad \forall i \in \mathcal{N}$$

[2] This becomes visible with the Kirchhoff Current Law (KCL) (Hörsch et al. 2017): $p_i = \sum_{l=1}^{N_l} K_{il} f_l$ with line flows $f_l = \frac{1}{x_l} \sum_i K_{il}\phi_i, \quad \forall l \in \mathcal{L}$ where x_l is the reactance and $K \in \mathbb{R}^{N_b \times N_l}$ the incidence matrix.

with $\gamma_{i,2} > 0$ and $\gamma_{i,2}, \gamma_{i,1}, \gamma_{i,0} \in \mathbb{R}$ and the stochastic variable g_i. We assume that there is no cost for storage use. To obtain a deterministic scalar value, we take the expected value, i.e.,

$$\mathbb{E}(C_i(\mathsf{g}_i(t))) = C_i(\mathbb{E}(\mathsf{g}_i(t))) + \gamma_{i,2}\mathbb{V}(\mathsf{g}_i(t)). \tag{3.8}$$

Constraints The central constraint of the optimal power flow problem is the power balance equation

$$\sum_{i \in \mathcal{N}} \mathsf{p}_i(t) = 0, \quad \forall t \in \mathcal{T}$$

which splits nicely into the mean and covariance equations (Mühlpfordt et al. 2018)

$$\begin{aligned} &\sum_{i \in \mathcal{N}} (\hat{P}^t_{D,i} + \hat{P}^t_{G,i} + \hat{P}^t_{S,i}) = 0^{\mathcal{T}}, \\ &\tilde{P}^t_{D,j} + \sum_{i \in \mathcal{N}} \tilde{P}^t_{G,i} + \tilde{P}^t_{S,i} = 0^{\mathcal{T}\times\mathcal{T}}. \quad \forall j \in \mathcal{N} \end{aligned} \tag{3.9}$$

Remaining technical constraints, such as generator limits and line capacities, are written as chance constraints of the form

$$\begin{aligned} \mathbb{P}(\mathsf{x}(t) \leq \overline{x}) &\geq 1 - \varepsilon, \\ \mathbb{P}(\mathsf{x}(t) \geq \underline{x}) &\geq 1 - \varepsilon, \end{aligned} \tag{3.10}$$

with the stochastic variables $\mathsf{x} = \mathsf{f}_{ij}, \mathsf{g}_i, \Delta\mathsf{g}_i, \mathsf{e}_i, \mathsf{s}_i$ and the risk factor $\varepsilon \in (0, 0.1]$ set to 0.05. Additionally, we can constrain the standard deviation with

$$0 \leq \sqrt{\mathbb{V}(\mathsf{x})} \leq \Sigma_{\overline{\mathsf{x}}}. \tag{3.11}$$

Reformulating the chance constraints Combining equations (3.1)-(3.11) yields a stochastic DC-OPF, albeit one that is not yet tractable due to several reasons: with random processes, the dimension of the equality constraints is infinite, and integrals are required to solve the chance constraints and cost function.

To make it tractable, we apply the reformulation of the chance constraints by Bienstock et al. (2012): For a Gaussian random variable x with mean μ and standard deviation $\sigma = \sqrt{\mathbb{V}(\mathsf{x}(t))}$ with $\mathbb{V}(\mathsf{x}(t)) = \sum_{k=1}^{t} [\Sigma^L]_{tk}^2$, the chance constraint $\mathbb{P}(\mathsf{x} \leq \bar{x}) \geq 1 - \varepsilon$ in Equation (3.10) is equivalent to the deterministic constraints

$$\begin{aligned} \mu + \lambda(\varepsilon)\sigma &\leq \bar{\mathsf{x}}, \\ \underline{\mathsf{x}} &\leq \mu - \lambda(\varepsilon)\sigma, \end{aligned} \tag{3.12}$$

where $\lambda(\varepsilon) = \Psi^{-1}(1-\varepsilon)$ and Ψ is the standard normal cumulative distribution function (CDF) and $\underline{x}, \bar{x}$ the lower and upper bound of variables $\mathsf{x} = \mathsf{f}_{ij}, \mathsf{g}_i, \Delta\mathsf{g}_i, \mathsf{e}_i, \mathsf{s}_i$. Equation (3.11) can be reformulated analogously.

Optimization problem Equations (3.1)-(3.12) finally yield the second-order cone problem (SOCP) formulation:

$$\begin{aligned} \min_{\hat{P}^t_{G,i}, \tilde{P}^t_{G,i}, \hat{P}^t_{S,i}, \tilde{P}^t_{S,i}, F^t_{ij}} \quad & \sum_{t\in\mathcal{T}} \sum_{i\in\mathcal{N}} \left(C_i(\mathbb{E}(\mathsf{g}_i(t))) + \gamma_{i,2}\mathbb{V}(\mathsf{g}_i(t))\right) \\ \text{s.t.} \quad & \sum_{i\in\mathcal{N}} (\hat{P}^t_{D,i} + \hat{P}^t_{G,i} + \hat{P}^t_{S,i}) = 0^{\mathcal{T}}, \\ & \tilde{P}^t_{D,j} + \sum_{i\in\mathcal{N}} \tilde{P}^t_{G,i} + \tilde{P}^t_{S,i} = 0^{\mathcal{T}\times\mathcal{T}}, \\ & \mu + \lambda(\varepsilon)\sqrt{\Sigma^2} \leq \bar{\mathsf{x}}, \\ & \underline{\mathsf{x}} \leq \mu - \lambda(\varepsilon)\sqrt{\Sigma^2}, \\ & \forall \mathsf{x} \in \{\mathsf{f}_{ij}, \mathsf{g}_i, \Delta\mathsf{g}_i, \mathsf{e}_i, \mathsf{s}_i\} \end{aligned} \tag{3.13}$$

$\forall i, j \in \mathcal{N}, (i,j) \in \mathcal{L}, t \in \mathcal{T}$, with x as the line flows f_{ij}, generation g_i, generation ramping $\Delta\mathsf{g}_i$, storage state e_i, and storage injections s_i.

Formulation (3.13) is convex, tractable, and analytically exact (Bauer et al. 2022). Table 3.2 compares the optimization problem before and after the reformulation.

Table 3.2: Comparison of original intractable Problem and the tractable SOCP (3.13).

	Formulation (3.1)-(3.11)	Reformulation (3.13)
Problem type	No SOCP	SOCP
# constraints	Infinite	Finite
Solve CCs	Integral	Exact formulation
Variables	Random process	Gaussian process
Convexity	Not convex	Convex
Tractability	**No**	**Yes**

Data

The method is applied to several standard IEEE test systems ranging from 5 to 300 buses (see Table 3.1). Renewable generation data is generated synthetically as well as derived from historical wind power time series of the *Northwind* wind farm from the ENTSO-E dataset (De Felice 2021), containing the years 2014 to 2021. Synthetic data enables better explainability and control during testing, while real-world data enables validation in realistic scenarios.

Synthetic data Synthetic load and RES profiles are created using a simple sinusoidal mean and a fixed variance matrix:

$$-\hat{P}^t_{D,i} = P^{\text{nom}}_{D,i}\left(1 + 0.1 \cdot \sin\left(\frac{2\pi(t-1)}{T}\right)\right), \quad \forall i \in \mathcal{N} \tag{3.14a}$$

$$-\tilde{P}^t_{D,i} = \begin{cases} L_i \text{ from (3.18)}, & \forall i \in \mathcal{D}, \\ 0_{T\times T}, & \text{otherwise}, \end{cases} \tag{3.14b}$$

where $P^{\text{nom}}_{D,i}$ is the nominal load from the case files and $\tilde{P}^t_{D,i}$ is given by the lower-triangular matrix L_i in (3.18). The minus sign reflects the modeling convention of loads as negative injections. RES data is constructed analogously.

$$L_i = 10^{-4} \cdot \begin{bmatrix} 87 & 0 & 0 & 0 & 0 & 0 & 0 & 0 & 0 & 0 & 0 & 0 \\ 176 & 20 & 0 & 0 & 0 & 0 & 0 & 0 & 0 & 0 & 0 & 0 \\ 292 & 60 & 7 & 0 & 0 & 0 & 0 & 0 & 0 & 0 & 0 & 0 \\ 434 & 124 & 26 & 3 & 0 & 0 & 0 & 0 & 0 & 0 & 0 & 0 \\ 594 & 211 & 63 & 13 & 3 & 0 & 0 & 0 & 0 & 0 & 0 & 0 \\ 764 & 321 & 123 & 31 & 13 & 3 & 0 & 0 & 0 & 0 & 0 & 0 \\ 937 & 447 & 208 & 63 & 32 & 11 & 3 & 0 & 0 & 0 & 0 & 0 \\ 1103 & 582 & 317 & 109 & 65 & 27 & 10 & 3 & 0 & 0 & 0 & 0 \\ 1257 & 718 & 447 & 172 & 116 & 55 & 26 & 10 & 3 & 0 & 0 & 0 \\ 1392 & 847 & 591 & 251 & 184 & 98 & 53 & 26 & 10 & 3 & 0 & 0 \\ 1504 & 964 & 741 & 342 & 271 & 156 & 94 & 53 & 24 & 9 & 3 & 0 \\ 1590 & 1063 & 889 & 441 & 371 & 229 & 151 & 94 & 50 & 24 & 9 & 3 \end{bmatrix} \tag{3.18}$$

Real-world data: Gaussian Process Regression Real-world load and RES forecasts are obtained using Gaussian Process Regression (GPR), resulting in a Gaussian Process $\mathsf{d}_i = \mathcal{GP}(\mu, k)$ for each bus $i \in \mathcal{N}$, where μ is the mean and $k(t, t')$ the covariance kernel function over the time horizon $\mathcal{T}$. This function is later discretized into the covariance matrix Σ.

The kernel function used for GPR is set up of cosine, squared exponential (RBF), and constant functions:

$$k = k_{\text{cosine}} + k_{\text{RBF}} + k_{\text{constant}}.$$

The individual kernel functions are:

$$k_{\text{cosine}}(x, x') = \sigma_1^2 \cos\left(2\pi \sum_i \frac{(x - x')}{l_1}\right), \tag{3.15}$$

$$k_{\text{RBF}}(x, x') = \sigma_2^2 \exp\left(-\frac{(x - x')^2}{2l_2^2}\right), \tag{3.16}$$

$$k_{\text{constant}}(x, x') = \sigma_3, \tag{3.17}$$

with hyperparameters $\sigma_i \in \mathbb{R}$ representing the variance and $l_i \in \mathbb{R}$ the lengthscale, which controls periodicity and smoothness (Duvenaud 2014). The matrix L_i defines the time-correlated variance structure for each load or RES profile.

An example forecast based on the ENTSO-E dataset (De Felice 2021) is shown in Figure 3.2. A rolling window of 5 hours is used to smooth the prediction, which

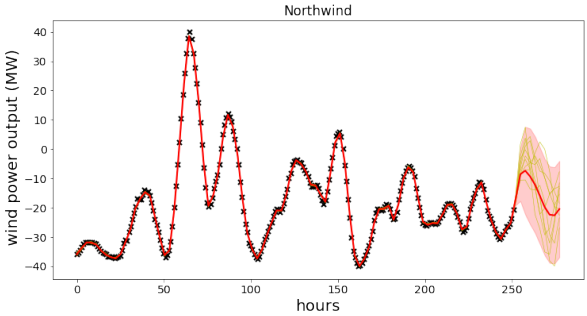

Figure 3.2: GPR-fitted and forecast wind power outputs smoothed with a rolling window of 5 hours.

illustrates typical daily variability in wind profiles. Note that the values are scaled to fit the kernels and are scaled back to only positive values afterwards.

3.3 Experiments

The proposed model in (3.13) is tested using both synthetic and real-world data on a variety of IEEE test grids. We begin with case5 to explore the dynamics of storage and uncertainty, followed by scalability tests on larger synthetic grids. In the next section, the model is further evaluated on a real-world transmission grid.

IEEE 5-bus test case

To evaluate the role of storage in mitigating uncertainty from renewable energy sources, we consider three scenarios:

- (S1) *No storage*,
- (S2) *With storage*,
- (S3) *With storage and variance constraints on generation*.

We compare the system behavior using both synthetic data for better interpretability and predicted RES time series based on Gaussian Process Regression (GPR).

Table 3.3: Parameter settings for the IEEE 5-bus system.

Type	Parameter	Values	
Generation $\forall i \in \mathcal{G}$	Active power limits	$\underline{P}_{G,i} = 0.0$	$\overline{P}_{G,i} = 1.1 P_{G,i}^{\max}$
	Ramping limits	$\Delta\underline{P}_{G,i} = \text{-}0.15 P_{G,i}^{\max}$	$\Delta\overline{P}_{G,i} = 0.15 P_{G,i}^{\max}$
	Cost coefficients	$\gamma_{i,2} = 0.01$, $\gamma_{i,1} = 0.3$, $\gamma_{i,0} = 0.2$	
Storage $\forall i \in \mathcal{S}$	Capacity limits	$\underline{E}_i = 0.0$	$\overline{E}_i = 6.0$
	Active power limits	$\underline{P}_{S,i} = \text{-}10.0$	$\overline{P}_{S,i} = 10.0$
	Initial condition	$\mathbb{E}(\mathsf{E}_i^{\text{ic}}) = 2.0$	$\mathbb{V}(\mathsf{E}_i^{\text{ic}}) = 0.0$
	Border limits	$\underline{E}_{S,i}^{T} = 0.19$	$\overline{E}_{S,i}^{T} = 0.21$

System Setup The test network consists of 5 buses and 6 transmission lines. We modify the topology by placing loads at buses $\mathcal{D} = \{2, 3\}$, a wind farm (RES) at bus $\mathcal{D}^{\text{RES}} = \{4\}$, a storage at bus $\mathcal{S} = \{5\}$, and generators at buses $\mathcal{G} = \{1, 4\}$. Due to modeling requirements allowing at most one generator per bus, generators 1 and 2 have been merged by summing their capacities, and generator 5 is replaced by a storage unit. Minor adjustments to cost coefficients and line ratings were also made (see Table 3.3).

To limit fluctuations in generation, we impose variance constraints on generator outputs:

$$\sqrt{\mathbb{V}(\mathsf{g}_{\mathsf{i}_i}(t))} \leq 0.01, \quad \forall t \in \mathcal{T} \tag{3.19}$$

which corresponds to scenario (S3).

Results

Figure 3.3 illustrates the network state at time $t = 6$, a representative point where storage is nearly fully charged. In scenario (S2), the storage injects a significant

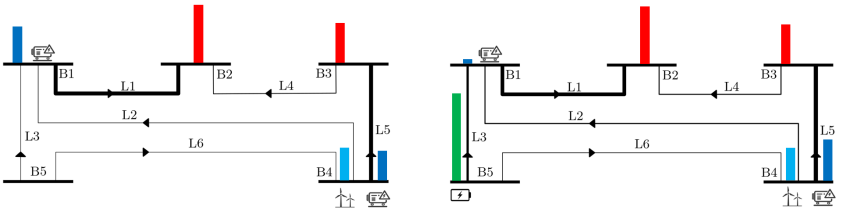

(a) Without storage.

(b) With storage.

Figure 3.3: IEEE case5: Network state without (upper) and with (lower) storage at time $t = 6$, with generation (dark blue), wind generation (light blue), loads (red), storage (green) and line flows (black).

amount of power, effectively offsetting generation from g_1, and demonstrating the storage's ability to shift energy temporally.

Figures 3.4a and 3.5a present the load profiles along with their corresponding uncertainty bands (shaded areas). In the synthetic case, the uncertainty is smooth and predictable, allowing generators and storage to respond in a more uniform manner. In contrast, the real-world forecast shows more volatility and a larger uncertainty over time, imposing a bigger challenge the system's flexibility.

Generation profiles shown in Figures 3.4b and 3.5b illustrate the impact of storage and variance constraints on generator outputs. Without storage (S1, brown), both generators show considerable fluctuations, particularly around periods of high RES generation, which can lead to increased costs for ramping in practice and more stress on the grid and less stable voltages. When storage is introduced (S2, blue), the generation curves are notably flattened, especially around midday peaks, as storage absorbs surplus energy and injects it when needed. Scenario S3 (green) imposes variance constraints on generators, which further smooths the generation profiles by shifting uncertainty to the storage unit. This demonstrates storage's dual role: not only energy shifting but also uncertainty mitigation.

Storage operation is visualized in Figures 3.4c and 3.5c. For both data types, storage is charged during periods of high renewable availability and discharged to buffer demand peaks. In the volatile case, storage also absorbs increased forecast uncertainty, reducing the need for fast adjustments of generators. Terminal

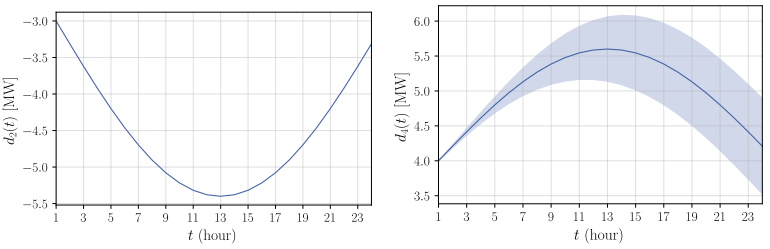

(a) Left: fixed load d_2; right: the uncertain load d_4.

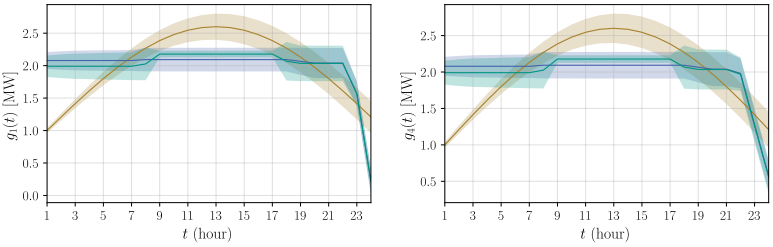

(b) Power injections of generators $\{g_1, g_4\}$.

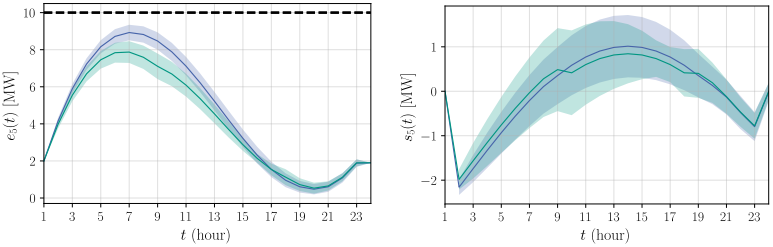

(c) Left: Power injections of storage s_5; right: respective change of power.

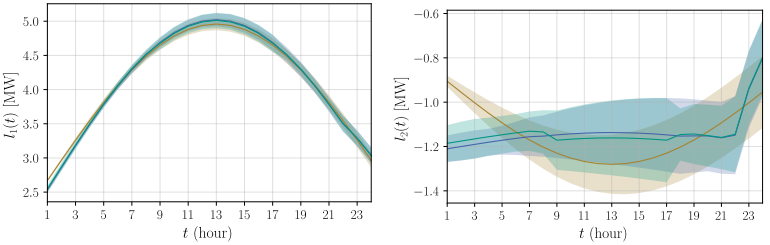

(d) Line flows of lines $\{l_1, l_2\}$.

Figure 3.4: OPF results for the IEEE 5-bus grid with synthetic wind generation without storage (S1, brown), with storage (S2, blue), and with storage and variance constraints (S3, green). The random variables x are depicted with their mean $\mathbb{E}(\mathsf{x})$ (solid) and scaled standard deviation $\mathbb{E}(\mathsf{x}) \pm \lambda(0.05)\sqrt{\mathbb{V}(\mathsf{x})}$ (shaded).

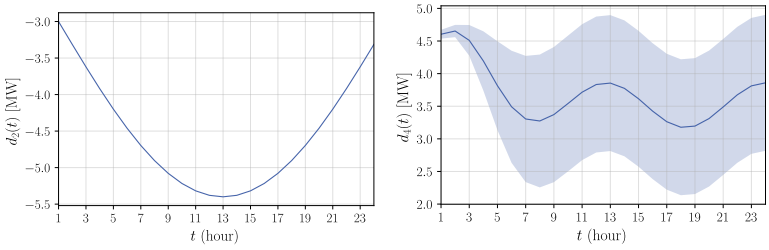

(a) Left: fixed load d_2; right: the uncertain load d_4.

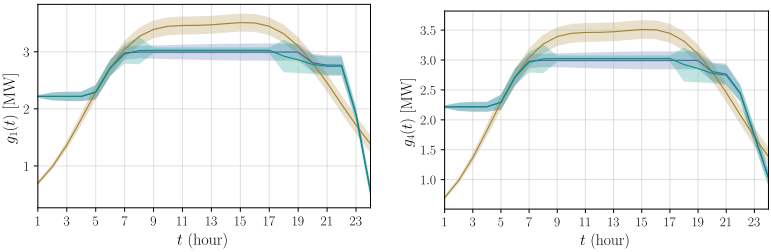

(b) Power injections of generators $\{g_1, g_4\}$.

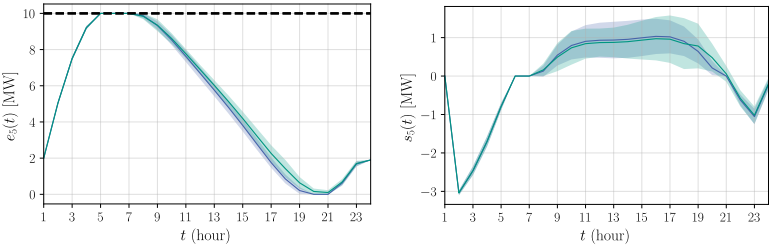

(c) Left: Power injections of storage s_5; right: respective change of power.

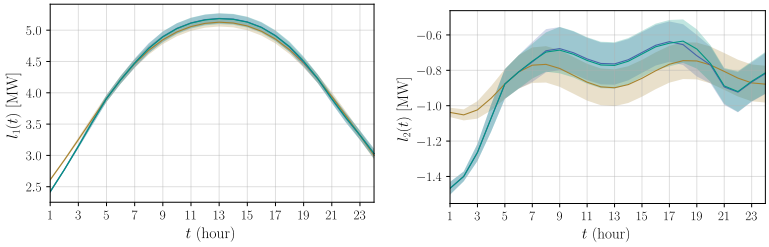

(d) Line flows of lines $\{l_1, l_2\}$.

Figure 3.5: OPF results for the IEEE 5-bus grid with real-world wind generation without storage (S1, brown), with storage (S2, blue), and with storage and variance constraints (S3, green). The random variables x are depicted with their mean $\mathbb{E}(\mathsf{x})$ (solid) and scaled standard deviation $\mathbb{E}(\mathsf{x}) \pm \lambda(0.05)\sqrt{\mathbb{V}(\mathsf{x})}$ (shaded).

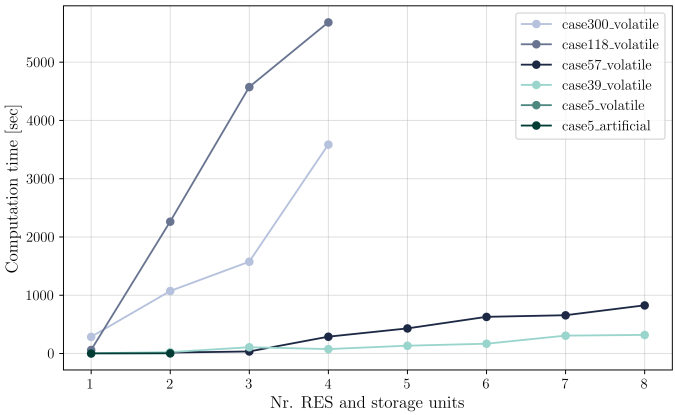

Figure 3.6: Computation time of all test cases with respect to the number of uncertainties and storage units.

energy constraints are met by recharging toward the horizon's end, emphasizing foresighted scheduling to maintain reliability under uncertainty.

Finally, line flows in Figures 3.4d and 3.5d reflect the combined effect of load, generation, and storage. Some lines show reduced flows with active storage, suggesting that storage can locally relieve lines and smooth power flows. Other lines remain sensitive to RES variability, particularly in the real-world forecast scenario. This demonstrates that while storage mitigates uncertainty, its effect is often local and depends on network topology and placement relative to RES and loads.

Overall, these results emphasize the critical role of storage in enhancing both operational flexibility and robustness to renewable uncertainty in small test systems.

Scalability Testing

We test scalability on IEEE 39, 57, 118, and 300-bus systems. Up to 7 uncertain loads and storage units are placed per system. Loads are selected based on demand magnitude; storage units are assigned randomly.

The OPF results for the IEEE 39-bus system are provided in the Appendix (Section A.2). The qualitative results mirror those of case5: storage units significantly reduce generator variance, smooth generation profiles, and lower total system costs.

Figure 3.6 shows computation time versus system size and number of uncertain nodes. Small systems solve in seconds, but runtime grows quickly for larger grids, reaching up to 15 minutes for cases with over 100 buses. This highlights the computational challenges posed by increasing network size and uncertainty. Longer time horizons further increase complexity: solving for 24 hours takes about 10 times longer than 12 hours due to quadratic growth in variables. The figure also reveals that more uncertain RES and storage units lead to longer computation times, reflecting the trade-off between model detail and solver tractability.

3.4 Summary & Discussion

This chapter presented and tested a multi-period stochastic DC-OPF model formulated as a second-order cone program (SOCP). The model incorporates distributed storage units and models uncertainty from renewable energy sources (RES) using Gaussian processes and chance constraints. Forecasts are generated through Gaussian Process Regression (GPR). The method is validated on a range of IEEE test cases, including scalability.

Strength The method offers a tractable and analytically exact formulation for modeling uncertainty in power systems. It scales well to networks of moderate size, up to around 100 nodes, without requiring additional optimization. Across all tested cases, storage significantly improves grid operation in high-RES scenarios by mitigating uncertainty, reducing total generation costs, and flattening generation profiles, thus enhancing predictability. Additionally, larger grids generally handle uncertainty better due to structural redundancy and the distributed nature of their components.

Limitations Despite these strengths, the method has several limitations. Most notably, its computational complexity grows rapidly with the time horizon, the number of uncertain nodes, and the number of storage units. For instance, solving the IEEE case300 with ten uncertain loads and ten storage units over a 12-hour horizon already takes several minutes. Furthermore, the model relies on the DC approximation of power flow, which neglects voltage magnitudes and reactive power and may be less accurate for meshed or distribution-level networks. The assumption of Gaussian uncertainty, while analytically convenient and partly justified through aggregation effects, does not always hold in practice and may limit the realism of the results. Finally, GPR itself is sensitive to the choice of kernel and its parameters, which makes the forecasting step less robust than desired and therefore needs to be fitted carefully.

Future Research There are several directions for future research. Improving the method's scalability through sparsity-aware solvers or decomposition techniques could make it suitable for larger systems. Extending the approach to an AC-OPF formulation would improve accuracy, especially in meshed networks. More robust forecasting models could replace GPR as Gaussian Process Regression has its limits. The storage model could be enhanced to include charging and discharging efficiencies, degradation effects, and operational costs. Lastly, the approach could be applied to more complex planning and market scenarios, including optimal siting and sizing of storage or adapting affine control policies to specific regulatory or market conditions.

Overall, the proposed method provides a rigorous and tractable framework for incorporating uncertainty and storage in power system operation. It delivers valuable insights into system behavior under high RES penetration and highlights the importance of optimal storage deployment for future grid planning and reliability.

4 Case Study: Turkish Transmission Grid

Publication reference for this chapter

Bauer, R. and Mühlpfordt, T. and Ludwig, N. and Hagenmeyer, V. (2022). "Analytical uncertainty propagation and storage usage in a high RES Turkish transmission grid scenario". *Proceedings of the Thirteenth ACM International Conference on Future Energy Systems*, p. 489-495. DOI: 10.1145/3538637.3539762

To further validate the multi-period DC stochastic OPF model from (3.13), we apply the model to a real-world setting: a newly built Turkish transmission grid. Wind power plants are modeled as uncertain renewable energy sources (RES), and we evaluate the optimal storage placement under three different scenarios. This chapter addresses research question

RQ2 *What influence does BESS placement have on managing uncertainty in the grid?*

This chapter is structured as follows. First, we provide background information on the Turkish transmission system and its strategic importance. Then, we detail the modeling approach and key assumptions used in our analysis. Following this, Section 1.2 presents the experiments and results evaluating the role of battery energy storage systems (BESS). Finally, Section 1.3 summarizes the main findings and conclusions.

4.1 The Turkish Transmission Grid Model

Background

Turkey plays a strategic role in the European energy system as a transit country for electricity and gas imports from Iran and Azerbaijan into the EU, with 2.2 GW of interconnection capacity via Bulgaria and Greece (EUROPEAN et al. 2024, Schröder et al. 2017).

The country has significant renewable energy potential—particularly wind in the west and solar in the southeast and central Anatolia—and continues to attract foreign investments (Bart 2020). Its high-voltage transmission grid, operated by the state-owned TEİAŞ, spans 154 kV and 400 kV and is rapidly expanding (Gullu 2024).

Despite this, the system faces persistent challenges: high energy theft rates (up to 20%) (EU 2014), dependency on fossil fuel imports (Tokyay 2022), and grid stability issues, including a major blackout in 2015 (TEIAS 2015). In addition, much of the infrastructure is exposed to seismic and drought risks (AFAD 2020).

As of 2019, Turkey had over 100 GW of installed capacity and produced more than 300 TWh of electricity. Renewables made up 10% wind, 7.5% solar, and roughly 32% hydroelectric power (Agency 2021, IRENA 2021). RES generation more than doubled between 2009 and 2021.

To meet its 2053 net-zero emissions goal, Turkey plans to add 60 GW of new wind and solar by 2035 and expand grid flexibility through large-scale BESS installations. New regulations (2023–2024) require renewable projects to include co-located storage (Syed 2024, Gullu 2024).

Figure 4.1: Overview of the Turkish transmission grid model used in this study.

Model Details

The Turkish transmission grid is built from the following sources: Line parameters—resistance (R), reactance (X), and susceptance (B)—are statistically derived using the distributions proposed in Kurban and Filik (2006). Line ratings are taken from a TEİAŞ transmission map (TEIAS 2004). Generator capacities are obtained from Peker et al. (2018) and adjusted to reflect national-level capacities in Japan International cooperation agency (2011). The Turkish transmission grid model consists of 61 buses, 92 transmission lines, and 24 generators. The grid topology is adapted from Kurban and Filik (2006), while electrical parameters are based on estimates and national data sources. The resulting topology is visualized in Figure 4.1, and the complete casefile is provided in Appendix A.1.

Wind power is concentrated in the western regions of Turkey (Marmara, Aegean, and Mediterranean), where wind resources are strongest, as shown in Figure 4.2. Accordingly, ten wind farms are placed in the western part of the grid, close to both wind potential and major industrial load centers (Godron et al. 2018), as visualized in Figure 4.3.

Wind generation follows the data and Gaussian Process forecasts from the previous section, smoothed with a rolling window of size 10 and scaled to the network's

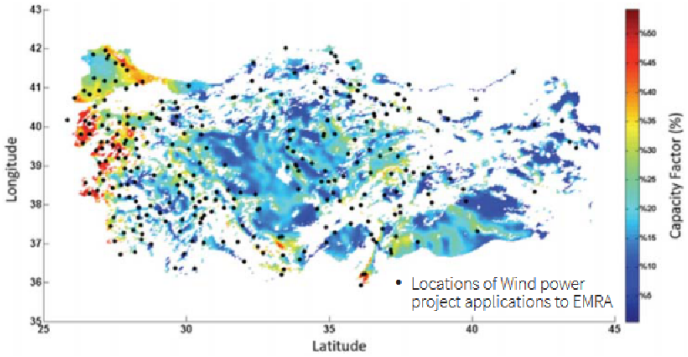

Figure 4.2: Wind capacity and locations for wind power plants in Turkey (Godron et al. 2018).

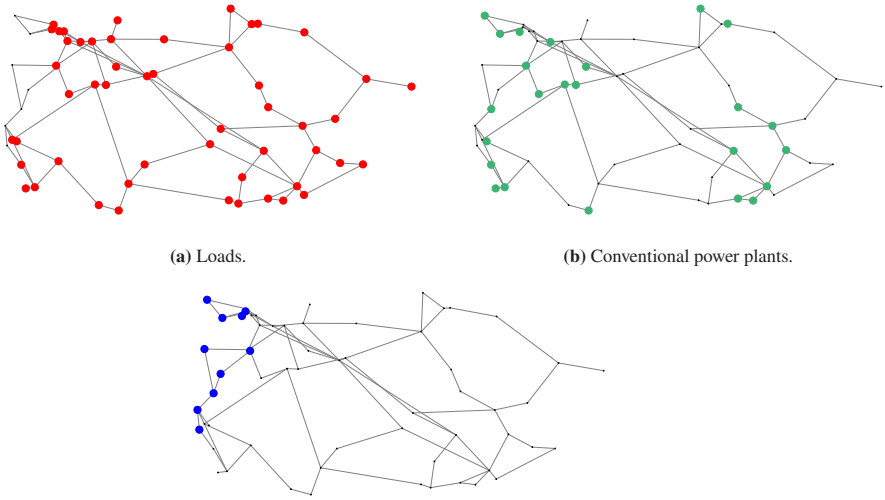

(a) Loads.

(b) Conventional power plants.

(c) Wind farms.

Figure 4.3: Locations of OPF components in the Turkish transmission grid.

capacity. The total system load is assumed to be 91,000 MW. Wind power is scaled to 25% (23,000 MW) of this load—more than twice Turkey's actual wind share in 2021—to simulate future high-RES scenarios.

Load profiles are based on a representative day in Peker et al. (2018) and scaled to match total demand. Loads are modeled synthetically as in the previous section, with spatial distribution matching historical usage patterns.

Storage units are not fixed but placed variably across the grid depending on the scenario. The time horizon is set to 12 hours, i.e., $\mathcal{T} = \{1, \ldots, 12\}$, to reduce computational complexity. Since data is scaled to the horizon, this only changes temporal resolution—not the behavior of the results.

4.2 Experiments

Table 4.1: Data and test grids for Chapter 4.

Data Type	Details
Grids	61-bus Turkish Transmission Grid (custom)
Time Series	ENTSO-E Wind Generation Data (2014-2021), *Northwind* (De Felice 2021)

The used data is summarized in Table 4.1.

Scenarios

To assess the impact of battery energy storage systems (BESS), we compare scenarios with and without storage integrated into the transmission grid. In this analysis, we do not consider variance constraints on generation, as there are no new insights compared to the last chapter.

Three storage placement strategies are analyzed to evaluate how location affects system behavior:

(a) *Close to wind generation*,

(b) *Close to load*,

(c) *Far away from load and wind generation*.

In all three scenarios, ten storage units are deployed, each with a capacity of 5 MWh and a maximum power rating of 10 MW. Their respective bus locations are:

(a) $\mathcal{N}_a = \{1, 2, 8, 9, 10, 11, 38, 39, 41, 43\}$,

(b) $\mathcal{N}_b = \{2, 5, 6, 15, 16, 20, 21, 34, 41, 45\}$,

(c) $\mathcal{N}_c = \{24, 27, 28, 29, 31, 33, 50, 57, 58, 59\}$.

All remaining parameters are kept consistent with previous experiments (see Table 3.3).

Results

We begin by analyzing scenario (b), where storage is placed near major load centers, followed by a comparison of all three placement strategies.

Figure 4.4 illustrates the power flow and storage operation results in the Turkish transmission grid under real-world renewable energy source (RES) forecast uncertainty. For numerical stability, the variables are scaled during computation and should be interpreted in GW rather than MW. In Figure 4.4a, the left plot depicts the fixed and uncertain loads, showing how the uncertainty bands capture the uncertainty in the demand profile. The generation profiles in Figure 4.4b reveal that, without storage (brown), conventional generators must closely follow the net load variations, leading to substantial ramping and variability in their output. When storage is introduced (blue), generation is notably smoother, as

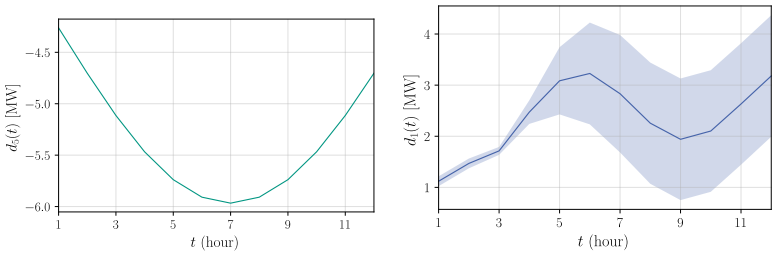

(a) Left: fixed load $-d_{61}$; right: the uncertain load d_1.

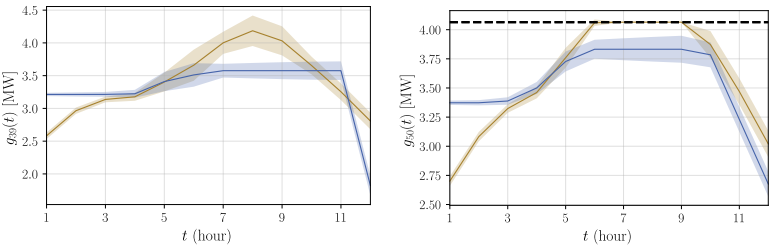

(b) Power injections of generators $\{g_{39}, g_{50}\}$.

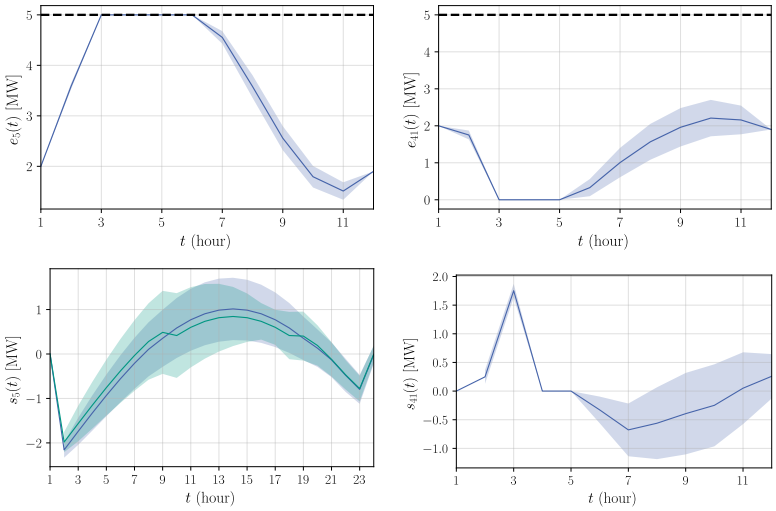

(c) Upper: State of storages $\{s_5, s_{41}\}$; lower: respective storage injections.

Figure 4.4: Turkish Network: Results for power flow (MW) without storage (brown) and with storage (blue). The random variables x are depicted with their mean $\mathbb{E}(\mathsf{x})$ (solid) and the scaled standard deviation $\lambda(0.05)\sqrt{\mathbb{V}(\mathsf{x})}$ (shaded).

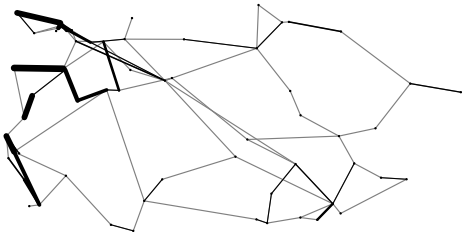

Figure 4.5: Line flows for scenario (a) with storage close to wind farms.

storage units absorb fluctuations and reduce the need for rapid adjustments in conventional generation. The storage operation plots in Figure 4.4c confirm that storage units charge during periods of high RES availability and discharge to meet demand peaks, effectively buffering uncertainty and flattening the net load seen by generators.

Figure 4.5 shows the resulting line flows for the scenario where storage is placed close to wind farms (a). It shows that the lines in the northwest region of the grid carry the highest power flows, indicating these transmission corridors are critical for managing energy transfer under uncertain RES conditions. The presence of storage mitigates flow variability on many lines by smoothing injections, for example, more than in scenario (c). However, some lines connected to wind farms still show heavy loading.

The results for the different storage locations are given in Figure 4.6. All storage units are used, and many are filled fully. At time $t = 6$, when storage is used most, the total storage injections are (a) 35 MW, (b) 36 MW, and (c) 28 MW. This indicates that storage is used most when it is near demand or load. However, as DC-OPF ignores losses, the differences might be even larger for AC-OPF.

A comparative analysis of all storage placement scenarios is shown in Figure 4.6. At time step $t = 6$, when storage activity is at its peak, the total injections from

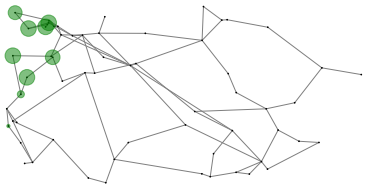

(a) Storage directly at wind farms in the west.

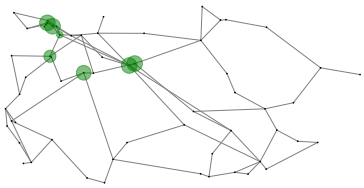

(b) Storage close to high demand in the center.

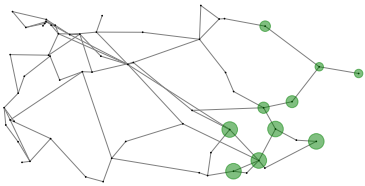

(c) Storage far away from wind farms in the east.

Figure 4.6: Storage fill state for three scenarios at $t = 5$.

storage are: (a) 35 MW, (b) 36 MW, and (c) 28 MW. These results suggest that storage is utilized most effectively when located near demand centers. As DC-OPF neglects network losses, the actual benefit of better placement might be even more pronounced in an AC-OPF formulation.

The mean active power line flows for all scenarios at $t = 6$ are compared in Figure 4.7, with scenarios (a), (b), and (c) shown in light blue, magenta, and brown, respectively. We can see that when storage is placed remotely (scenario c), key interregional transmission lines are significantly more loaded. Some lines approach their thermal limits and may be considered congested.

In contrast, scenario (b) with storage near load consistently results in the lowest overall line utilization, indicating that this placement strategy minimizes transmission stress.

Figure 4.8 summarizes the total active power line flows over all buses, given over the full horizon. When storage is colocated with wind generation (scenario a), power flow profiles follow the wind generation curve. Storage near load

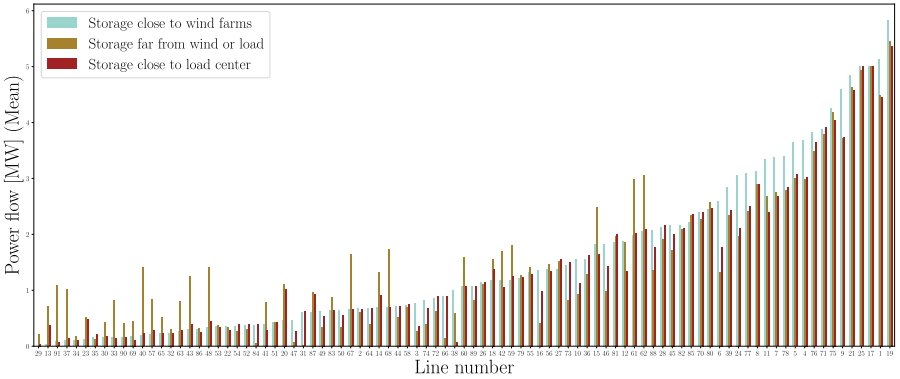

Figure 4.7: Differences in mean active power line flows for three storage scenarios (a)-(c) for $t = 6$.

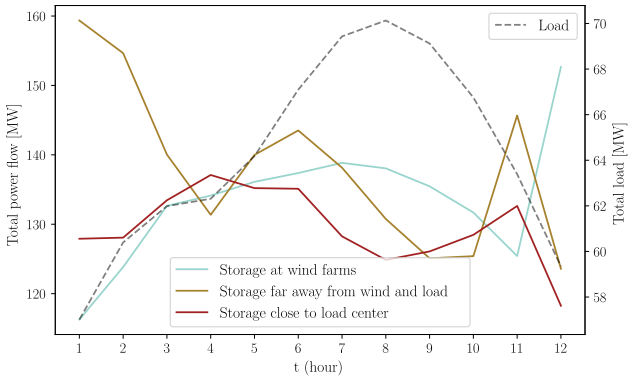

Figure 4.8: Sum of absolute mean active power line flows for all three storage scenarios (a)-(c) and sum of mean loads over horizon $\mathcal{T}$.

(scenario b) yields similar but slightly reduced flow peaks. The most pronounced flow swings are seen in scenario (c), where storage units, located far from both generation and demand, cause sharp injections and withdrawals early and late in the horizon to satisfy their boundary constraints.

These results confirm that the Turkish grid's behavior under uncertainty mirrors the findings from the previous case studies: storage units play a crucial role in managing variability by absorbing RES uncertainty, stabilizing generation profiles, and relieving stress on key transmission lines. The demonstrated ability of storage to smooth generation and line flows supports its consideration as an essential component in Turkey's evolving power system.

4.3 Summary

The case study of the Turkish transmission grid confirms that the proposed multi-period stochastic DC-OPF formulation performs reliably on realistic, large-scale networks. Storage units prove effective in mitigating renewable uncertainty and enhancing operational stability.

Among the evaluated strategies, placing storage close to load centers yields the best system-wide benefits: lower line loading, more stable generation schedules, and fewer operational bottlenecks.

These findings support a key recommendation for future high-RES power systems: integrating distributed storage—especially near demand centers—can substantially reduce operational stress and improve flexibility.

Notably, since the time of this study, Turkey has taken steps to implement large-scale storage solutions (7.5 GW by 20235) in alignment with its 2053 net-zero roadmap and REPowerEU goals. According to Gullu (2024), the transmission lines that will be most overloaded in the Turkish transmission grid in 2035 are close to the load in the west. Suggested storage locations are in the west, too, but not solely as Turkey also has a lot of PV power in the south-east. The largest

capacity, however, is in states with much load, not those with the most wind power. Additionally, as it is connected to a large gas supply country, it has seven gas pipelines through the country and sees itself as a central country in the future world energy market (Gürses 2022).

Part II

The Shapley Value: Towards Application in the Power Grid

5 Introduction

The second part of this thesis shifts from managing uncertainty to improving explainability in power systems, while maintaining a focus on battery energy storage systems (BESS). While Part I showed that BESS can mitigate the variability of renewables and support grid stability, this alone is often not enough in today's complex electricity systems.

As the energy transition advances, power systems shift from centralized generation to distributed renewables, increasing volatility and making power flows harder to predict and control. This poses new challenges for TSOs, who must ensure secure operation while managing uncertainty.

Traditional tools like PMUs or power flow simulations show the system state but not who or what causes specific outcomes. For example, in redispatch, congestion may affect many lines, but only a few are responsible. Simple proportional cost allocations can be unfair and mislead future planning. TSOs need better methods to understand and fairly attribute the impact of individual grid components.

In Part II, we aim to evaluate each component's contribution to system performance more fairly and transparently. If the true impact of a line, generator, or storage unit is known, it can be priced accordingly and controlled more effectively. To share total system costs, we use an *allocation rule*—specifically, the *Shapley value*.

Allocation rules are widely used to distribute costs or benefits in multi-agent systems. Among them, the Shapley value stands out for its fairness properties. It has been applied in economics, machine learning, and increasingly, in power systems. In our context, fairness helps uncover the true operational role of each

grid component, such as how much a congested line contributes to redispatch costs or how much a storage unit helps relieve it.

The use case of redispatch cost allocation was introduced by a German TSO and studied in Voswinkel et al. (2022), which applied the Shapley value to a simple DC-OPF model to allocate costs between TSOs and distribution system operators (DSOs). While promising, the study had two main limitations: it used the linear DC-OPF (ignoring reactive power), and it did not evaluate the Shapley value's behavior in more complex grids or real-world scenarios.

This part addresses both points. First, we improve realism by using the nonlinear AC-OPF formulation, as DC-OPF solutions are never AC feasible (Baker 2021). Second, we respect data privacy by solving it in a distributed way—so grid operators do not need to share their full models. Third, we extend the Shapley value beyond cost allocation: we use it as an explainability tool to assign utility. Similar to explainable AI (XAI), where Shapley is used to evaluate feature importance[1], we apply it to grid components. This allows us to quantify each component's influence on total cost or constraint violations—more precisely than proportional methods, which serve as our baseline.

The rest of this part is organized as follows: Chapter 6 introduces game theory, allocation rules, and the Shapley value. Chapter 7 presents a distributed AC-OPF formulation that respects data privacy. Chapter 8 compares DC and AC-OPF results for cost allocation and congestion patterns. Chapter 9 includes BESS units and analyzes their role using active and reactive power. Chapter 10 conducts a sensitivity analysis on the robustness of Shapley values across component types.

[1] The SHAP package (SHapley Additive exPlanations) is used in XAI (eXplainable AI). It uses the Shapley value to assign each input feature a fair contribution to a model's prediction, making black-box models like neural networks more interpretable. It explains which features influence predictions and in what direction.

6 Fundamentals of Allocation Rules

This chapter provides the theoretical foundation for allocation rules in power systems and explains how different methods assign costs or benefits to individual components in an interconnected electricity network. It also motivates why cooperative game-theoretic approaches—in particular the Shapley value—are central for obtaining fair and transparent allocations.

Allocation rules are mathematical tools used to assign system-wide costs (e.g., from generation, losses, redispatch, investments) or profits to individual participants in the power grid (e.g., system operators, consumers, technical components).

In interconnected power systems, components influence each other through the network: A generator's output changes power flows, a line congestion results in redispatch costs, and a battery can shave RES generation peaks. Because these interactions are not always local, simple rules, such as proportional sharing, often misrepresent 'true' impact. Hence, we need to choose an appropriate allocation rule suited to the base system.

In the following, we define the requirements for allocation rules in power systems—with a particular focus on fairness—provide an overview of the main existing methods, explain why the Shapley value is the most suitable choice, and introduce the mathematical foundations.

6.1 Allocation Rules

There are various types of allocation rules that can all be used for power grids. They do have different properties that serve different purposes, so let us put up some requirements that an allocation rule for cost and utility allocation should fulfill, and then see why the Shapley value is the most suitable one.

Requirements for Power Systems

In our problem setting we have several participants in the power grid, e.g., grid components or TSOs, and we want to know their contribution to the total operation or redispatch costs. Hence, the goal is to allocate the total system costs to individual participants or components in the power grid.

Doing that in a fair way is essential because it shows the 'true' costs for each participant. At the same time, the value should be interpretable to make the grid's complex inner workings transparent, as well as predictable and reproducible. This suggests an analytical value. Moreover, the method must reflect how components interact through the network, as these interactions are often non-local and sometimes non-linear.

Hence, the desired requirements, similar to Conejo et al. (2002), are:

- **Analytical**: Deterministic and comprehensible.
- **Transparency**: Cost allocation needs to be understandable, and utility should help to understand the inner grid dynamics.
- **Fairness**: Fair cost allocation and 'true' contributions of a grid component.
- **Consider power flows**: The grid needs to be considered as it heavily influences generation and thus costs.
- **Consider location**: Location is considered through the grid; where a component is located in the grid matters and should reflect in the allocation.

– **Consider participants' interactions**: We want to depict the complex interactions between grid components.

These requirements already exclude many heuristic or tracing-based methods, which often fail to capture interactions or depend on ad-hoc assumptions. Cooperative game theory is a natural framework here because it explicitly links the allocation of a participant to its contribution. Fairness is an important requirement, so let us define what we mean by that quantitatively.

A First Description of Fairness

In the context of power systems, fairness refers to how well an allocation reflects a participant's actual impact on the system. Three aspects are particularly relevant:

– **Marginal impact**: Participants should pay or receive amounts proportional to the change in system cost they induce.

– **Consider location**: Allocations should reflect only physical influence through the network, without a locational bias.

– **Consistency in representation**: Allocations should not change unexpectedly when similar components are grouped or separated.

These fairness principles guide the selection of allocation rules, since not all of them fulfill them, and are formalized mathematically later in the chapter.

Overview of Allocation Rules

A selection of the various game-theoretic and flow-based allocation rules, along with their properties, are listed in Table 6.1. There are three families: the *core* and *Shapley family* from cooperative game theory, and the *power flow-based* methods. The simple proportional pro-rata rule is added for completeness. We shortly describe all the families before we reason the choice of the Shapley value.

Table 6.1: Comparison of allocation rules across cooperative game theory and power-flow-based methods (Analyt. = Analytical, CR = Coalitional Rationality, EXC. = Excess, E = Efficiency, A = Additivity, NA = Null Agent, S = Symmetry, IR = Individual Rationality, EQ = Equity, Diff. = Difficult, V. = Value, R. = Rule)

	Core-related Methods			**Shapley-based Methods**				**Power Flow-based**		
Property	**Core**	**Kernel**	**Nucleolus**	**Shapley**	**Myerson**	**Aum.-Shapley**	**τ-Value**	**P. Sharing**	**Z-Bus**	**PTDF**
Efficiency	✓	✓	✓	✓	✓	✓	✓	✓	✓	✓
Fairness	Mid	Mid	Mid	High	Mid	High	Mid	Low	Low	Low
Existence	–	–	✓	✓	✓	✓	✓	✓	✓	✓
Uniqueness	×	–	✓	✓	✓	✓	✓	✓	✓	✓
In Core	–	✓	✓	–	–	–	–	–	–	–
Axioms	E,CR	E,IR	E,IR	E,A,NA,S	E,S	E,A,NA,S	E,S,IR,NA	–	–	–
Network	✓	×	✓	✓	✓	✓	×	✓	✓	✓
Marg. contrib.	×	×	×	✓	✓	✓	×	×	×	×
Form	SoE	Opt.	Opt.	Analyt.	Analyt.	Analyt.	Opt.	Analyt.	Analyt.	Analyt.
Complexity	High	High	High	High	High	High	Mid	Low	Mid	Mid
Transparency	Low	Low	Low	High	Mid	Mid	High	High	Mid	Mid
Implementation	Diff.	Low	Diff.	Easy	Mid	Mid	High	Easy	Mid	Mid
Scalability	Low	Low	Low	Low	Mid	Mid	Mid	Mid	Mid	High

Core-Related Methods

The *core* is a fundamental concept in cooperative game theory (Peters and Peters 2008, Fiestras-Janeiro et al. 2011). It defines a set of stable allocations where no coalition can improve its payoff by deviating. Formally, it is a convex subset of $\mathbb{R}^n$ defined by linear inequalities that satisfy *efficiency* and *coalitional rationality*. While it ensures stability, the core is not always non-empty—it exists only for *balanced* games[1]. Stability is not part of the fairness axioms, which is why the Shapley value need not lie in the core.

Two key rules derived from the core are the *Nucleolus* and the *Kernel*. The *Nucleolus*, introduced by Schmeidler (1969), minimizes the maximum dissatisfaction (excess) among all coalitions and yields a unique solution if the core is non-empty. It assumes an *essential game*[2] but is computationally intensive due to nested LPs.

The *Kernel* models bilateral bargaining and satisfies *efficiency* and *individual rationality*. It does not guarantee uniqueness and is harder to compute due to its nonlinear formulation. Both values focus on coalition stability but are less transparent than Shapley-based rules.

Shapley-Family Methods

The Shapley value and its variants allocate costs based on marginal contributions. All are analytical, ensuring existence and uniqueness.

The *Shapley value*, introduced by Shapley (1952), is the foundational solution concept in cooperative game theory. It distributes total system costs based on each player's average marginal contribution across all possible coalitions. Importantly, it is the *only* value that satisfies all key fairness axioms: *efficiency, symmetry,*

[1] "A balanced game is one where, informally, no coalition structure can demand more than the grand coalition's value." (Hougaard 2009)

[2] A game is essential if the grand coalition yields more than the sum of individual values. (Peters and Peters 2008)

null player, and *additivity*. This makes it particularly attractive for applications that demand fairness, interpretability, and analytical transparency—such as cost allocation or influence quantification in power systems. It is defined rigorously later in Section 6.3.

The *Myerson value* adapts the Shapley value to networked systems (Caulier et al. 2017), where only connected players can form coalitions.[3] It reflects communication or physical constraints and scales better due to sparse network topologies. Applications include power systems and explainable AI (Homberg et al. 2024).

The *Aumann–Shapley value* extends the concept to continuous cost functions (Caulier et al. 2017), using path integrals over gradients. It works well in convex settings like DC-OPF, but in nonconvex models such as AC-OPF, undefined gradients can cause ambiguity and instability.

The *Weighted Shapley value* allows for asymmetric players (Shapley 1953, 1952), introducing weighted symmetry and a relaxed version of additivity (Béal et al. 2018). This is useful in applications where voting power or influence varies among players.

Power Flow-Based Methods

Flow-based methods allocate costs based on physical grid behavior. They are transparent and fast, but do not satisfy game-theoretic properties like *marginality*.

Proportional Sharing distributes power flows proportionally among outgoing branches (Bialek 1996). While simple and intuitive (Conejo et al. 2002), it is based on DC approximations and lacks accuracy for systems with losses or reactive power.

The *Z-bus method* uses the impedance matrix to allocate costs based on voltage angles (Conejo et al. 2007). It captures AC behavior but is computationally heavy

[3] Disconnected networks limit feasible coalitions.

and scales poorly. Related approaches like Incremental Transfer Loading (ITL) suffer from volatility and allocation imbalances (Karthikeyan et al. 2013).

PTDF-based methods rely on linear sensitivity factors (Kern and Wendlinger 2022) that quantify how injections affect line flows under DC assumptions. They are scalable and computationally efficient but unsuitable for nonlinear AC settings.

Proportional Rule

The *pro-rata* method is the most basic allocation rule, assigning costs directly proportional to usage (Conejo et al. 2002). It is entirely independent of the network structure, highly scalable, and extremely easy to implement. However, it neglects both physical flow characteristics and strategic interactions. Consequently, it often leads to allocations that are considered unfair in complex systems (Ilic et al. 1998). Nonetheless, it is a common industry benchmark due to its simplicity and transparency, and shall also serve as a benchmark at some point in this thesis.

Why not use non-cooperative game theory?
Non-cooperative game theory is not suitable for our setting. As Robert Aumann notes in an interview (van Damme 1998), non-cooperative models focus on strategic behaviour and players acting against each other, as in pricing or bidding problems. In contrast, cooperative game theory focuses on the joint outcome through cooperation and how to allocate it among participants. In power systems, we see cooperation of congestion or components as being 'simultaneously active' and want to determine their contribution to the overall cost. Hence, only cooperative game theory suits the purpose.

Why choose the Shapley value?

Game-theoretic methods offer stronger fairness guarantees, but differ in transparency, uniqueness, and computational effort. Among them, the Shapley value is the only analytical and fully axiomatic method that does not require an additional optimization criterion, unlike the Nucleolus or kernel. Flow-based methods, while

intuitive and fast, cannot represent marginal contributions and therefore cannot capture true system impact.

For this thesis, transparency and analytical tractability are essential. We therefore adopt the Shapley value as the main allocation method and use a proportional rule as a simple baseline. In the following, we give the game-theoretic foundations to define the Shapley value and its fairness axioms rigorously.

6.2 Cooperative Game Theory

This section introduces the basic notions of cooperative game theory. It is based on the book "An Introduction to Allocation Rules" by Hougaard (2009).

In the power grid setting, the problem of sharing operation costs can be formulated as a cooperative game. A cooperative game consists of a set of players $\mathcal{P}$, who may collaborate by forming coalitions $\Omega \subseteq \mathcal{P}$, and a cost function Φ assigning a value to each coalition. The utility is assumed to be freely transferable between players, meaning all participants use the same unit of payment. A cooperative game with this property is called a transferable-utility (TU) game (Peters and Peters 2008, Hougaard 2009).

Definition 1 (Cooperative Game with Transferable Utility (TU Game)) *A TU game is a tuple $(\mathcal{P}, \Phi)$, where $\mathcal{P} = \{1, \ldots, N\}$ is the set of players and the cost function $\Phi : \mathfrak{P}(\mathcal{P}) \to \mathbb{R}$ assigns each coalition Ω in the power set $\mathfrak{P}(\mathcal{P})$ a value $\Phi(\Omega) \in \mathbb{R}$. The empty coalition satisfies $\Phi(\emptyset) = 0$, and the full set $\bar{\Omega} = \mathcal{P}$ is the* grand coalition.

As defined above, all players may act jointly by forming the grand coalition, which produces the total cost $\Phi(\mathcal{P})$ (e.g., obtained from an OPF). Distributing this total cost among the individual participants $p \in \mathcal{P}$ is called a payoff distribution. Such a distribution is determined by an allocation rule Ψ (Hougaard 2009).

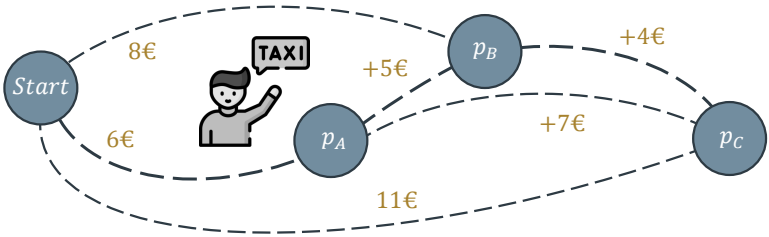

Figure 6.1: The Taxi Game; the path costs represent the marginal contributions.

Definition 2 (Cost Allocation Rule) *Consider a TU game* $(\mathcal{P}, \Phi)$. *A* cost allocation rule *is a mapping* $\Psi : \mathcal{P} \to \mathbb{R}^n$ *with* $n = |\mathcal{P}|$ *such that*

$$\sum_{p \in \mathcal{P}} \Psi_p(\Phi) = \Phi(\mathcal{P}), \tag{6.1}$$

i.e., the total allocated cost equals the value of the grand coalition. An allocation is the resulting vector $(\Psi_p(\Phi))_{p \in \mathcal{P}} \in \mathbb{R}^n$.

To compute an allocation rule, the contribution of a player $p \in \mathcal{P}$ to a coalition Ω is often needed, which is called the *marginal contribution* (Hougaard 2009).

Definition 3 (Marginal Contribution) *In a TU game* $(\mathcal{P}, \Phi)$, *the* marginal contribution *of a player* $p \in \mathcal{P}$ *to a coalition* $\Omega \subseteq \mathcal{P} \setminus \{p\}$ *is defined as*

$$\Phi(\Omega \cup \{p\}) - \Phi(\Omega), \tag{6.2}$$

i.e., the change in cost caused by adding player p. *Note that the marginal contributions can be negative in special cases.*

Taxi Example

A simple taxi-sharing example can illustrate cost sharing with marginal contributions intuitively before applying them to power systems.

Example 1 (Taxi Game) *Three passengers p_A, p_B, p_C share a taxi but exit at different locations. Let Φ be the cost function. Individually, they would pay*

$$\Phi(p_A) = 6, \quad \Phi(p_B) = 8, \quad \Phi(p_C) = 11.$$

If they ride in pairs,

$$\Phi(\{p_A, p_B\}) = 11,\ \Phi(\{p_B, p_C\}) = 14,\ \Phi(\{p_A, p_C\}) = 13,$$

and all three together pay

$$\Phi(\{p_A, p_B, p_C\}) = 15.$$

The costs are visualized in Figure 6.1. The pair $(\mathcal{P}, \Phi)$ forms a TU game.

Marginal contributions. *For instance, the marginal contribution of p_A to $\{p_B, p_C\}$ is*

$$\Phi(\{p_A, p_B, p_C\}) - \Phi(\{p_B, p_C\}) = 15 - 14 = 1.$$

Towards a fair allocation. *A natural idea is to consider all possible orders in which passengers might enter the taxi and record how much extra cost each one adds when joining the group formed so far. For p_A, this involves the coalitions $\emptyset, \{p_B\}, \{p_C\}, \{p_B, p_C\}$. Their marginal contributions vary: joining the nearly complete coalition $\{p_B, p_C\}$ adds only 1, joining $\{p_B\}$ or $\{p_C\}$ adds 3, and joining an empty taxi adds 6.*

A weighted average (reflecting how often each coalition appears) yields approximately

$$p_A = \frac{6+1}{3} + \frac{3+2}{6} = 3\frac{1}{6} \approx 3.167, \qquad p_B = \frac{8+2}{3} + \frac{5+3}{6} = 4\frac{2}{3} \approx 4.667,$$
$$p_C = \frac{11+4}{3} + \frac{7+6}{6} = 7\frac{1}{6} \approx 7.167$$

which sum to the total fare of 15.

This averaging idea—evaluating all orders and combining their marginal contributions—is exactly the intuition behind the Shapley value.

6.3 Shapley Value

The Shapley value is the 'truest' allocation rule in cooperative game theory with respect to the players' marginal contributions. It considers a player's marginal contribution in every coalition and weights these contributions according to how frequently each coalition appears when players join in all possible orders. Because only coalition size matters, coalitions of the same size receive the same weight. Averaging these weighted contributions over all permutations yields a fair and unbiased cost allocation. The Shapley value is defined following Lipovetsky (2020).

Definition 4 (Shapley Value) *Let* $(\mathcal{P}, \Phi)$ *be a TU game. The Shapley value is the allocation rule* Ψ *defined for each player* $p \in \mathcal{P}$ *as*

$$\Psi_p(\Phi) = \sum_{\Omega \subseteq \mathcal{P} \setminus \{p\}} \underbrace{\frac{|\Omega|!\,(|\mathcal{P}| - |\Omega| - 1)!}{|\mathcal{P}|!}}_{\textit{weight}} \underbrace{\Big[\Phi(\Omega \cup \{p\}) - \Phi(\Omega)\Big]}_{\textit{marginal contribution}}. \tag{6.3}$$

In words, the value of player p *is obtained by summing the player's marginal contribution to every coalition* Ω *not containing* p*, weighted by how often this coalition appears when all players join in random order. The weight counts permutations of players in* Ω*, permutations of the remaining players, and normalizes by the total number of permutations.*

The Shapley value has several interpretations depending on its use case. In a player-focused setting, it can describe power or influence (e.g., politics), a contribution, or simply an expected value. Looking at it outcome-oriented, it can

provide a comparison of all possibilities, yield explainability (e.g., XAI), merely be a probability, or serve as a cost allocation method.

The Shapley value is analytical and gives a linear payoff distribution (Peleg and Sudhölter 2007). By that, it is particularly useful for OPF-based applications of the power grid. One downside is its combinatorial complexity of $O(2^{|\mathcal{P}|})$ for $|\mathcal{P}| - 1$ coalitions. This means for 10 players, 1024 OPFs have to be computed.

It is also the unique value that fulfills the whole fairness definition, described by the properties above and defined mathematically below (Caulier et al. 2017). All advantages and drawbacks are summarized in Table 6.2

Table 6.2: Advantages and disadvantages of the Shapley value.

Advantages	Disadvantages
– guarantees fairness – reflects the 'true' contribution – analytic / closed-form – transparent, comprehensible – simple implementation – considers the grid structure – considers the marginal contributions	– has high computational complexity – (equal weight to all players)

Fairness Axioms

According to the requirements defined for power systems, an allocation rule should distribute the total system cost exactly, treat equivalent participants identically, assign zero cost to components that have no influence, and respond linearly when cost functions are combined. These ideas are captured by four classical fairness axioms: *Efficiency*, *Symmetry*, *Null player*, and *Additivity* (Lipovetsky 2020,

Peters and Peters 2008). This axiomatization traces back to Shubik (1962), while Shapley's original formulation relied on the related axioms of carrier, additivity, and anonymity (Shapley 1953). An overview of axiomatizations is to be found in Shan et al. (2023).

Efficiency ensures that the full cost of the grand coalition is allocated, without deficit or surplus.

Axiom 1 (Efficiency (Lipovetsky 2020)) *For a TU game $(\mathcal{P}, \Phi)$, an allocation rule Ψ satisfies efficiency if*

$$\sum_{p \in \mathcal{P}} \Psi_p(\Phi) = \Phi(\mathcal{P}). \tag{6.4}$$

Symmetry states that players who affect the cost function in exactly the same way must receive the same allocation.

Axiom 2 (Symmetry (Lipovetsky 2020)) *Let $(\mathcal{P}, \Phi)$ be a TU game and $p, q \in \mathcal{P}$. If*

$$\Phi(\Omega \cup \{p\}) = \Phi(\Omega \cup \{q\}), \quad \forall\, \Omega \subseteq \mathcal{P} \setminus \{p, q\}$$

then a symmetric allocation rule satisfies

$$\Psi_p(\Phi) = \Psi_q(\Phi).$$

Some components may have no influence on the system cost when added to any coalition. Such a component is a *null player*.

Definition 5 (Null player) *A player p is a null player if*

$$\Phi(\Omega \cup \{p\}) = \Phi(\Omega). \quad \forall\, \Omega \subseteq \mathcal{P}$$

Axiom 3 (Null player (Lipovetsky 2020)) *If p is a null player, then*

$$\Psi_p(\Phi) = 0.$$

Additivity expresses linearity of the allocation with respect to the cost function.

Axiom 4 (Additivity (Lipovetsky 2020)) *Let* $(\mathcal{P}, \Phi)$ *and* $(\mathcal{P}, c')$ *be two TU games. Then an allocation rule* Ψ *is additive if*

$$\Psi(\Phi + c') = \Psi(\Phi) + \Psi(c').$$

Remark 1 *The Shapley value does* not *satisfy* individual rationality *or* coalitional rationality*, in contrast to stability-oriented concepts such as the core or the nucleolus. These rationality axioms are meaningful when players are strategic decision-makers, but not in power systems, where "players" represent grid components. Because network effects can make a component reduce total cost when added to a coalition, such rationality conditions are not appropriate.*

The Shapley Value for Power Grids

In power systems, the Shapley value can be used in several ways depending on how the players and the characteristic function are defined. Typically, the characteristic function is the outcome of an OPF,

$$\Phi = c,$$

representing generation cost, redispatch cost, losses, or any other system-wide utility (e.g., active or reactive power). Players may be system operators (TSOs, consumers) or physical grid components such as lines, generators, loads, or storage units. Forming a coalition means that the corresponding components operate simultaneously.

In the literature (Fiestras-Janeiro et al. 2011), most Shapley-based applications focus on *transmission cost allocation* (players = generators/loads, value = transferred MW) and *network usage and wheeling cost allocation* (players = transactions, value = transmission cost). These applications typically use a DC-OPF-based characteristic function.

In this thesis, we examine two applications of the Shapley value in power grids.

Application 1—Congested Power Lines

We examine the case where the players are congested transmission lines, and the cost function represents redispatch costs required to relieve those congestions. Adding or removing a player corresponds to relaxing or enforcing that line's thermal limit. The grand coalition represents the operating point where all congestion–relevant lines have *active* limits. Inactive limits are set sufficiently high in the optimization problem so that the corresponding power flows do not reach them. This is determined via a preliminary power flow: if a line is congested (its flow exceeds the original limit), the limit is raised; otherwise, it remains unchanged.

Application 2—Grid Components

If the players are flexible grid assets such as BESS units, the cost function is typically the generation cost from the OPF. Each unit reduces this cost through flexibility, creating a *utility*. Here, adding or removing a player corresponds to activating or deactivating the device. The grand coalition describes the case where all units are simultaneously available.

The following chapters apply the Shapley value to power systems across four steps toward practical implementation. First, using congestion as an application case, we study computational aspects such as distributed evaluation and compare AC and DC OPF formulations. Second, we apply the value to grid components such as BESS units and generators, and analyse its robustness under perturbations and modelling uncertainties. These applications demonstrate how the Shapley value can be used to assess influence, allocate costs, and support decision-making in modern electricity networks.

7 Privacy-Preserving Cost Allocation

Publication reference for this chapter

Bauer, R. and Dai, X. and Hagenmeyer, V. (2023). "A Shapley value-based Distributed AC-OPF Approach for Redispatch Congestion Cost Allocation". *Proceedings of the 14th ACM International Conference on Future Energy Systems*, p. 109-113. DOI: 10.1145/3575813.3576881

With rising congestion in the German electricity grid, the four transmission system operators (TSOs) are under increasing pressure to prevent overloads through redispatch. Since power flows naturally across all regions, this can only be managed effectively through close collaboration. The same holds on a European scale: the pan-European grid is highly interconnected, with frequent inter-country transit flows and energy traded continuously across borders—not least to avoid blackouts.

To manage such complexity, TSOs need to coordinate their actions and jointly compute the Optimal Power Flows (OPFs) across larger parts of the grid. New digital platforms like PICASSO (ENTSO-E 2022) and Connect+ are currently being developed to facilitate this kind of cooperation. However, such collaboration brings new challenges—above all, grid security and data privacy. TSOs want to work together, but they are not willing (or allowed) to fully share sensitive grid data such as their internal topologies or time series for load and generation. This refers to research question

RQ3 *How can we preserve data privacy between grid regions when computing the Shapley value?*

In the context of redispatch in Germany, this can be reformulated as: *How can we share redispatch costs fairly without having to share grid model data?*

One proposed answer, introduced earlier in this thesis and studied in Voswinkel et al. (2022), is to use the Shapley value as a fair cost allocation rule. It allows redispatch costs to be distributed proportionally to each TSO's contribution to the underlying congestion. However, computing the Shapley value requires solving OPF problems for many different configurations of TSO participation. To make these results realistic and applicable in practice, we rely on the full non-linear AC-OPF formulation—since solutions from DC-OPF are not generally AC feasible (Baker 2021). Yet, for larger grids, solving the AC-OPF centrally becomes increasingly difficult due to its non-convexity and computational complexity.

This computational challenge motivates a shift toward **distributed optimization**. By decomposing a large OPF problem into smaller local subproblems, which are solved in parallel and coordinated iteratively, we can handle the large number of scenarios required for Shapley value computations more efficiently. Distributed methods not only mirror the structure of today's decentralized energy systems but also address data privacy concerns, as full grid topologies or detailed time-series data for load and generation need not be shared. While these approaches are naturally suited for distribution grids connected to the transmission system at a single point, as we demonstrate in this chapter, they can also be effectively applied to meshed transmission networks with complex inter-TSO couplings. Beyond privacy, distributed optimization further enhances scalability and resilience: it reduces the computational burden and isolates failures to individual regions without disrupting the entire system.

Related Work Several distributed algorithms have been proposed for solving the AC-OPF problem. The most common first-order methods include the Optimality Condition Decomposition (OCD) (Hug-Glanzmann and Andersson 2009), the Auxiliary Problem Principle (APP) (Baldick et al. 1999), and the Alternating

Direction Method of Multipliers (ADMM) (Erseghe 2014). While these are relatively simple and lightweight, they have one major drawback: the nonconvexity of the AC-OPF problem makes convergence hard to guarantee in general, and performance often depends on problem structure and initialization. This is because AC-OPF is proven to be NP-hard (Bienstock and Verma 2019), and these first-order methods only work well under specific assumptions.

To improve convergence, second-order methods have been developed. One notable example is ALADIN (Augmented Lagrangian-based Alternating Direction Inexact Newton), proposed in Houska et al. (2016). It combines fast local NLP solvers with a global coordination step that uses curvature information (i.e., Jacobian and Hessians) to build a coupled quadratic program (QP). If suitable Hessian approximations are used, ALADIN guarantees local convergence with a quadratic convergence rate given a generic distributed nonconvex optimization problem. In the context of power systems, ALADIN has a key advantage: it does not require sharing full grid models, which makes it attractive for privacy-sensitive applications like inter-TSO coordination. Recent studies (Engelmann et al. 2019, Zhai et al. 2022) have demonstrated its scalability and robustness, both for transmission grids and in hybrid AC/DC networks.

In this chapter, we contribute a proof of concept that redispatch costs due to congestions, when calculated using the Shapley value, remain consistent even when the underlying OPF is solved using a distributed optimization method across multiple TSO regions.

The remainder of this chapter is structured as follows. Section 7.1 introduces the Shapley value algorithm in combination with a distributed OPF formulation and presents the distributed optimization method ALADIN. In Section 7.2, we apply the approach to a small IEEE test system and compare the results of the centralized and distributed OPF implementations. Finally, Section 7.3 concludes the chapter.

7.1 Methodology

To share the redispatch costs, we need to know the costs that individual congestions cause. As mentioned before, the cost share is not proportional to physical overload, but to the line's marginal impact on redispatch costs. Given the total system costs, the goal is to allocate these costs, i.e., the costs of the grand coalition, to the individual congested lines. The costs are computed by an OPF. We can compute the individual cost shares by going through all combinations of active congestions, taking the marginal contribution of one congestion to the specific configuration, and later averaging over them. This is the principle of the Shapley value. For every coalition, i.e., every configuration of congested lines, we have to compute an OPF. In this case, that is a distributed OPF, which we compute with the ALADIN algorithm. In the following, we present both the Shapley algorithm, as well as the distributed OPF algorithm.

Allocating Redispatch Costs with the Shapley Value

Let us repeat the Shapley value first. We are given a TU game $(\mathcal{P}, \Phi)$, where $\mathcal{P}$ is the set of congested lines, and the cost function Φ represents the OPF. The goal is to allocate the cost of the grand coalition (total redispatch costs) $\Phi(\mathcal{P})$ to each player (congested line) $p \in \mathcal{P}$. The Shapley value for a specific player p, as defined in Equation 6.3, is written as cf.(Shapley 1952)

$$\Psi_p(\Phi) = \sum_{\Omega \subseteq \mathcal{P} \setminus \{p\}} \frac{|\Omega|!\,(|\mathcal{P}| - |\Omega| - 1)!}{|\mathcal{P}|!} \left\{\Phi\left(\Omega \cup p\right) - \Phi\left(\Omega\right)\right\}, \tag{7.1}$$

where $\left\{\Phi\left(\Omega \cup p\right) - \Phi\left(\Omega\right)\right\}$ is the marginal contribution of player p to the configuration (coalition) Ω, that are weighted individually and summed collectively.

The workflow of computing the Shapley values with ALADIN is visualized in Figure 7.1. To compute the congested transmission lines, we perform three steps: First, we compute the optimal market scenario given the fixed demand and generation capacities. Second, we compute the power flows of that wishful

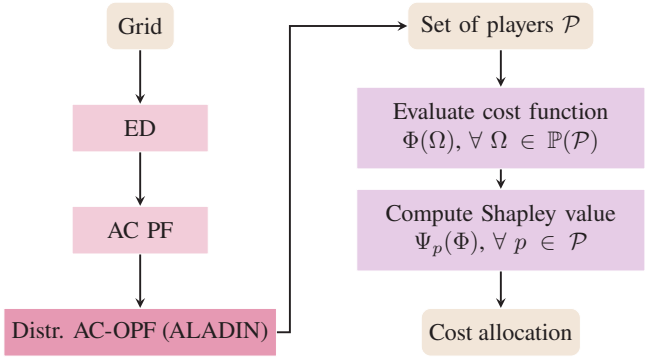

Figure 7.1: The Shapley algorithm for cost allocation with a distributed AC-OPF (ALADIN).

market scenario, assuming that there are no line limits. Finally, we compare these flows with the realistic power flows within the line capacities. In technical terms, we first compute the market scenario with an economic dispatch (ED), second, we use power flow to compute the respective power flows, and lastly, we compare those with the optimal power flow results, yielding the cost-optimal generation and power flows in the transmission grid. These steps are computed sequentially.

In the right part of Figure 7.1, we compute an OPF for every coalition of congested lines $\Omega \subset \mathcal{P}$, and with the resulting marginal contributions, the Shapley value for all congested lines. This gives us the share in redispatch costs per line. The algorithm differs from Voswinkel et al. (2022) in two ways: First, Voswinkel uses a DC-OPF, while we changed to AC-OPF. Second, they describe using a power flow only, given an optimal market scenario, while we do not assume an optimal scenario, but perform an economic dispatch optimization followed by a power flow computation.

The Centralized Optimization Problem

The cost function Φ for each coalition in the Shapley value algorithm is determined by solving a full non-linear AC Optimal Power Flow (OPF) problem. This OPF formulation captures both active and reactive power flows, along with network

constraints and component limits. Voltages are expressed in polar form, i.e., $V_i = v_i e^{\mathrm{j}\theta_i}$, where v_i is the voltage magnitude and θ_i is the phase angle at bus i. The decision variables include voltages, generation, and power flows: $x = (\theta,\, v,\, P_G,\, Q_G)$.

Let $\mathcal{L}^{\mathrm{cl}}$ be the set of congested lines. A coalition $\Omega \subseteq \mathcal{L}^{\mathrm{cl}}$, with its complement $\Omega^{\mathrm{c}} \subseteq \mathcal{L}^{\mathrm{cl}}$, represents the set of congested lines considered active, thermal limits are enforced only on $\tilde{\mathcal{L}} = \mathcal{L} \setminus \Omega^{\mathrm{c}}$. All other congested lines in the complement $\Omega^{\mathrm{c}} = \mathcal{L}^{\mathrm{cl}} \setminus \Omega$ are treated as unconstrained in that OPF run. This allows us to isolate the marginal cost contribution of each line.

The centralized AC-OPF is formulated following (Frank and Rebennack 2016):

$$\min_{x} \quad c(x) = \sum_{i \in \mathcal{N}} \left\{ a_i \left(P_{G,i}\right)^2 + b_i(P_{G,i}) + c_i \right\} \tag{7.2a}$$

$$\text{s.t. } P_{G,i} - P_{D,i} = v_i \sum_{k \in \mathcal{N}} v_k \left(G_{ik} \cos \Delta\theta_{ik} + B_{ik} \sin \Delta\theta_{ik}\right), \tag{7.2b}$$

$$Q_{G,i} - Q_{D,i} = v_i \sum_{k \in \mathcal{N}} v_k \left(G_{ik} \sin \Delta\theta_{ik} - B_{ik} \cos \Delta\theta_{ik}\right), \tag{7.2c}$$

$$P_{ij} = v_i^2 G_{ij} - v_i v_j \left(G_{ij} \cos \Delta\theta_{ij} + B_{ij} \sin \Delta\theta_{ij}\right), \tag{7.2d}$$

$$Q_{ij} = -v_i^2 G_{ij} - v_i v_j \left(G_{ij} \sin \Delta\theta_{ij} - B_{ij} \cos \Delta\theta_{ij}\right), \tag{7.2e}$$

$$P_{ij}^2 + Q_{ij}^2 \leq (\overline{S}_{ij})^2, \tag{7.2f}$$

$$\underline{v}_i \leq v_i \leq \overline{v}_i, \tag{7.2g}$$

$$\underline{P_{G,i}} \leq P_{G,i} \leq \overline{P_{G,i}}, \quad \underline{Q_{G,i}} \leq Q_{G,i} \leq \overline{Q_{G,i}}, \tag{7.2h}$$

$\forall i \in \mathcal{N}, (i,j) \in \tilde{\mathcal{L}}$, where c in Equation (7.2a) defines the quadratic generation cost function, constraints (7.2b) and (7.2c) enforce active and reactive power balance at each node, Equations (7.2d) - (7.2f) model the active and reactive line flows and enforce thermal limits only for lines within $\tilde{\mathcal{L}}$, and (7.2h) represents the bounds on voltage magnitudes and generator outputs. Note that we follow MATPOWER's π-model sign conventions for branch flows.

The feasible set for a coalition Ω is denoted by $\mathcal{X}(\Omega)$, which includes all variables x satisfying the constraints above. The respective cost for the coalition Ω and a cost function f is computed as:

$$x^*(\Omega) = \arg \min_{x \in \mathcal{X}(\Omega)} f(x), \tag{7.3}$$

$$\Phi(\Omega) := f(x^*(\Omega)). \tag{7.4}$$

The operation cost $\Phi(\Omega)$ serves as the characteristic function value in the Shapley value framework and represents the total redispatch cost resulting from enforcing constraints for only the lines in Ω.

The Distributed OPF

To solve the AC-OPF from Equation 7.2 in a distributed fashion, we reformulate it. Instead of disconnecting tie-lines between regions, as proposed in earlier work (Engelmann et al. 2019), we adopt a more physically consistent approach using *shared components* across regional boundaries. This ensures consistency in physical variables at the interfaces and allows for coordinated optimization without compromising data privacy. Respective algorithms are to be found in Dai et al. (2025).

Consequently, the AC OPF problem can be written as an *affinely coupled* distributed optimization problem with the set of regions $\mathcal{R}$:

$$\min_{x} \quad f(x) := \sum_{\ell \in \mathcal{R}} f_\ell(x_\ell) \tag{7.5a}$$

$$\text{s.t.} \quad \sum_{\ell \in \mathcal{R}} A_\ell x_\ell = b \quad | \ \lambda \tag{7.5b}$$

$$h_\ell(x_\ell) \leq 0 \quad | \ \kappa_\ell, \quad \forall \ell \in \mathcal{R} \tag{7.5c}$$

where Equation (7.5a) represents the separable objective function—typically the sum of local generation costs across all regions $\ell \in \mathcal{R}$, Equation (7.5b) contains the consensus constraints that enforce agreement on shared variables at regional boundaries (e.g., voltages or flows at tie-line buses), and Equation (7.5c) includes all local nonlinear constraints, such as power balance equations, line limits, and box constraints on voltages and generation within each region.

The dual variables λ and κ_ℓ correspond to the equality constraints (7.5b) and inequality constraints (7.5c), respectively. This formulation enables distributed solution techniques while ensuring that the overall physical model remains consistent. For further details on the formulation and decomposition approach, we refer to Mühlpfordt et al. (2021) and Dai et al. (2022).

Solving the Distributed OPF with ALADIN

Concept Among the available distributed nonlinear optimization methods, the ALADIN algorithm (Houska et al. 2016) is particularly well suited for problems of the form (7.5). It solves them through an iterative two-level process: in each iteration, local regions solve nonlinear programs (NLPs) in parallel using private data, followed by a coordination step that aligns shared variables through a quadratic program (QP). The local NLPs ensure physical feasibility within each region, while the central QP enforces consistency across regional boundaries. Thus, ALADIN combines the decomposition benefits of distributed optimization with the fast convergence of Newton-type methods.

Algorithm The ALADIN algorithm (Algorithm 1) consists of two main phases: the local NLP step 1 and the coordination QP step 4. In the local step, each region ℓ independently solves an augmented Lagrangian subproblem with objective function f_l that includes the penalty term ρ and scaling Σ_ℓ, ensuring that all local constraints h_l, such as power balances and line limits, are satisfied. In the subsequent coordination phase, the algorithm aligns the regional solutions through the coupled QP (7.8), which uses second-order sensitivity information (7.7). The penalty parameters ρ and μ control the balance between local accuracy and global

Algorithm 1 ALADIN

Input: z, λ, $\rho > 0$, $\mu > 0$ and scaling symmetric matrices $\Sigma_\ell \succ 0$
Repeat:

1. Solve the following decoupled NLPs for all $\ell \in \mathcal{R}$:

$$\min_{x_\ell} \quad f_\ell(x_\ell) + \lambda^\top A_\ell x_\ell + \frac{\rho}{2} \|x_\ell - z_\ell\|^2_{\Sigma_\ell} \tag{7.6a}$$

$$\text{s.t.} \quad h_\ell(x_\ell) \leq 0 \qquad | \ \kappa_\ell \tag{7.6b}$$

2. Compute the gradient g_ℓ, the Jacobian matrix J_ℓ of active constraints h^{act}_ℓ and the approximated Hessian H_ℓ at the local solution x_ℓ by

$$g_\ell = \nabla f_\ell(x_\ell), \ J_\ell = \nabla h^{\text{act}}_\ell(x_\ell), \ H_\ell \approx \nabla^2 \left\{ f_\ell(x_\ell) + \kappa_\ell^\top h_\ell(x_\ell) \right\} \succ 0 \tag{7.7}$$

3. Terminate if $\|Ax - b\|_2 \leq \epsilon$ and $\|\Sigma(x - z)\|_2 \leq \epsilon$ are satisfied.
4. Obtain $(p^{\text{qp}}, \lambda^{\text{qp}})$ by solving the coupled QP:

$$\min_{p^{\text{qp}}, s} \quad \sum_{\ell \in \mathcal{R}} \left\{ \frac{1}{2} (p^{\text{qp}}_\ell)^\top H_\ell \, p^{\text{qp}}_\ell + g_\ell^\top p^{\text{qp}}_\ell \right\} + \lambda^\top \, s + \frac{\mu}{2} \|s\|_2^2 \tag{7.8a}$$

$$\text{s.t.} \quad \sum_{\ell \in \mathcal{R}} A_\ell (x_\ell + p^{\text{qp}}_\ell) = b + s \quad | \ \lambda^{\text{qp}} \tag{7.8b}$$

$$J_\ell \, p^{\text{qp}}_\ell = 0, \ \ \ell \in \mathcal{R} \tag{7.8c}$$

5. Update the primal and the dual variables with the full step

$$z^+ = x + p^{\text{qp}} \quad \text{and} \quad \lambda^+ = \lambda^{\text{qp}} \tag{7.9}$$

consistency. The symmetric, positive-definite matrices Σ_ℓ improve numerical conditioning; in well-scaled OPF problems, they can be set to the identity matrix. The dual variable λ corresponds to the consensus constraints (7.5b). The slack variable s and penalty μ maintain the feasibility of the consensus constraints even when the local NLPs are not perfectly synchronized. By leveraging this curvature information, ALADIN achieves locally quadratic convergence under standard regularity assumptions (Engelmann et al. 2019, Houska and Jiang 2021).

Complexity Compared with simpler first-order methods such as ADMM, ALADIN requires more communication per iteration, since each region must transmit gradients g_ℓ, Jacobians J_ℓ, and Hessian approximations H_ℓ to the central coordinator. The coordination QP is computationally more involved than the averaging step in ADMM, but the richer second-order information typically yields convergence in far fewer iterations, compensating for the additional effort (Mühlpfordt et al. 2021, Dai et al. 2022).

From a computational perspective, the distributed AC OPF formulation has a slightly increased problem size due to duplicated boundary variables and additional *consensus constraints*. Each region R_i solves an NLP with $2N_b^{R_i} + 2N_g^{R_i}$ decision variables and $2N_b^{R_i}$ equality constraints, while the coordinator enforces about $2N_\mathrm{c}$ consensus equalities for coupling buses or tie-lines. This enables parallelization across regions, so that the overall computation time scales mainly with the size of the largest region and the number of its decision variables. Table 7.1 summarizes the relative scaling characteristics of centralized and distributed OPF formulations (Mühlpfordt et al. 2021).

Table 7.1: Comparison of centralized and distributed AC OPF complexity.

Aspect	Centralized OPF	Distributed OPF (ALADIN)
Variables	$\mathcal{O}(2N_b + 2N_g)$	$\mathcal{O}\Big(\sum_i (2N_b^{R_i} + 2N_g^{R_i})\Big)$
Equalities	$\mathcal{O}(2N_b)$ (PBE)	$\mathcal{O}(2N_b^{R_i}) + \mathcal{O}(2N_c)$ consensus
Per-iteration cost	One solve	Parallel NLPs + coordination QP
Communication	None	Exchange of g_i, J_i, H_i and dual variables per iteration

In summary, the distributed formulation has slightly more variables for coupling, but thereby enables parallel computation and scalability. When the regions are loosely connected, ALADIN can achieve similar or faster and equally robust convergence than a centralized solver while preserving local feasibility and data privacy.

7.2 Illustrative Example

As a case study, we use the standard IEEE 9-bus system, shown in Figure 7.2. Some grid parameters have been modified to induce congestion. All modifications are given in Table 7.2.

Setting The grid is partitioned into two regions, representing different transmission grids: $\mathcal{R}_1 = \{1, 4, 5, 9\}$ and $\mathcal{R}_2 = \{2, 3, 6, 7, 8\}$, see Figure 7.2a. The partitioning and distributed OPF setup are implemented using the open-source toolbox RAPIDPF (Mühlpfordt et al. 2021)[2].

Implementation All simulations are run in Matlab R2021a on a standard desktop equipped with an `Intel® i5-6600K CPU @ 3.50GHz` and 32 GB RAM. The modeling is done using the CasADi toolbox (Andersson et al. 2019),

[2] Available at `https://github.com/xinliang-dai/rapidPF`

Table 7.2: Modifications of IEEE case9 for the robustness analysis.

Component	Parameter	Changes
Branch $l \in \mathcal{L}$	RateA[1] $\overline{S}_{ij}$	70 for $l = 1$, 40 for $l = 4$
	RateB/C	set to 0 for all lines
	Angle limits	set to $[-60°, 60°]$ for all branches
Generators $i \in \mathcal{G}$	Cost coeff. b_i	$b_1 = 32, b_2 = 25, b_3 = 20$
	$\overline{P}_{G,i}$	1000.0 for all $i \in \mathcal{G}$ (sufficiently high)
Loads $i \in \mathcal{D}$	Location / $P_{D,i}$	$d_5 = 90, d_7 = 100, d_9 = 125$
	Other buses	no loads assigned

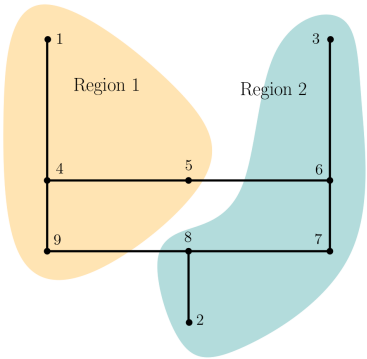

(a) Regions of system operators.

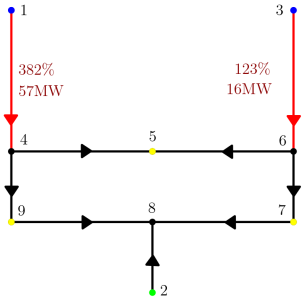

(b) Simulation results (red = congested lines, blue/green = generator ramping up/down, yellow = load).

Figure 7.2: IEEE 9-bus test grid: Partitioning and simulation results.

and the nonlinear programs are solved using IPOPT (Wächter and Biegler 2006). For comparison, the centralized OPF reference is computed using the default solver provided in Matpower.

Shapley Values

Figure 7.2b shows the OPF results of the test case. Two transmission lines $\mathcal{L}^{\text{cl}} = \{(1,4),(3,6)\}$ are congested with flow limits of {20, 70} MW respectively. They experience overloads of {57, 16} MW, corresponding to {382, 123} %. The system includes three generators located at buses $\mathcal{G} = \{1,2,3\}$, producing {72, 163, 85} MW respectively. Accounting for losses, this generation matches the total system demand of $\sum_i P_{D,i} = 315\,\text{MW}$, at buses $i \in \mathcal{D}$ ={5, 7, 9}.

The resulting Shapley values for the congested lines are $\Psi_1 = 424, \Psi_2 = 135$, respectively. These values allocate the total redispatch costs proportionally to each line's contribution to congestion. While they roughly reflect the relative overloads, the cost attributed to region $\mathcal{R}_1$ is slightly higher. This effect becomes more prominent in larger or more complex networks.

Centralized vs. Distributed Computation

Since the Shapley value is based on repeated evaluations of the AC OPF, the accuracy of the OPF solutions significantly affects the cost allocation results, cf. (6.3).

Metrics To validate the distributed approach using ALADIN, we compare the results with those from the centralized Matpower solver using two metrics: The deviation of the solution

$$\|x - x^*\|_2\,, \tag{7.10}$$

and the relative solution gap

$$\left|\frac{f(x^*) - f(x)}{f(x^*)}\right|, \tag{7.11}$$

where x^* and $C(x^*)$ denote the solution and objective value obtained from the centralized solver.

Results Table 7.3 summarizes the numerical results. For all evaluated coalitions, ALADIN converges in just seven iterations, yielding highly accurate solutions. The solution gap remains below 10^{-6}, confirming that distributed computation does not impact the reliability of the Shapley value calculation.

Table 7.3: Comparison between centralized and distributed OPF solutions

Coalition Ω	Iterations	Time [s]	$\|x - x^*\|_2$	Solution Gap
$\{\emptyset\}$	7	0.129	4.54×10^{-4}	2.19×10^{-6}
$\{(1,4)\}$	7	0.128	7.82×10^{-6}	4.60×10^{-7}
$\{(3,6)\}$	7	0.131	9.90×10^{-4}	6.04×10^{-8}
$\{(1,4),\ (3,6)\}$	7	0.129	1.135×10^{-6}	9.54×10^{-8}

Figure 7.3 shows the convergence behavior of ALADIN for the grand coalition $\Omega = \mathcal{L}^p = \{(1,4),(3,6)\}$. The algorithm rapidly converges to a high-precision solution in terms of both primal and dual residuals, state variable deviation, and objective value. This confirms that ALADIN is suitable for distributed OPF evaluation in the Shapley value framework, even in the presence of coupling across regional boundaries.

7.3 Conclusion

In this chapter, we proposed a distributed method for calculating the Shapley value to allocate redispatch costs arising from grid congestion. By extending the original idea with a full non-linear AC OPF formulation, the approach ensures a more realistic and fair allocation of costs in comparison to simplified DC models, which may lack AC feasibility in practical settings. Additionally, the use of the distributed optimization algorithm ALADIN enables system operators to compute redispatch responsibilities across multiple regions without exposing sensitive grid data, thereby preserving data privacy.

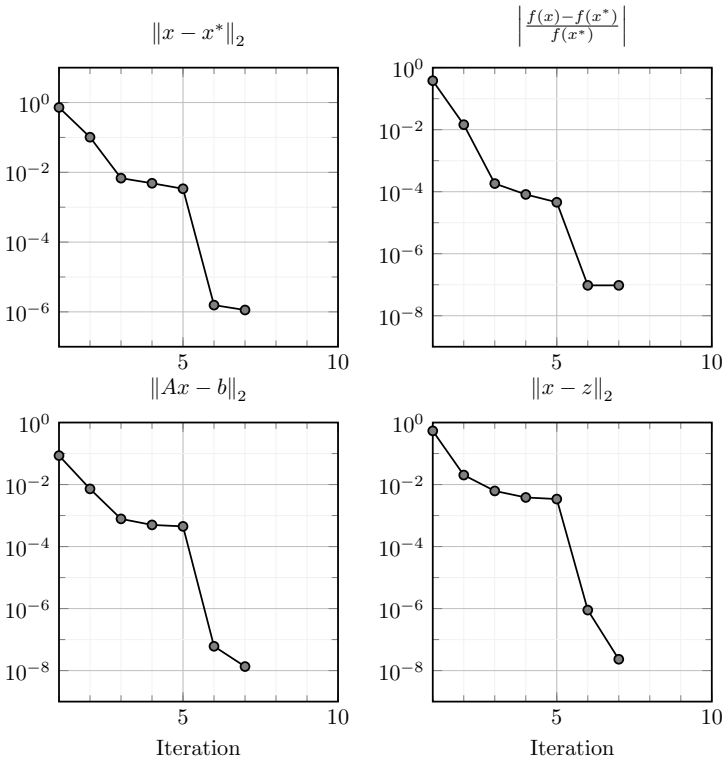

Figure 7.3: Convergence behaviour of ALADIN for the grand coalition $\Omega = \mathcal{P}$

The simulation results on an IEEE 9-bus test system demonstrate that the distributed Shapley value approach yields results with equal precision to a centralized reference, while also being computationally efficient. These findings confirm the suitability of the method for real-world applications, particularly in a highly interconnected and dynamic grid environment.

Given the increasing need for explainability, transparency, and fair cost allocation in the evolving energy system, this method contributes a promising tool for grid operators, especially TSOs, facing the complexity of congested, multi-actor power systems. Future work includes extending this approach to larger systems,

incorporating distribution-level grids, and developing scalable approximations for both the OPF problem and the Shapley value.

8 Comparison of AC vs. DC-based Cost Allocation

Publication reference for this chapter

Bauer, R. and Dai, X. and Hagenmeyer, V. (2024). "Industrial Application of the Shapley value-based Redispatch Cost Allocation to Large-Scale Power Grids requires AC Optimal Power Flow". *2024 IEEE Power & Energy Society General Meeting (PESGM)*, p. 1-5. DOI: 10.1109/PESGM51994.2024.10688852

The previous chapter showed that redispatch costs can be fairly allocated using the Shapley value—even when OPF is solved in a distributed, privacy-preserving manner using the full AC formulation. However, in the process, we noticed that results based on AC-OPF can differ substantially from those based on DC-OPF, both in terms of congestion patterns and Shapley values. These differences cannot be attributed solely to additional losses: AC-OPF solutions are not necessarily more expensive, nor do they always produce more congested transmission lines.

Such discrepancies are relevant for both fairness in cost allocation and long-term grid planning. For example, if congestion locations differ between models, resulting decisions on grid reinforcements will also diverge. Thus, a fair cost allocation requires not only tractability but also a sufficiently accurate representation of grid physics.

Since the Shapley value is typically applied using DC-OPF —both in studies and operational tools—this raises the question of whether DC-OPF remains appropriate given the complexity of today's grid flows. A further limitation of the previous

chapter was its illustrative test case, which did not address scalability to larger, meshed AC grids.

Accordingly, this chapter shifts focus from *how* OPF is solved to *what* physical model it is based on—and how well the overall approach scales. This leads to our central research question:

RQ4 *How does the use of AC-OPF affect the results and fairness of the Shapley value compared to DC-OPF?*

Because the observed differences between Shapley values based on AC-OPF versus DC-OPF are neither systematic nor easy to predict, we extend the analysis to a range of meshed grids of varying size and topology. This raises the question: *do these differences also appear on larger, meshed grids?*

Section 8.1 shortly formulates the Shapley-based cost allocation with AC-OPF and outlines the computational setup for scaling. Section 8.2 presents numerical results on small and large systems, contrasting DC and AC outcomes. Section 8.3 summarizes insights and implications for application.

8.1 Methodology

We build directly on the previous chapter by using the Shapley value to allocate total redispatch costs to congested lines. The AC-OPF formulation follows the exact polar representation as in the DC case. In this section, we summarize the setup and highlight differences between the DC and AC approaches, particularly in how costs are allocated and how scaling plays a role in both formulations.

Grid and Players

Let the transmission grid be $\mathcal{A} = (\mathcal{N}, \mathcal{L})$ with a set of buses $\mathcal{N}$ and branches $\mathcal{L}$. Congested lines form the player set $\mathcal{P} \subseteq \mathcal{L}$, where each player $p = (i, j)$ represents a transmission line $p \in \mathcal{L}$. Coalitions are defined as sets of simultaneously active

congested lines, and are contained in the power set of players, i.e., $\Omega \in \mathfrak{P}(\mathcal{P})$. The characteristic cost function $\Phi : \mathfrak{P}(\mathcal{P}) \to \mathbb{R}_{\geq 0}$ maps each coalition to the resulting redispatch cost computed by the AC-OPF. This framework builds on the fact that redispatch costs vary depending on the specific lines involved and the congestion in the network, making the Shapley value an ideal method to allocate these costs fairly.

Shapley Value for Redispatch Costs

Given the players $\mathcal{P}$ and the OPF cost function Φ, we use the same cooperative game $(\mathcal{P}, \Phi)$ as before. Again, the Shapley value $\Psi_p(\Phi)$ assigns the cost of the grand coalition $\Phi(\mathcal{P})$ to each congested line p based on its average marginal contribution across all possible coalitions. Specifically, the marginal contribution of a line is calculated by considering how much the coalition's redispatch cost increases when the line is added to the coalition. This is expressed as:

$$\Psi_p(\Phi) = \sum_{\Omega \subseteq \mathcal{P} \setminus \{p\}} \frac{|\Omega|!\,(|\mathcal{P}| - |\Omega| - 1)!}{|\mathcal{P}|!} \Big\{ \Phi(\Omega \cup \{p\}) - \Phi(\Omega) \Big\}. \tag{8.1}$$

Operationally, we first determine the set of congested lines $\mathcal{P}$ by comparing the power flow results with the network-feasible OPF solution. The power flows are computed in two steps: an Economic Dispatch (ED) step determines the optimal (topology-unaware) generation, followed by a Power Flow (PF) computation to determine the actual line flows. The ED and PF are used solely to detect congested lines, with the actual redispatch costs computed from the AC/DC-OPF. Note that this differs slightly from the method presented in Bauer et al. (2024), which used only power flow computation. However, this approach is insufficient as the initial generation values may not represent the optimal market dispatch. Hence, in this thesis, we adopt this corrected method to better reflect real-world conditions.

For each coalition $\Omega \subseteq \mathcal{P}$, we solve an OPF where only the lines in the coalition Ω enforce thermal limits, while the remaining lines (players) $\mathcal{P} \setminus \Omega$ are unconstrained.

This procedure allows us to compute the marginal contributions with the cost function $\Phi(\cdot)$ for each coalition and obtain the Shapley values by averaging these contributions across all possible coalitions.

The full process is illustrated in Figure 8.1, which outlines the method from initial power flow calculations to the final cost allocation.

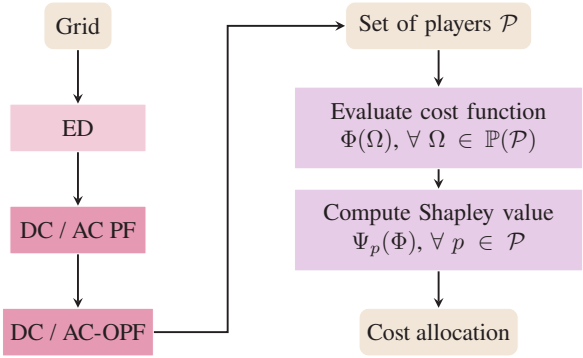

Figure 8.1: The Shapley algorithm with cost allocation based on DC and AC PF and OPF.

AC-OPF Formulation

We use the AC-OPF formulation from the last chapter. For each coalition $\Omega \subseteq \mathcal{P}$ in the Shapley procedure, the characteristic cost $\Phi(\Omega)$ is obtained from a full non-linear AC optimal power flow. Voltages are in polar form $V_i = v_i e^{\mathrm{j}\theta_i}$, and the decision vector is $x = (\theta, v, p^g, q^g)$. To isolate marginal effects, only lines in

$$\tilde{\mathcal{L}} \;=\; \mathcal{L} \setminus \big(\mathcal{P} \setminus \Omega\big)$$

retain their thermal limits in that OPF run; players in the complement are unconstrained. We follow Frank and Rebennack (2016) and, using MATPOWER's

π-model sign conventions for branch flows as previously, we write the centralized AC-OPF as

$$\min_{x} \quad c(x) = \sum_{i \in \mathcal{N}} \left\{ a_i \left(P_{G,i}\right)^2 + b_i(P_{G,i}) + c_i \right\} \tag{8.2a}$$

$$\text{s.t. } P_{G,i} - P_{D,i} = v_i \sum_{k \in \mathcal{N}} v_k \left(G_{ik} \cos \Delta\theta_{ik} + B_{ik} \sin \Delta\theta_{ik}\right), \tag{8.2b}$$

$$Q_{G,i} - Q_{D,i} = v_i \sum_{k \in \mathcal{N}} v_k \left(G_{ik} \sin \Delta\theta_{ik} - B_{ik} \cos \Delta\theta_{ik}\right), \tag{8.2c}$$

$$P_{ij} = v_i^2 G_{ij} - v_i v_j \left(G_{ij} \cos \Delta\theta_{ij} + B_{ij} \sin \Delta\theta_{ij}\right), \tag{8.2d}$$

$$Q_{ij} = -v_i^2 G_{ij} - v_i v_j \left(G_{ij} \sin \Delta\theta_{ij} - B_{ij} \cos \Delta\theta_{ij}\right), \tag{8.2e}$$

$$P_{ij}^2 + Q_{ij}^2 \leq (\overline{S}_{ij})^2, \tag{8.2f}$$

$$\underline{v}_i \leq v_i \leq \overline{v}_i, \quad \underline{P_{G,i}} \leq P_{G,i} \leq \overline{P_{G,i}}, \quad \underline{Q_{G,i}} \leq Q_{G,i} \leq \overline{Q_{G,i}}, \tag{8.2g}$$

$\forall i \in \mathcal{N}, (i,j) \in \tilde{\mathcal{L}}$, where $\theta_{ij} = \theta_i - \theta_j$, $G_{ij} + \mathrm{j}B_{ij}$ are elements of the bus-admittance matrix, and $\overline{s}_{ij}$ are the apparent power limits on $\tilde{\mathcal{L}}$. Constraints (8.2b)–(8.2c) impose nodal active/reactive power balance; (8.2d)–(8.2f) define AC branch flows and thermal limits; and (8.2g) enforces bounds on voltages and generator outputs.

8.2 Results

We study how the choice of the OPF model (DC vs. AC) influences three outputs of the Shapley procedure under fixed loads: the set of congested lines, the redispatch costs, and the resulting Shapley values. We begin with small systems to show the basic effects, then move to large, meshed grids where scale and topology matter.

Setup We use networks from 9 up to 2383 buses, mostly from the PGLib library (Babaeinejadsarookolaee et al. 2019), see Table 8.1. These cases are derived from standard IEEE systems with mildly adjusted parameters, including generation costs. For each case, we induce multiple congestions by altering load and thermal limits (Appendix Section A.3) and report representative instances here.

Table 8.1: Data and test systems used in Chapter 8.

Data Type	Details
Grids	IEEE 9, 39, 118, 300, 793, 1354-bus, PGLib 2382wp, ACTIVSg10k (TAMU)

Table 8.2: Shapley allocations with DC-OPF and economic dispatch (Julia).

Cases	Lines	Congested lines	System costs ($)	Redispatch costs ($)	Shapley Values ($)	Runtime (min)
case9	9	{2,4,5}	6,566	**266**	**{182, 25, 59}**	00:00:56
case39	39	{2,4}	5,334	48	**{27,21}**	00:00:49
case118	186	{106,141,163}	93,132	105.3	**{46, 1.3, 58}**	00:16:36
case300	411	{394,400}	707,405	**1,112**	{401,711}	00:01:14
case793	913	**{188,324,338,399,616,910,911}**	253,891	**88.7**	{0,0,0,0,**65,17,6.7**}	00:26:00
case1354	1,991	{86,167,227,230,297}	1,177,118	3,526	**{256,104,2058,246,862}**	00:01:42
case2383	2,896	{169,292,321,322}	1,769,943	**1,464**	{**926,538**,0,0}	00:01:42

Coordinates for the larger grids are generated with the yEd software (yWorks GmbH 2019). In all plots, generators are shown in green, loads in blue, and line thickness encodes flow magnitude. The exact results for congestions, redispatch costs, and Shapley values are given in Tables 8.2–8.3 for DC and AC-OPF, respectively, with the biggest differences marked in bold.

Implementation Computations are performed in MATLAB R2022b using MATPOWER (The MathWorks 2021) on a desktop (`Intel® i5-6600K @ 3.50 GHz`, 32 GB RAM), with the CasADi toolbox (Andersson et al. 2019), and the nonlinear programs are solved using IPOPT (Wächter and Biegler 2006).

Small-scale systems: Two effects of AC-OPF on the Shapley values

Our first result is qualitative: AC-OPF can change flows enough to alter which congestions are costly, and by how much. This is not just a mere refinement of DC-OPF, as it can flip which line is deemed responsible.

Table 8.3: Shapley allocations with AC-OPF and economic dispatch (Julia).

Cases	Lines	Congested lines	System costs ($)	Redispatch costs ($)	Shapley Values ($)	Runtime (min)
case9	9	{2,4,5}	6,773	**168**	**{105,22,41}**	00:01:25
case39	39	{**1**,2,4}	5,666	293	**{4,181,108}**	00:11:00
case118	186	**{105,106,141,163}**	97,213	330	**{43,201,0,86}**	**02:50:51**
case300	411	{394,400}	720,612	**886**	**{336,550}**	00:05:36
case793	913	{324,399,616}	255,547	**0**	{0,0,0}	00:12:00
case1354	1,991	**{86,167,227,230,297,829}**	1,216,700	3,234.05	**{77,205,2018,23,911,0.05}**	02:32:20
case2383	2,896	{169,292,321,322}	1,858,494	**60**	{**0,60**,0,0}	**15:16:43**

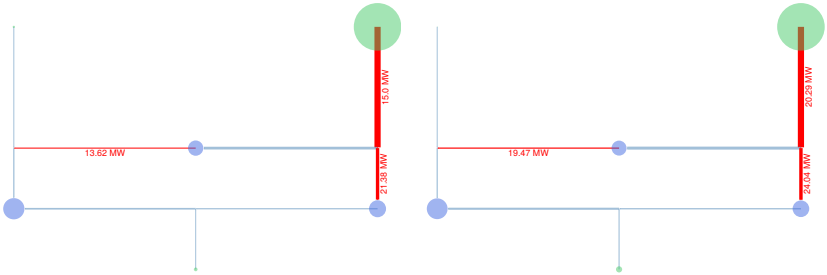

Figure 8.2: Case9: Overloaded lines (red) in DC-OPF (left) and AC-OPF (right), with power flows (blue, flow indicated by width), and generation (green) and load (blue) nodes.

9-bus example Figure 8.2 compares DC-OPF (left) and AC-OPF (right) for the same IEEE 9-bus case. Both models flag the same three lines $\mathcal{L}^{\text{cl}}\{2, 4, 5\}$ as congested, but assign different importance scores and redispatch costs. This shows that AC-OPF can still shift cost attribution even if the active constraints remain unchanged.

The Shapley allocations differ accordingly. Under DC, the Shapley values are distributed as {182, 25, 59}, whereas under AC, they become {105, 22, 41}. Despite identical overloads, the importance of each line to the system cost shifts notably. The overloads are computed from economic dispatch and PF, with values of 315 MW at bus 1 under DC and 324 MW under AC. With limits {70,

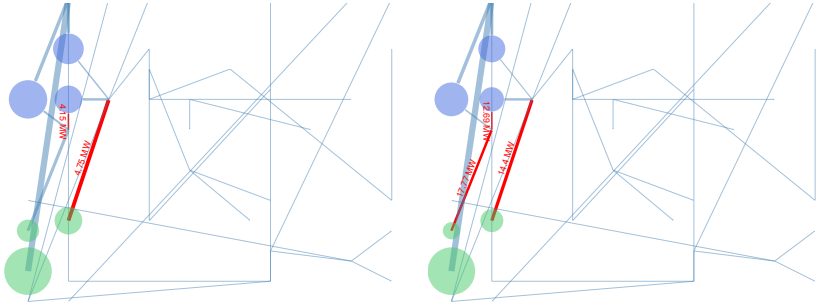

Figure 8.3: Case39: Overloaded lines (red) in DC-OPF (left) and AC-OPF (right), with power flows (blue, flow indicated by width), and generation (green) and load (blue) nodes.

40} MW, the implied overloads are {245.0,100.2} MW and {261.4, 105.7} MW, respectively. After redispatch, the flows change to {13.1, 40.0} in DC and {70.0, 15.6} in AC.

Two effects stand out. First, total redispatch costs differ substantially; AC-OPF yields *lower* redispatch costs, counter to the intuition that AC is always more expensive due to losses. Second, the cost attribution among the same set of congested lines shifts significantly. These changes arise from topology-dependent flow redistribution under AC constraints. Extrapolating DC-based allocations can therefore be misleading, even on small systems.

Large-scale systems: more and different changes

On large, meshed grids, the same message persists. AC-OPF does not simply scale DC-OPF; it can change the number of congestions, the pattern of redispatch, and the Shapley values—sometimes in directions opposite to expectation. Even runtimes are not uniformly higher for AC-OPF (cf. case793).

Tables 8.2-8.3 summarize the results from IEEE test grids with 9 to 2383 buses. Figure 8.3 shows an early case (39-bus) where AC-OPF introduces additional congestions and drastically alters cost attribution. Figure 8.4 confirms the same

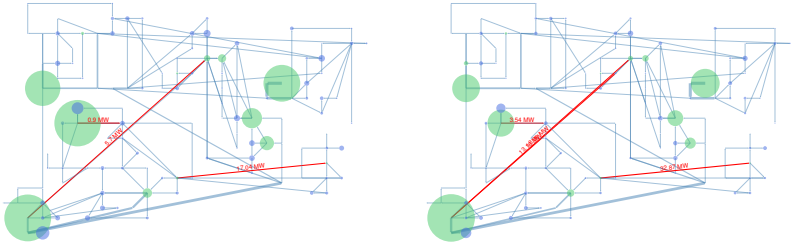

Figure 8.4: Case118: Overloaded lines (red) in DC-OPF (left) and AC-OPF (right), with power flows (blue, flow indicated by width), and generation (green) and load (blue) nodes.

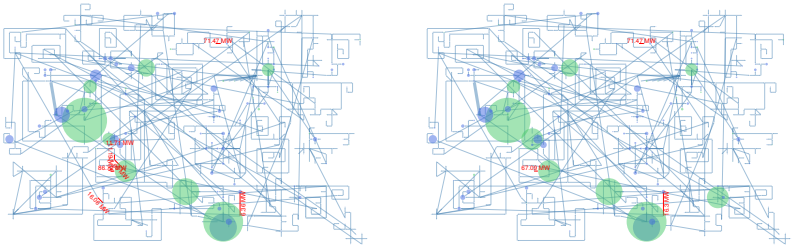

Figure 8.5: Case3793: Overloaded lines (red) in DC-OPF (left) and AC-OPF (right), with power flows (blue, flow indicated by width), and generation (green) and load (blue) nodes.

trend in a larger grid, where both the number and the identity of congested lines shift. In contrast, Figure 8.5 highlights the opposite: AC-OPF reports fewer congestions and zero redispatch cost. Together, these examples show that AC effects are not uniform but depend on topology and grid configuration. Since the AC vs. DC differences are non-monotonic and topology-dependent, DC results cannot be corrected by simple scaling factors or heuristics. Some trends are familiar (often higher redispatch under AC), but two additional effects are noteworthy. We highlight them below using specific cases from Figures 8.3-8.5.

Different number of congestions AC-OPF frequently yields *more* congestions than DC-OPF, though not consistently. In IEEE case39 and case118, the number and identity of congested lines expand under AC-OPF. Parity occurs in the IEEE case300, and the reverse is possible: In the PGLib case793, AC-OPF reports only three congestions versus seven under DC and, crucially, zero redispatch cost, meaning the OPF schedule coincides with the market schedule for the active limits. One plausible explanation is that AC feasibility constraints already reshape generation locationally before line limits bind, as in DC. However, the precise workings are topology-dependent and thus cannot be explained precisely. In the PGLib case2383, AC has *more* congestion but still *lower* redispatch cost than DC. In these cases, AC feasibility shifts generation enough so that the remaining active constraints are naturally satisfied, whereas DC enforces a flow pattern that requires redispatch.

Shapley is not proportional to overload Many Shapley values are zero, even though the corresponding lines show non-zero overload. A line can be heavily overloaded yet irrelevant for redispatch if its removal or enforcement does not change the optimal dispatch—its marginal contribution is zero. Interpreted as importance scores (as in XAI), the Shapley value therefore highlights only those congestions that actually drive system cost under the given market outcome and capacities.

This is seen clearly in case793 (Figure 8.5): DC assigns cost to five lines, while AC reports zero Shapley values despite similar flows. This reflects how different grid physics affect the marginal cost impact of each line, and that load alone does not determine cost responsibility.

8.3 Conclusion

Redispatch costs continue to rise, making both their exact computation and their equitable distribution increasingly important. The Shapley value has been proposed as a fair allocation rule and demonstrated on small, concatenated test systems; however, existing redispatch studies typically rely on DC-OPF. This work asks how the choice of power flow model—DC versus AC—affects the Shapley allocation and evaluates the approach on large, meshed transmission systems.

Our results show that AC-OPF can materially change all three outputs of the Shapley procedure: which lines are congested, the total redispatch costs, and the Shapley values themselves. Across a range of systems from 9 to 2383 buses, we observe consistent deviations between DC and AC results—sometimes subtle, sometimes substantial—as illustrated in Figures 8.3-8.5. Crucially, these differences are not systematic. AC-OPF does *not* always produce more congestion, higher redispatch costs, or larger allocations. The direction and magnitude of changes depend on topology and AC feasibility effects, which means DC-based results cannot simply be extrapolated to real AC grids. We also observe substantial variability in Shapley values, including many zeros, highlighting that high loading does not necessarily translate into cost responsibility.

For research and TSO practice alike, we recommend using AC-OPF as the basis for Shapley-based redispatch cost allocation, especially on large, meshed networks.

For future work, several extensions are plausible. First, real-world case studies, for example, on the German transmission grid, would validate the findings at an operational scale. However, after this work had been completed, another study by Voswinkel (2023) was published that applies the Shapley value on the German TG using DC-OPF with a speed-up method to compute the Shapley values. Following the results from this paper, it would be interesting to repeat this simulation with AC-OPF. Second, a systematic comparison of meshed versus concatenated (e.g., transmission vs. distribution) topologies could clarify how network structure affects allocations. Finally, incorporating flexibilities such as battery storage would quantify congestion relief and the ensuing reduction in redispatch costs.

9 Extending Shapley towards Utility

Publication reference for this chapter

Bauer, R. and Dai, X. and Zahn, F. and Hagenmeyer, V. (2025). "Shapley value-based cost allocation for Battery Energy Storage Systems in Power Grids with a High Share of Renewables". *Proceedings of the 16th ACM International Conference on Future and Sustainable Energy Systems*, p. 650-655. DOI: 10.1145/3679240.3734664

Battery Energy Storage Systems (BESS) are increasingly seen as key assets for operating power systems with high shares of renewable generation. Their main advantage is additional capacity and thus short-term flexibility, e.g., to shift load in time, smooth renewable variability, and support ancillary services like reactive power compensation (Hu et al. 2022, Ayesha et al. 2024, Blair et al. 2022, Tookanlou et al. 2023). As redispatch costs rise and congestion becomes a routine challenge, BESS are expected to reduce operational costs and relieve stress on the grid (Dehnavi et al. 2019, Nguyen et al. 2024).

However, the extent to which a specific BESS unit contributes to these goals is not straightforward to quantify. In meshed AC transmission grids, power flows depend on nonlinear interactions and the system-wide impact of a single unit may not align with its local energy throughput. This raises the question of how to assess and compare the usefulness of individual storage units—not just by their dispatch, but by their effect on system performance over time.

In this chapter, we propose a way to quantify the operational *utility* of BESS based on the *Shapley value* (Lipovetsky 2020), which we have discussed in the previous Chapters 6, 7, and 8 and that has appeared in recent publications (Voswinkel 2023, Bauer et al. 2024). In this chapter, we adapt the Shapley value for Application 2 (see Chapter 6 on Shapley fundamentals): to evaluate the contribution of storage units to system cost reduction and constraint relief across multiple time periods, addressing the research question

RQ5 *How can the Shapley value be used to quantify the utility of individual BESS units in the transmission grid?*

This includes not only active power effects, but also reactive power and grid interactions. Compared to previous work, we shift the focus from allocating costs between actors or regions to assessing utility at the component level. BESS are treated as the players in a cooperative game whose value function is based on the cost outcomes of a multi-period AC-OPF.

The chapter proceeds as follows: We first introduce the OPF-based grid and storage model, then define the Shapley utility measure in this context. We demonstrate the method on both radial and meshed test systems and discuss how the results reflect the system-level contribution of each BESS unit.

9.1 Methodology

This section outlines the modeling and computation framework for quantifying the utility of distributed battery energy storage systems (BESS) by applying the Shapley value to an Optimal Power Flow (OPF) problem. Each BESS is treated as an individual actor, and its impact on system operation is evaluated based on its contribution to total cost reduction over a multi-period optimization horizon.

The OPF is formulated as a multi-period AC problem, as the benefits of storage only manifest over time. Unlike previous Chapters 6 and 7, where the Shapley value was used for cost allocation between TSOs, we repurpose it here as a utility

measure for individual BESS units. The OPF formulation and Shapley setup are reintroduced for completeness, but kept concise to avoid redundancy.

AC-OPF Formulation

The system behavior is modeled using a multi-period AC optimal power flow (MP-OPF) including battery storage units, as their value unfolds over time. At each time step $t \in \mathcal{T}$, the objective is to minimize total generation costs subject to physical grid constraints and operational limits on all components.

The decision variables include the voltage magnitude and angle (v_i^t, θ_i) at each bus $i \in \mathcal{N}$, the active and reactive generation $(P_{G,i}^t, Q_{G,i}^t)$ for generators $i \in \mathcal{G}$, and the active and reactive storage injections $(P_{S,i}^t, Q_{S,i}^t)$ for storage units $i \in \mathcal{S}$.

Generator cost is modeled as a quadratic function $C_{G,i} = c_i + b_i \cdot P_{G,i}^t + a_i \cdot (P_{G,i}^t)^2$, while curtailment and storage costs (e.g., investment and usage costs) can optionally be included. In this setting, storage costs are set to zero.

The total system cost is given by:

$$C = \sum_{t \in \mathcal{T}} \left(\sum_{i \in \mathcal{G}} C_{G,i} + \sum_{i \in \mathcal{D}^{\text{RES}}} C_{Curt,i} + \sum_{i \in \mathcal{S}} C_{S,i} \right), \tag{9.1}$$

with zero storage cost, i.e., $C_{S,i} = 0$.

This objective is subject to a set of operational and physical constraints at each bus $i \in \mathcal{N}$ and time step $t \in \mathcal{T}$. First, the power flow equations sum active and reactive power from generation, storage, demand, and RES generation:

$$P^t_{G,i} + P^t_{S,i} - P^t_{D,i} - (P^{RES,t}_{D,i} - P^t_{Curt,i}) \tag{9.2a}$$

$$= \sum_{j \in \mathcal{N}} v^t_i v^t_j \left(G_{ij} \cos(\theta^t_{ij}) + B_{ij} \sin(\theta^t_{ij}) \right), \tag{9.2b}$$

$$Q^t_{G,i} + Q^t_{S,i} - Q^t_{D,i} - (Q^{RES,t}_{D,i} - Q^t_{Curt,i}) \tag{9.2c}$$

$$= \sum_{j \in \mathcal{N}} v^t_i v^t_j \left(G_{ij} \sin(\theta^t_{ij}) - B_{ij} \cos(\theta^t_{ij}) \right), \tag{9.2d}$$

as well as the standard operational limits for generators, curtailment, voltages, and line flows:

$$\underline{P}_{G,i} \leq P^t_{G,i} \leq \overline{P}_{G,i}, \tag{9.3a}$$

$$\underline{Q}_{G,i} \leq Q^t_{G,i} \leq \overline{Q}_{G,i}, \tag{9.3b}$$

$$0 \leq P^t_{Curt,i} \leq \overline{P}^t_{Curt,i}, \tag{9.3c}$$

$$(F^t_{ij})^2 + (F^t_{ji})^2 \leq \overline{S}^2_{ij}, \tag{9.3d}$$

$$\underline{v}_i \leq v^t_i \leq \overline{v}_i. \tag{9.3e}$$

Storage Model

The storage model follows Geth et al. (2020) and introduces a new set of variables and constraints to describe charging, discharging, and changes in the State of Energy (SoE) of storage units at buses $s_i \in \mathcal{S}$ over the time horizon $\mathcal{T}$.

At each time step, the active power injection from a storage unit is defined as:

$$P_{S,i}^{t} = P_{S,i}^{t,CH} - P_{S,i}^{t,DC}, \tag{9.4}$$

where $P_{S,i}^{t,CH}$ and $P_{S,i}^{t,DC}$ denote the charging and discharging power, respectively. To prevent simultaneous charging and discharging, the model includes a complementarity condition:

$$P_{S,i}^{t,CH} \cdot P_{S,i}^{t,DC} = 0. \tag{9.5}$$

In practice, this is implemented via a nonlinear constraint rather than a binary decision variable, thereby avoiding mixed-integer formulations while preserving the physical requirement.

The storage state of energy evolves across time steps as:

$$E_{S,i}^{t} = E_{S,i}^{t-1} \cdot \eta_{S,i}^{SDC} + \Delta t \cdot \left(\eta_{S,i}^{CH} \cdot P_{S,i}^{t,CH} - \frac{1}{\eta_{S,i}^{DC}} \cdot P_{S,i}^{t,DC} \right), \tag{9.6}$$

where $\eta_{S,i}^{CH}$, $\eta_{S,i}^{DC}$, and $\eta_{S,i}^{SDC}$ are the charging, discharging, and self-discharging efficiencies, respectively.

Technical limits on power and energy further constrain the storage unit:

$$0 \leq P_{S,i}^{t,CH} \leq \overline{P}_{S,i}, \tag{9.7a}$$
$$0 \leq P_{S,i}^{t,DC} \leq \overline{P}_{S,i}, \tag{9.7b}$$
$$0 \leq Q_{S,i}^{t} \leq \overline{Q}_{S,i}, \tag{9.7c}$$
$$0 \leq E_{S,i}^{t} \leq \overline{E}_{S,i}. \tag{9.7d}$$

To improve interoperability and for simplicity, we fix the initial and final energy states via boundary conditions $E_{S,i}^{0} = E_{IC}$ and $E_{S,i}^{t+1} = E_{BC}$, ensuring the

storage does not gain or lose energy over the horizon. If no storage is connected to a bus, all associated variables are set to zero.

The resulting optimization problem is the full multi-period AC-OPF with storage:

$$\begin{aligned} \min \quad & C \quad (9.1) \\ \text{s.t.} \quad & \text{Power flow equations} \quad (9.2), \\ & \text{Physical constraints} \quad (9.3), \\ & \text{Storage model} \quad (9.4) \text{ - } (9.7) \end{aligned} \tag{9.8}$$

As in the previous chapters, the problem is nonlinear and nonconvex due to the full AC formulation and time-coupling from the storage state.

Shapley Value as Utility Measure

To quantify the marginal utility of each storage, we apply the Shapley value from cooperative game theory. Unlike in earlier chapters (e.g., Chapter 7), where the Shapley value was used to allocate redispatch costs among TSOs, here we adapt it to measure benefit: the reduction in total system cost due to the inclusion of an individual storage unit.

The basis is a cooperative game in which each player $p \in \mathcal{P}$ corresponds to a storage unit $s_i, i \in \mathcal{S}$, a coalition $\Omega \subseteq \mathcal{P}$ represents the active storage units, and the value of a coalition $\Phi(\Omega)$ is given by the optimal cost of the multi-period AC-OPF.

The Shapley value for a storage unit p is defined as:

$$\Psi_p = \sum_{\Omega \subseteq \mathcal{P} \setminus \{p\}} \frac{|\Omega|!(|\mathcal{P}| - |\Omega| - 1)!}{|\mathcal{P}|!} \left[\Phi(\Omega \cup \{p\}) - \Phi(\Omega)\right]. \tag{9.9}$$

Since the benefits of storage manifest over time, we compute the marginal contribution of each storage unit at every time step $t \in \mathcal{T}$, apply the Shapley procedure

to each step individually, and then aggregate the results. Thus, we define the utility Ψ_{s_i} of the storage unit (player) $p = s_i$ as the average marginal contribution of that storage unit across all time steps, where the Shapley value at each t is applied to the cost function c^t. To reflect a benefit (rather than a (negative) cost reduction), the total value is negated:

$$\Psi^{\text{BESS}} s_i(c) = -\frac{1}{T} \sum_{t \in \mathcal{T}} \Psi^t_{s_i}(c^t). \tag{9.10}$$

Since each c^t contributes linearly to the total cost $c = \sum_{t \in \mathcal{T}} c^t$, the additivity axiom of the Shapley value (Lipovetsky 2020) implies that the sum over time is equivalent to applying the Shapley value once to the full multi-period cost function. Hence,

$$\Psi^{\text{BESS}} s_i(c) = -\frac{1}{T} \cdot \Psi_{s_i}(c) \tag{9.11}$$

represents the average contribution of BESS unit s_i to the overall cost reduction, normalized over the horizon $\mathcal{T}$.

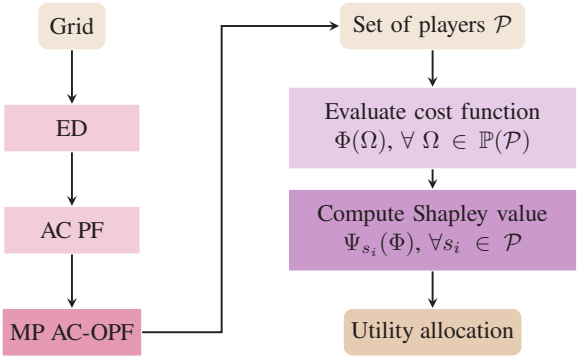

Figure 9.1: The Shapley algorithm for multi-period AC-OPF as a utility measure.

The algorithm is presented in Figure 9.1. Compared to before, the dark violet, purple, and brown boxes for the MP-AC-OPF, Shapley computation and utility allocation have changed.

The resulting value Ψ_p can be interpreted as a utility score: how much does the system benefit from the inclusion of storage unit p, relative to the case without it.

Baseline

To benchmark the utility values computed via the Shapley procedure, we define a baseline measure for each storage unit $s_i \in \mathcal{S}$ based on its total energy output. Specifically, we sum the active power discharged over the entire horizon $\mathcal{T}$:

$$B_i = \sum_{t \in \mathcal{T}} P_{S,i}^{t,DC}, \tag{9.12}$$

where $P_{S,i}^{t,DC}$ denotes the active power discharged by storage unit s_i at time t. This is a valid and symmetric reference, as the energy level is assumed to return to its initial state by the end of the horizon, the total amount of discharged energy is equal to the total amount charged, i.e.,

$$\sum_{t=1}^{\mathcal{T}} (P_{S,i}^{t,DC} + P_{S,i}^{t,SDC}) = \sum_{t=1}^{\mathcal{T}} P_{S,i}^{t,CH}. \tag{9.13}$$

Synthetic Load and RES Generation Data

For load and renewable generation profiles, we generate synthetic time series that are designed to mimic the periodic patterns that typically appear in daily demand and solar or wind generation.

The load profile for bus i is generated using a simple sine-based function creating a bump in the middle:

$$f_{\text{load},i}(t) = \left| d_i^{\text{load}} \cdot \frac{1}{2} \cdot \gamma^{\text{load}} \cdot \sin\left(\frac{\pi t}{T}\right) \right| \in \mathbb{R}^{\geq 0},$$

where d_i^{load} is the initial nominal load, and $\gamma^{\text{load}} \in \mathbb{R}$ is a scaling factor to control the amplitude. The absolute value ensures non-negative demand values.

The renewable generation profile (treated as negative load) is defined analogously, using a combination of sine waves to introduce more variability:

$$f_{\text{RES},i}(t) = -\left| \frac{d_i^{\text{RES}} \cdot \gamma^{\text{RES}}}{2} \cdot \left(\sin\left(\frac{4\pi t}{T} + 0.7\right) + \sin\left(\frac{3\pi t}{T}\right)\right)\right| \in \mathbb{R}^{\leq 0},$$

where d_i^{RES} is the nominal RES generation at bus i, and $\gamma^{\text{RES}} \in \mathbb{R}$ is a scaling factor. The negative sign reflects that the load is negative, and as loads are, per se, negative, it is a positive generation. As the RES curve is deterministic, i.e., contains no uncertainty, the assumption is a perfect forecast.

Results

Radial Five-Node Test Grid

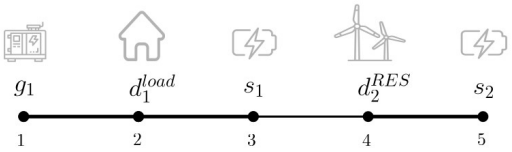

Figure 9.2: Grid topology and bus types for IEEE case5.

The five-node test grid (Figure 9.2) consists of a radial configuration with one generator at bus 1, followed by a load, a BESS unit s_3, a renewable generator (RES), and a second BESS s_5. Line capacities are 100 MVA, except the line between buses 2 and 3, which is reduced to 40 MVA to induce congestion. Loads are fixed to 40 MW/20 MVAr, RES generation is set to an initial 30 MW/10 MVAr (before curtailment). The generator has a cost of €40/MWh, and curtailment is

penalized at €60/MWh. The BESS units have energy/power ratings of 20/10 MW (s_3) and 10/10 MW (s_5), with a shared reactive power limit of [–50, 70] MVAr and round-trip efficiency of 0.9.

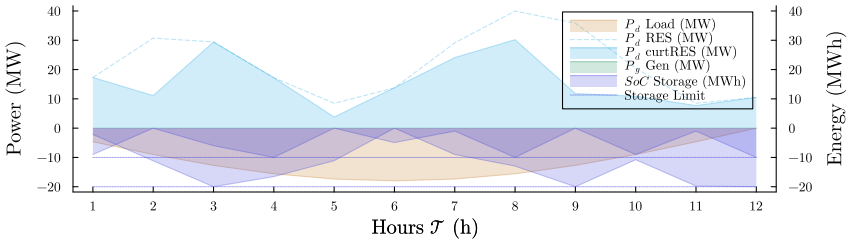

Figure 9.3: OPF results for the grand coalition $\Omega = 3, 5$ in IEEE case5.

Figure 9.3 shows the OPF results when both storage units are active. The RES generation fully covers the load, and excess energy is stored to avoid curtailment. No conventional generation is needed. Both storage units charge and discharge repeatedly, with unit s_3 (lower purple line) storing more energy due to its larger capacity and more central position.

Table 9.1: Costs of coalitions for case5.

Coalition Ω	$\{\}$	$\{3\}$	$\{5\}$	$\{3, 5\}$
Cost c (€)	87.8	55.8	66.2	44.0

Table 9.1 summarizes the resulting costs. With no BESS, the total cost is €87.8. Adding s_3 or s_5 alone reduces costs to €55.8 and €66.2, respectively, while the grand coalition yields the lowest cost at €44.0. The combined effect results in a 49.8% cost reduction. This indicates that s_3 is slightly more effective overall.

Figure 9.4 gives the results. Again, note that the Shapley values are positive (a negated cost reduction). The Shapley values in Figure 9.4a confirm the relative importance of the two BESS units. Storage s_3 receives a utility of 2.26, while

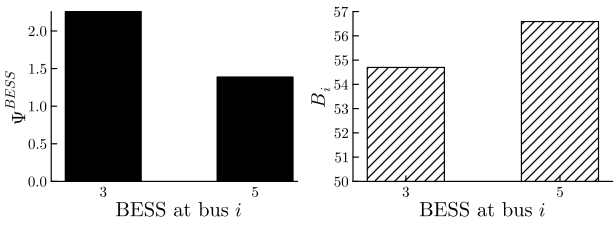

(a) Shapley values. **(b)** Baseline active power injections.

Figure 9.4: Shapley values and baseline injections for s_3 and s_5 in IEEE case5.

s_5 receives 1.39. This reflects its larger capacity and more central grid location. Interestingly, the baseline from Equation 9.12 in Figure 9.4b shows that s_5 injects slightly more (56.6 MW) than s_3 (54.8 MW). Hence, s_3 must offer additional value beyond energy shifting.

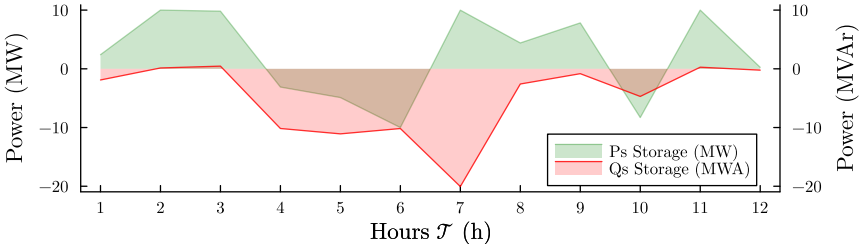

(a) Storage s_3.

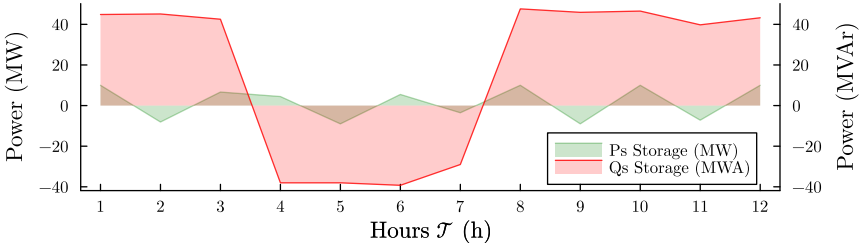

(b) Storage s_5.

Figure 9.5: Active (green) and reactive (red) power of BESS units in IEEE case5.

Figure 9.5 reveals that s_5 provides significantly more reactive power compensation than s_3. While s_3 operates mostly within [–20, 0] MVAr, s_5 ranges from –40 to +45 MVAr. This reactive contribution, which affects voltage and losses, is, however, hardly captured in the Shapley utility. The question remains whether the Shapley value can capture that reactive power compensation.

Modified IEEE case14

A more complex example is the IEEE case14, which has more nodes and is a meshed grid; see Figure 9.6. The loads and RES are concentrated in order to make the power flows more understandable and to imitate real-world situations. The most important parameters different to IEEE case5 are: The loads d_2, d_3, d_4, d_{13} are set to 45 MW/14 MVA, 30 MW/10 MVA, 70 MW/25 MVA, and 13 MW/6 MVA, respectively, and RES $d_{12}^{RES}, d_{14}^{RES}$ to 30 MW/10 MVA and 20 MW/7 MVA, respectively. Generation costs are €20, €30, €35, €40, and €50 for plants $g_{10}, g_1, g_2, g_8, g_6$, respectively. Branches $(4, 9), (5, 6), (6, 12), (7, 8), (12, 13)$ have a reduced capacity of 30 MVA, and all BESS units have 10 MWh of energy capacity.

The OPF results of IEEE case14 are given in Figure 9.7. We can see that the RES generation is insufficient to cover the load, and conventional generation fills in. Several storage units are charged, discharged, and charged again during the second peak. Removing the BESS results in significantly higher conventional generation, while some curtailment still occurs during peak periods, likely due to the restricted line capacity from north to south.

Table 9.2: Costs of coalitions for case14.

Ω	$\{\}$	$\{6\}$	$\{7\}$	$\{12\}$	$\{6,7\}$	$\{6,12\}$	$\{7,12\}$	$\{6,7,12\}$
c (€)	81.8	68.0	69.4	63.8	63.2	51.2	51.7	48.9

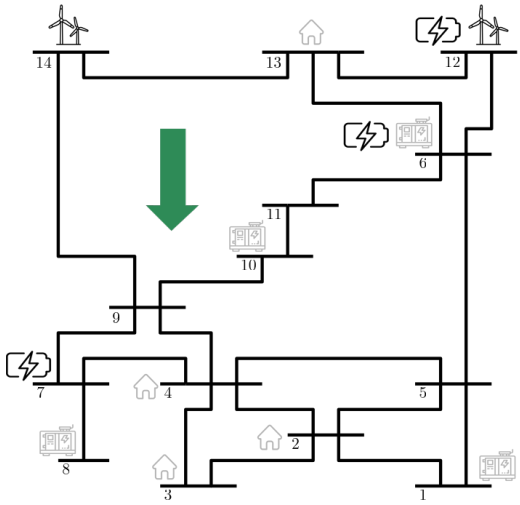

Figure 9.6: Scenario for IEEE case14.

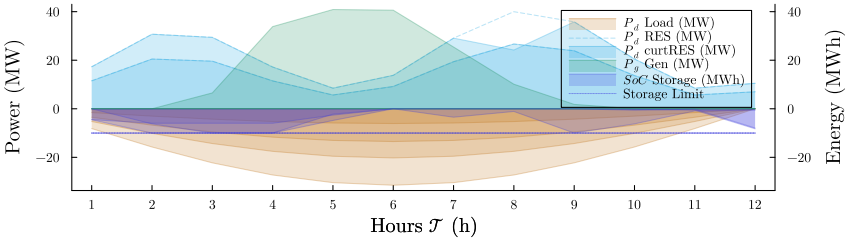

Figure 9.7: OPF results of case14 for the grand coalition $\Omega = \{6, 7, 12\}$.

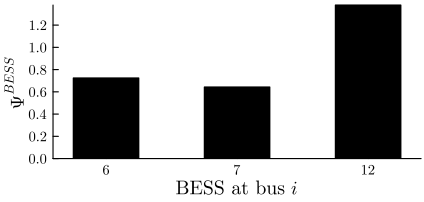

Figure 9.8: Shapley values for three storage units s_6, s_7, and s_{12} for case14.

Looking at the costs in Table 9.2, it seems that storage s_{12} contributes most to cost reduction, followed by s_6 and s_7. The overall cost reduction from €81.8 to €48.9 is approximately 40%, similar to the IEEE case5 scenario due to the chosen parameters.

The Shapley values in Figure 9.8 confirm this observation: Unit s_{12} has the largest contribution (1.38), followed by s_6 (0.72) and s_7 (0.64). In this example, the Shapley values roughly correspond to the sum of the active powers up to size. Still, the reactive power should be considered. Although the objective considers only active power generation costs, reactive injections influence voltages and losses, thereby altering the feasible dispatch set. This indirect effect is captured by the Shapley value, which explains why s_6 and s_7 receive non-negligible utility despite similar active power profiles.

Figure 9.9 shows that units s_6 and s_7 contribute significantly to reactive power compensation, with values up to ±70 MVAr. Although s_{12} shows lower reactive power usage, it has the highest utility. This suggests that active power affects cost reduction more directly, while reactive power contributions are still captured by the Shapley value due to their effect on system losses and voltage support.

Insights

Two insights stand out:

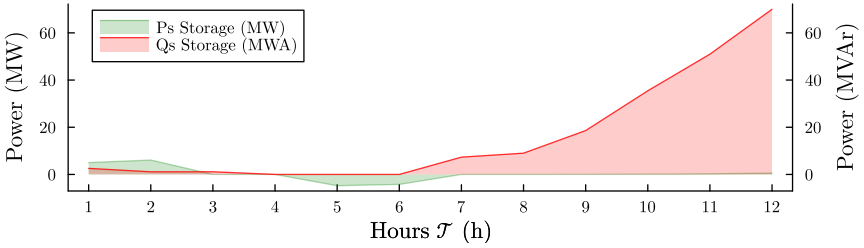

(a) Storage unit s_6.

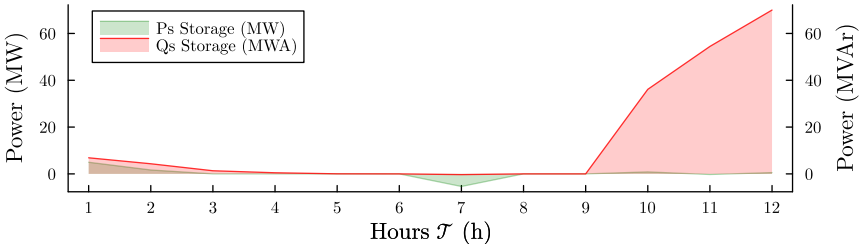

(b) Storage unit s_7.

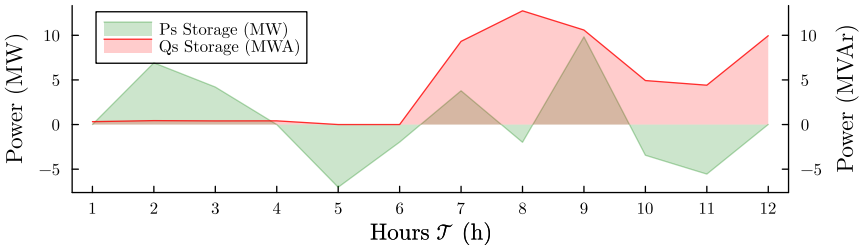

(c) Storage unit s_{12}.

Figure 9.9: Active (green) and reactive power input (red) of the BESS units of case14.

(1) The influence of an individual storage unit cannot be inferred from its active power profile alone. Location, losses, and voltage support can dominate the marginal contribution.

(2) The results hint that the Shapley value can capture reactive power effects even though the objective minimizes only active power cost, since reactive injections alter feasibility, losses, and dispatch.

These findings suggest that the Shapley value can enhance transparency by quantifying the broader system contribution of BESS units—including indirect effects that are otherwise difficult to observe.

9.2 Discussion and Conclusion

This chapter presented a Shapley-based utility measure to quantify the contribution of battery energy storage systems (BESS) in the transmission grid. Based on a multi-period optimal power flow (MP-OPF), the approach allocates system cost reductions to individual storage units while respecting time coupling, nonlinear interactions, and both active and reactive power effects. The approach is demonstrated on two test systems: a simplified 5-bus radial grid and a modified IEEE 14-bus meshed grid.

The results show that the Shapley value offers a meaningful and interpretable measure of system utility. It captures contributions that are not directly observable in the power injections alone due to the meshed nature of the power grid. Units with comparable energy throughput can yield substantially different values, depending on their location and system interaction. This supports the idea that BESS placement decisions should not rely solely on injection magnitudes or energy-based heuristics, but should instead involve a system-wide analysis.

Interpretation and Technical Considerations

Several modeling choices and observations deserve further clarification.

First, while the Shapley value can be evaluated per time step, this is not meaningful for storage. Due to intertemporal coupling, a storage unit's value often depends on its behavior over the whole horizon. Temporary charging or discharging may appear costly in isolation, but is beneficial when viewed in the broader context of future load or RES forecasts. Consequently, a storage unit may exhibit positive marginal costs in individual time steps, yet its overall Shapley value remains negative, reflecting net cost reduction over the full horizon.

Second, one might ask whether the presence of BESS can introduce new congestion. Since congestion is defined by comparing the optimal power flow (OPF) with a reference power flow (PF) that excludes storage, no new congestion can arise solely from storage. More precisely, a congestion is counted only if the OPF violates a limit that is also violated in the reference PF; limits that turn binding solely as a consequence of the storage's operation are not considered part of the congestion set. However, line loadings may increase, particularly near the storage units, as they actively participate in balancing power flows.

Third, it is theoretically possible for BESS to reduce costs below the reference PF solution, especially if large and well-located storage units reduce expensive generation. This would result in negative redispatch costs. However, such outcomes are rare in realistic scenarios, as transmission and storage limits constrain the extent to which storage can reshape flows or displace generation.

Limitations and Open Questions

The proposed method is not without limitations. The following aspects are particularly relevant for future research:

Time horizon What horizon length is required to obtain a stable and representative utility value, especially when decisions are made over shorter intervals?

There has been work on finding the optimal planning horizon in storage scheduling problems (Prat et al. 2024), showing that it is possible to determine a long-enough horizon. A research question could be whether the same holds for our BESS schedules in transmission grids.

Scalability Two questions arise when it comes to applying the approach on larger power grids: Does it work equally well on larger grids, and do the Shapley values show the same behavior? And does the approach scale well? Regarding the behavior, some effects might be smoothed out or enlarged, such as the sensitivity to perturbations. Regarding computation complexity, due to the factorial increase in coalitions, scalability is a challenge. However, there are approximation methods that have proven to work well in other contexts (van Campen et al. 2017) (Survey: (Lamothe and Ngueveu 2025)). The only question is, wether they work equally well on a complex system such as an AC power grid.

Model assumptions The analysis is performed with ideal model assumptions such as perfect (deterministic) forecasts and does not include any uncertainty, nor in the available load and RES data, nor in that BESS units are keeping some capacity for other services, nor in the variability of prices. In practice, a lot more criteria have to be considered that might make the Shapley computation for BESS units more difficult. What these are and how they can be considered is an open research question.

Sensitivity and robustness How stable is the Shapley value under variations in component parameters or other perturbations in the grid? This links to the last point of model assumptions and uncertainty. Since we considered only one load scenario, it would be interesting to see how meaningful the Shapley value of a component is in an ever-changing environment and over a longer period of time.

We do address the last point of uncertain component parameters and changing grid configurations in the next Chapter 10.

Conclusion and Outlook

The increasing complexity of power systems, driven by the integration of renewable energy and the decentralization of resources, demands tools that improve transparency and explainability. BESS are an important flexibility resource, but their system contribution is sometimes difficult to quantify. This chapter proposed a Shapley-based utility measure to evaluate the operational value of individual storage units in terms of system cost reduction.

The results demonstrate that this measure can distinguish between different units – even when they perform similarly in terms of injected energy – based on their location, interaction, and system impact. This enables more informed planning decisions regarding BESS deployment and supports the design of compensation or incentive schemes that reflect true system value.

Future work should further investigate the robustness of the utility metric under system changes, as well as explore its application to other outputs of the MP-OPF, such as reactive power or RES curtailment. In addition, the method could be extended to support optimal BESS placement or portfolio planning under uncertainty and operational constraints. The potential to generalize the Shapley value toward broader transparency metrics in grid planning and regulation presents an exciting direction for continued research.

10 Robustness Analysis of the Shapley Value in Power Grids

After having applied the Shapley value to battery storage units, showing differences in AC and DC OPF usage, and using it in a privacy-preserving fashion, another step towards practical applicability is necessary: Testing the values' robustness in the face of uncertainties in the grid.

This reminds us of the first part of this thesis, where we included uncertain wind generation in a DC OPF problem. In this second part, we do not include uncertainty analytically, but rather through different scenarios. We want to test how robust the Shapley value is when faced with an uncertain load situation and grid parameters. We also want to know, whether these changes affect various player types equally, e.g., storage units, but also generators or branches. This is summarized in the last research question of this thesis:

RQ6 *How robust is the Shapley value in its application to electricity grids in the face of perturbations in grid parameters?*

We can divide this question by asking what parameters we change: the ones of the player himself, or the grid parameters. In this chapter, we look at both aspects in two parts with the following questions:

(1) *How does the Shapley Value for BESS units change when their parameters are perturbed?*

(2) *How does the Shapley value of various player types change under perturbations in the grid parameters?*

To answer these questions, we perform an experimental robustness analysis using Monte Carlo sampling for one example grid.

A robustness analysis usually tests how stable a system is when its inputs are perturbed, or when ideal assumptions from theory no longer hold. Its goal is to ensure that the outcome is not highly sensitive to uncertain inputs and can function under various conditions. In contrast to a sensitivity analysis, it does not ask which input features have the most effect on the output, but tests extreme conditions.

In the context of electricity grids, a robustness analysis for tools that automate, help decision-making, or allocate costs is essential as grid systems are subject to constant changes. These include uncertainties in RES generation, transmission line failures, and changing loads. By better understanding the impact of these changes, we can make more informed decisions regarding resource allocation, grid investments, and the overall design of future grid infrastructure. When it comes to cost allocation mechanisms, e.g., for electricity charges or the evaluation of the beneficialness of components, it is especially vital to know how the value behaves. Only then can we interpret it properly and include it in our decision-making processes.

One primary requirement is that its behavior is predictable. It should reflect changes in the grid, but also stay fairly stable and not be overly sensitive to small changes. Of course, how the value behaves always depends on the dynamics of the underlying grid. Accumulating values, such as the Shapley value that averages marginal contributions, usually have such a behavior. As the Shapley value is a linear map, its output also changes linearly with the inputs. Still, different values behave differently, and we do not know precisely how, especially for complex systems like electricity grids. Therefore, it is necessary to perform a robustness analysis before thinking about deploying it in practice.

The remaining chapter first describes the experimental setup including sampling strategies, data, and perturbations, then gives the results for questions (1) and (2), and concludes with a discussion.

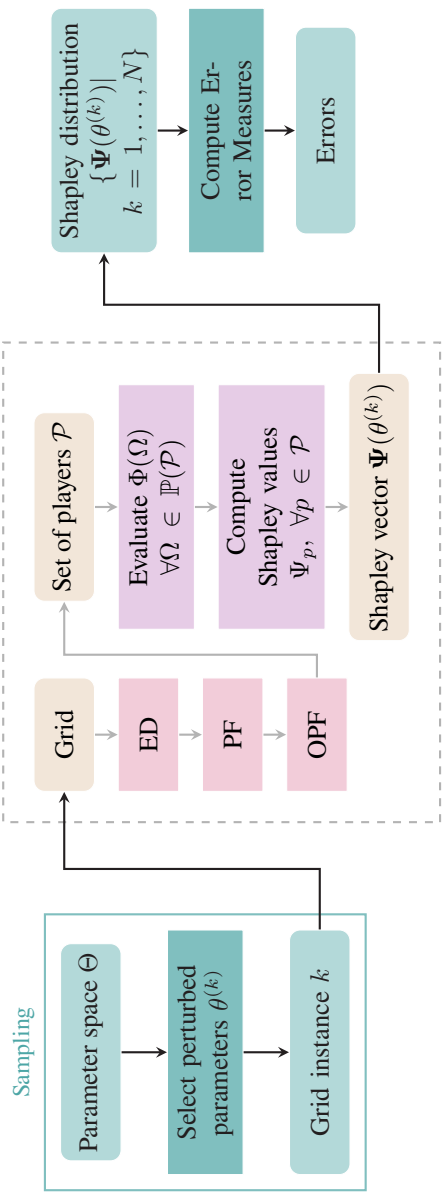

Figure 10.1: Integration of Monte Carlo sampling with the Shapley value computation. Perturbed grid parameters are sampled from the parameter space and passed through the original Shapley pipeline (shown in the dashed box). The resulting Shapley vectors are aggregated and analyzed using cosine similarity, MAE, and rank-order error.

10.1 Experimental Setup

This robustness analysis (def. in Nosek and Errington (2020)) is empirical and conducted on a modified IEEE 14-bus test grid, described below. The goal of this first attempt is to study how the Shapley value behaves under large controlled changes of the grid topology in a meshed network.

The workflow of the analysis is shown in Figure 10.1. Perturbed grid scenarios are sampled on the left, passed through the unchanged OPF–Shapley pipeline (dashed box), and yield Shapley vectors $\Psi(\theta^{(k)})$ for each realization. These vectors are then evaluated using the robustness metrics shown on the right.

Sampling Strategies

We use two sampling strategies to generate perturbed grid scenarios: a grid sweep and Monte Carlo sampling. For Question (1), BESS parameters are varied directly via a deterministic grid, since we directly evaluate the storage units. For Question (2), Monte Carlo sampling is used to integrate the more complex grid–component interactions. All scenarios are evaluated with both the DC and AC OPF formulations.

Deterministic Grid Sampling

For Question (1), each storage parameter (location, efficiency, energy capacity, and charge/discharge limits) is systematically varied over a predefined grid. Only one parameter is perturbed at a time, while all others remain at their default values. This produces a deterministic and structured set of scenarios that covers the full parameter range without randomness.

Monte Carlo Sampling

For Question (2), we use Monte Carlo sampling to capture the complex grid interactions; grid sweep would not be possible due to the many possibilities. In each trial, several component types (generator, load, branch, or RES unit) with one or two associated parameters are selected and perturbed. The magnitude of the perturbation is drawn from the corresponding intervals. Each draw yields one random grid realization. The following subsection formalizes this sampling process with Monte Carlo sampling.

Mathematical Formulation To describe the sampling process mathematically, we collect all perturbed grid parameters in a vector

$$\theta = [\theta_1, \ldots, \theta_m]$$

with each parameter θ_j drawing values from the domain Θ_j, i.e., $\theta_j \in \Theta_j$. The whole value space is then defined as $\Theta = \Theta_1 \times \cdots \times \Theta_m$, from which we draw N independent samples from a probability distribution $P(\Theta)$:

$$\theta^{(k)} \sim P(\Theta). \qquad k = 1, \ldots, N$$

Each sample $\theta^{(k)}$ represents a scenario of the TU game $(\mathcal{P}, \Phi(\cdot \mid \theta^{(k)}))$, with players $\mathcal{P}$, OPF cost function Φ, and grid parameters $\theta^{(k)}$. Let $\Psi_p(\theta^{(k)})$ denote the Shapley value of player $p \in \mathcal{P}$ in scenario k. Then the set

$$\left\{ \Psi_p(\theta^{(k)}) \mid k = 1, \ldots, N \right\}$$

gives the empirical distribution of one player's Shapley value allocation under uncertainty.

Robustness can then be assessed with several measures. Closest are the empirical mean and variance that can be applied to the distribution of one or all players' Shapley values. The empirical mean of player p is defined as

$$\widehat{\mu}_p = \frac{1}{N} \sum_{k=1}^{N} \Psi_p(\theta^{(k)}). \tag{10.1}$$

The empirical variance, capturing the spread of player p's Shapley values across all perturbations, is

$$\widehat{\sigma}_p^2 = \frac{1}{N} \sum_{k=1}^{N} \Big(\Psi_p(\theta^{(k)}) - \widehat{\mu}_p \Big)^2. \tag{10.2}$$

Since mean and variance only give limited information, we use three additional error measures: *cosine similarity*, the *mean absolute error (MAE)*, and a *rank-order error*. Each measure captures a different dimension of robustness: cosine similarity captures the overall alignment or correlation between Shapley vectors, MAE captures the absolute magnitude of deviations, and rank-order error captures how strongly the relative importance of players, as expressed through their Shapley values, has shifted. They are defined as follows.

Definition 6 (Cosine Similarity) *Let $\mathbf{\Psi}^{(a)}$ and $\mathbf{\Psi}^{(b)}$ denote two Shapley value vectors. The (normalized) cosine similarity is defined as*

$$\mathrm{CosSim}\left(\mathbf{\Psi}^{(a)}, \mathbf{\Psi}^{(b)}\right) = \frac{\mathbf{\Psi}^{(a)} \cdot \mathbf{\Psi}^{(b)}}{\|\mathbf{\Psi}^{(a)}\|_2, \|\mathbf{\Psi}^{(b)}\|_2}, \tag{10.3}$$

normalized to lie in $[0, 1]$. It measures the directional correlation between the two vectors.

While cosine similarity reflects the general alignment, it does not reflect whether the order, which indicates the player's importance, changes. Knowing this is

important when decisions are to be made, e.g., which component is built. To assess the order, we take the rank-order error, defined as follows.

Definition 7 (Rank-Order Error) *Let* $\mathrm{rank}(\boldsymbol{\Psi})$ *denote the ordering of players induced by the Shapley values. The rank-order error between two Shapley value vectors is defined as the number of pairwise inversions between their rankings. This quantity is not normalized. It measures how much the relative importance of players changes.*

However, even if the order is off, it might still be the case that the differences are generally very small. Therefore, we have to consider the absolute deviations as well with the mean absolute error, defined as follows.

Definition 8 (Mean Absolute Error (MAE)) *For two Shapley value vectors* $\boldsymbol{\Psi}^{(a)}$ *and* $\boldsymbol{\Psi}^{(b)}$*, the globally normalized mean absolute error is*

$$\mathrm{MAE}\left(\boldsymbol{\Psi}^{(a)}, \boldsymbol{\Psi}^{(b)}\right) = \frac{1}{|\mathcal{P}|} \sum_{p \in \mathcal{P}} \left| \Psi_p^{(a)} - \Psi_p^{(b)} \right|. \tag{10.4}$$

It describes the absolute deviations between both allocations.

Together, these three measures provide an interpretable assessment of how the Shapley values change.

Data

We perform both robustness analyses on a modified IEEE 14-bus test case. The load, generation, and line limits are adjusted to obtain a north-south power flow with congestion, and storage units are added. The grid is visualized in Figure 10.2, which stems from the previous chapter. All modifications are listed in Table 10.1; while the storage parameters are given in Table 10.2.

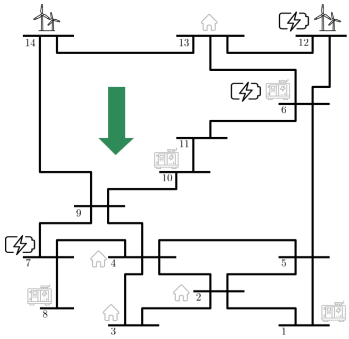

Figure 10.2: Scenario for IEEE case14.

Perturbation Intervals

The pipeline in Figure 10.1 applies to both Question (1) and Question (2); only the perturbed parameter sets differ between them. Tables 10.3 and 10.4 summarize all grid values and intervals used.

For Question (1), we analyze how changes in the storage unit's own parameters affect its Shapley value. For this, we add three storage units at buses $\mathcal{S} = \{6, 7, 12\}$ with energy capacity 10 MWh, power limits of 10 MW, and efficiencies of 0.9. In each trial, we alter the capacity and power, the efficiencies, add or remove a storage unit, or scale the RES output with the factor a_{RES}. In total, we test $N = 57$ scenarios, containing 7 values for the capacity, 5 for the efficiencies, 10 for the amplitude factor a_{RES}, and 35 different storage locations for 2 and 3 storage units.

For Question (2), we study how Shapley values of different player types behave when the grid topology or composition changes. In each Monte Carlo trial, we add either a generator, a load, a branch, or a RES unit at a randomly selected admissible location, or scale the RES output. For this part, we have many more scenarios than in the first, because the relationship between the perturbation and the tested component is more complex due to interactions with the grid. In total, we have $N = 133$ scenarios, with 34 for the generators, 42 for the branches, and

Table 10.1: Modifications of IEEE case14 for the robustness analysis.

Component	Parameter	Changes
Branch $l \in \mathcal{L}$	RateA[1] $\overline{S}_{ij}$	30 for $l \in \{9, 10, 12, 14\}$, 10 for $l = 19$
Generators $i \in \mathcal{G}$	Location	move g_3 to g_{10}, add g_1, g_2, g_6, g_8
	Cost coeff. b_i	$b_1 = 0.3, b_2 = 0.35, b_6 = 0.5, b_8 = 0.4, b_{10} = 0.2$
	$\overline{P}_{G,i}$	$190.0\ \forall i \in \{1, 2, 6, 8, 10\}$
	$\overline{Q}_{G,i}$	$130.0\ \forall i \in \{1, 2, 6, 8, 10\}$
Loads $i \in \mathcal{D}$	Location	delete $d_6, d_9, d_{10}, d_{11}, d_{12}, d_{14}$
		move d_5 to d_3
	$P_{D,i}$	$\{45, 30, 70\}\ \forall i \in \{2, 3, 4\}$
	$Q_{D,i}$	$\{15, 10, 25\}\ \forall i \in \{2, 3, 4\}$
RES $i \in \mathcal{D}^{\text{RES}}$	Location	add $d_{12}^{RES}, d_{14}^{RES}$
	$P_{D,i}^{RES}$	$\{30, 20\}\ \forall i \in \{12, 14\}$
	$Q_{D,i}^{RES}$	$\{10, 7\}\ \forall i \in \{12, 14\}$

Table 10.2: Storage parameters for the modified IEEE 14-bus system.

Component	Parameter	Value
Storage $i \in \mathcal{S}$	Location	s_6, s_7, s_{12}
	Capacity $\overline{E}_{S,i}$	10 MWh
	Efficiencies $\eta_{S,i}^{CH}, \eta_{S,i}^{DC}, \eta_{S,i}^{SDC}$	0.9

57 for the storage units from before. The players are $\mathcal{P}_{\mathcal{S}} = \{6, 7, 12\}$ as storage units, $\mathcal{P}_{\mathcal{G}} = \{1, 6, 8\}$ as generators, and $\mathcal{P}_{\mathcal{L}} = \{1, 7, 10, 19\}$ as branches.

Table 10.3: Parameter grids used in Part (1), where only storage units and RES amplitude are perturbed. All parameters are varied deterministically over predefined grids.

Component	Parameter	Grid
Storage	Capacity / Power	$\{10, 20, \ldots, 70\}$ MWh/MW
	Self-/Dis-/Charge efficiency	$\{0.8, 0.85, \ldots, 1.0\}$
	Location	$\mathcal{N}$
RES units	Amplitude a_{RES}	$\times\{0.25, 0.5, \ldots, 2.5\}$

Table 10.4: Parameter intervals used in Part (2), where grid-level components are perturbed using Monte Carlo sampling. In each trial, exactly one component type and one parameter is perturbed.

Component	Parameter	Interval / Set
Storage	Location	$\mathcal{N}$
Generators	Location	$\mathcal{N} \setminus \mathcal{G}$
Loads	Location	$\mathcal{N} \setminus \mathcal{D}$
Branches	Location (new)	$\mathcal{N}$
RES units	Amplitude a_{RES}	$\times[0.25,\ 2.5]$

10.2 Results

The results follow the two questions (1) and (2) from above; by (1) analyzing perturbations of BESS parameters onto BESS Shapley values—also comparing values based on AC and DC-OPF as previously for congested lines, and (2) analyses the influence of random perturbations in the grid onto the Shapley values of storage, generators, and branches.

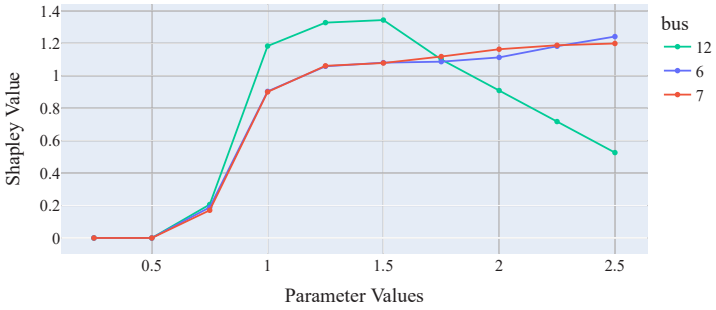

Figure 10.3: Shapley values of storage units at buses 6, 7, and 12 under perturbed RES amplitude factors.

BESS Parameter Perturbations

This first section addresses the first part of research question **RQ6**:

How does the Shapley Value for BESS units change when their parameters are perturbed?

In the following, we look at all parameter types individually and assess their impact on the Shapley values of the storage units.

RES Amplitude As the amount of RES generation increases, see Figure 10.3, the Shapley values rise sharply once RES production is large enough to saturate local demand. When RES output is very low, all storage units contribute almost nothing—the OPF hardly uses storage because there is simply no surplus to shift across time. As RES output grows, the unit located closest to the RES buses gains the most value. But this trend reverses at very high amplitudes: when RES generation becomes so large that it directly displaces conventional generation at the same point in time, storage becomes less relevant, and its marginal contribution declines. Thus, while placing storage close to RES generation is generally advantageous, the overall benefit still depends on how the units interact with the rest of the system.

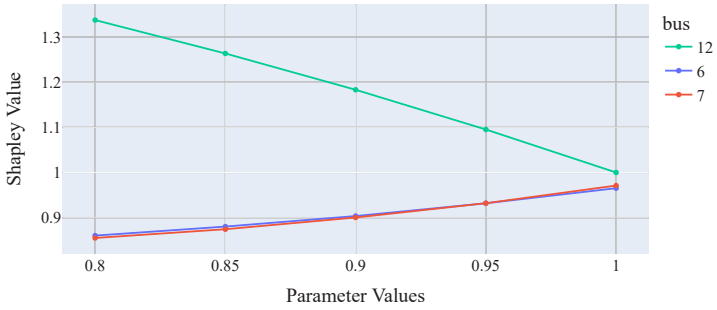

Figure 10.4: Shapley values of storage units at buses 6, 7, and 12 under perturbed efficiencies.

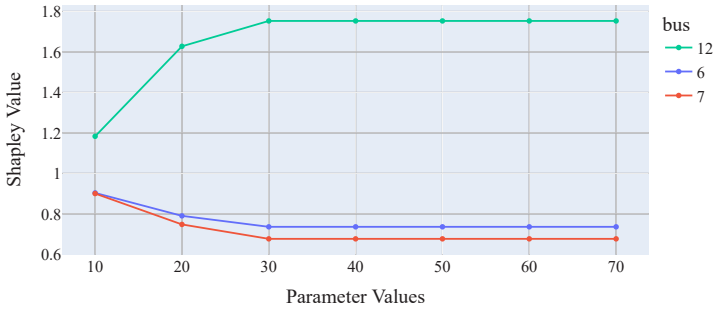

Figure 10.5: Shapley values of storage units at buses 6, 7, and 12 under perturbed capacities.

Efficiency Raising the efficiency parameters increases the value of all units, but not uniformly, see Figure 10.4. The farther a unit sits from the RES injections, the more it benefits from increased efficiency—because higher round-trip efficiency compensates for additional network losses and congested paths, making these units more attractive for the OPF. Although the Shapley values of the units move noticeably with the efficiency parameters, the trajectories remain smooth and monotonic. The changes are predictable rather than erratic. Overall, storage units do not converge to identical values—even with perfect efficiency—because network placement still governs their system value.

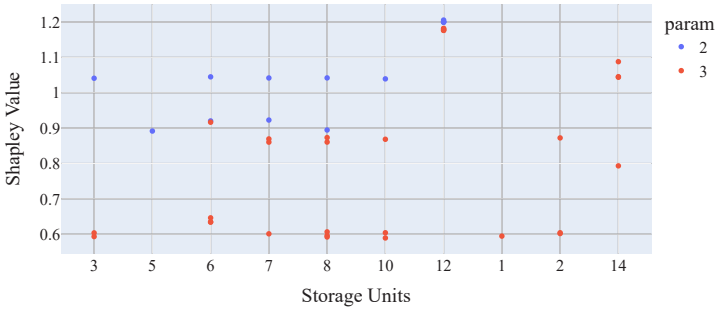

Figure 10.6: Shapley values of storage units at buses 6, 7, and 12 under varying numbers of storage units and locations.

Capacity Larger energy capacity clearly increases the value of the unit nearest the RES, see Figure 10.5. That unit captures the bulk of additional cost savings because it can absorb most of the fluctuating RES surplus directly at the source. As soon as the storage becomes large enough—that is, it can absorb all RES generation—the value saturates. Among all parameters tested, capacity produces the largest spreads in the Shapley values (up to 1.8), exceeding efficiency and RES amplitude changes.

Location Placement matters, but only up to a point, as shown in Figure 10.6. With two units, each storage sees a higher individual value because they are used more intensively. With three units, all but the RES-adjacent locations drop to low, nearly flat values around 0.6. Only units very close to RES consistently retain high value; units elsewhere are used fairly evenly and contribute comparatively little. Once several units are active, marginal contributions flatten across most locations—the network distributes usage broadly, except at the RES injection points.

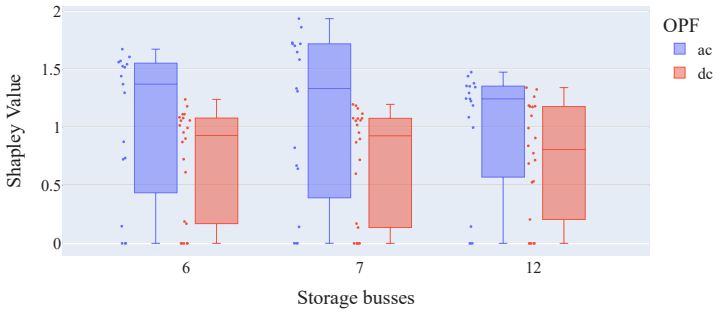

Figure 10.7: Distribution of Shapley values for storage units at buses 6, 7, and 12 under RES-amplitude perturbations.

Differences in AC vs. DC

One aspect that arose before in Chapter 8 was that AC and DC-OPF yield different congested lines and different Shapley values with sometimes unexpected outcomes. Therefore, given our many results, we split the values in those runs performed with a DC-OPF, and those with an AC-OPF, and check how much they differ. This is interesting as Shapley values might have a different sensitivity for storage units than for branches (congested lines).

To avoid redundancy, we only show those results for the factor with which the RES amplitude is multiplied, and for the number of storage units at different locations. The results for perturbations in capacity and efficiency are given in the Appendix (see Section A.4). Up front, we can already say that AC and DC OPF yield fairly similar results with slightly higher values for AC. This meets expectations, as AC produces higher costs due to added losses. It also suggests that the DC-OPF might just be good enough for approximating the Shapley values of BESS units.

Figure 10.7 shows the distribution of Shapley values under varying RES amplitudes, separated into AC and DC OPF. Since the storage units are grouped by bus, the plot highlights how each unit responds to changes in renewable injections. Across all three buses, AC-based Shapley values are generally higher and show a

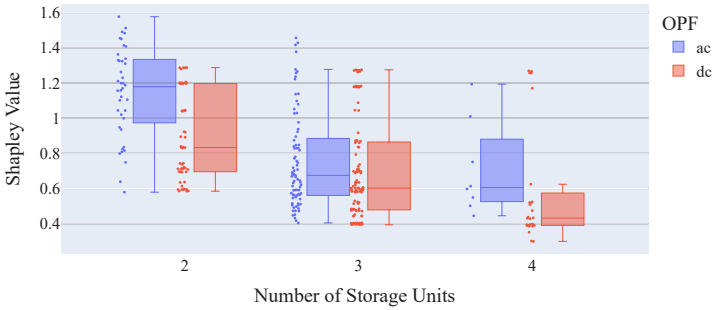

Figure 10.8: Distribution of Shapley values for two, three, and four storage units placed randomly in the grid. All their Shapley values are depicted in one of the three groups on the x-axis, which indicates the number of storage units placed.

noticeably larger spread. This can be interpreted such that storage units are more sensitive to changes in the AC setting, or that the perturbations in the AC setting produce more complex interactions between RES generation and the grid. This also means, that storage becomes more valuable in the AC setting because it can relieve not only active-power congestion but also AC-specific constraints.

Figure 10.8 shows the distribution of Shapley values under varying numbers of storage units and, hence, slightly different locations, too. As before, fewer storage units tend to have higher marginal contributions, with two having noticeably larger values than three or four units, suggesting that they have the biggest payoff and that more units might not be necessary. Comparing AC and DC, both formulations exhibit almost the same ordering across the cases, and the absolute differences are small. As this shows in the other plots, too, it supports the argument that DC might be good enough for BESS units. Nevertheless, AC values are slightly higher across the board, but not as pronounced as in the RES amplitude experiment. This makes sense, since when adjusting only the number and locations of storage units—without altering the injection height—the system is not driven into strongly voltage-sensitive regions. Additionally, the variance is still high, suggesting that at some locations, storage is very useful, while at others not so much. This also shows that placement within the grid matters.

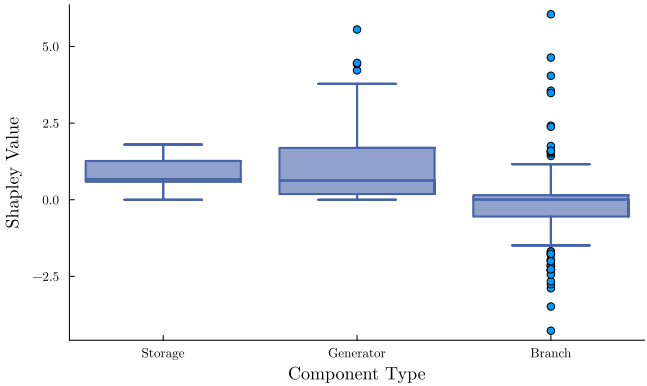

Figure 10.9: Mean and variance of all trials for perturbations through added generator, storage, and branch components.

Perturbations in other components

This second section addresses the second part of research question **RQ6**:

How does the Shapley value of various player types change under perturbations in the grid parameters?

Note: When there are more units in the plots than stated players, this happens because, as a perturbation, one unit of the player's type can be added.

Figure 10.9 presents a box plot of Shapley values across all individual components, grouped by type—storage units, generators, and branches. Generators generally show the highest median Shapley values and a wide range, indicating that they often exert a strong influence on the system outcome but with notable variability across units. Storage units also have positive Shapley values with tighter spreads, suggesting that their contribution is consistently beneficial and less sensitive to system configuration. Branches, in contrast, cluster around zero with a high number of outliers in both directions, reflecting that it very much depends on the setting whether the branch benefits the system, but it can also be counterproductive,

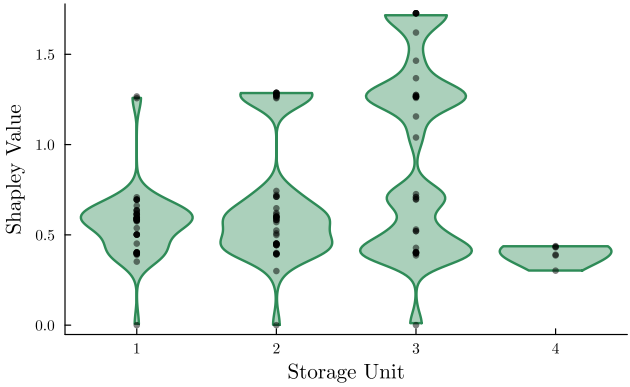

Figure 10.10: Distribution of Shapley values per storage unit over all trials. Units $\{1, 2, 3\}$ are located at buses $\{6, 7, 12\}$. The additional unit 4 can be located anywhere in the grid.

too. One could say that adding branches to a network needs to be planned a lot more carefully than adding generators or storage units.

However, as this graphic only shows aggregated values, we need to look at the players individually and apply more elaborate error scores than mean and variance.

In the following graphics, each trial is represented by a black dot. Red dashed line represents no correlation of the Shapley vectors for Cosine Similarity, and one permuted order for the Rank-Order Error (based on MSE). The Mean Squared Error (MAE) is normalized globally over all trials.

Storage

Figure 10.10 shows the full distribution of Shapley values for individual storage units at buses $\{6, 7, 12\}$. Units one and two display relatively narrow and centered distributions, which points to stable and consistent importance across different trials. However, some units, such as unit 3, show a broader or multi-modal

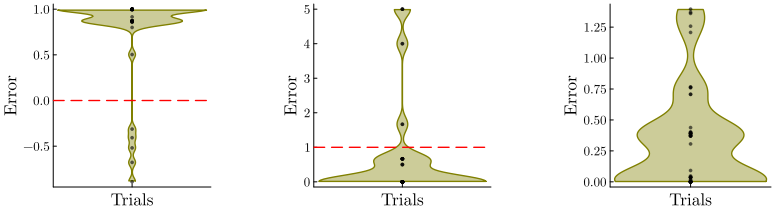

(a) Cosine Similarity. **(b)** Rank-Order Error. **(c)** MAE.

Figure 10.11: Error measures assess the sensitivity of the Shapley value to perturbations with respect to storage units as players.

distribution, suggesting their influence fluctuates significantly depending on the specific network configuration or parameter set. The fourth violin is small as only in some trials storage units have been added.

Figure 10.11 shows the three error measures applied to the whole set of Shapley vectors over all players. The cosine similarity and rank-order error show strong stability, indicating that storage-related Shapley rankings are preserved under parameter variations. However, the MAE is slightly more dispersed, varying on average about 50%. Since values are not large in general (see Figure 10.10) and the other two measures show high agreeableness, all values must have increased about the same size. This can match with the results from the previous section. Hence, while storage units tend to retain their relative importance, the magnitude of their Shapley values is sensitive to perturbations, probably mostly changes in RES generation.

Generator

Figure 10.12 illustrates the Shapley value distributions for each generator at buses $\{1, 6, 8\}$. One generator (unit 1) stands out with both the highest mean and variance, suggesting it plays a dominant and context-sensitive role in system

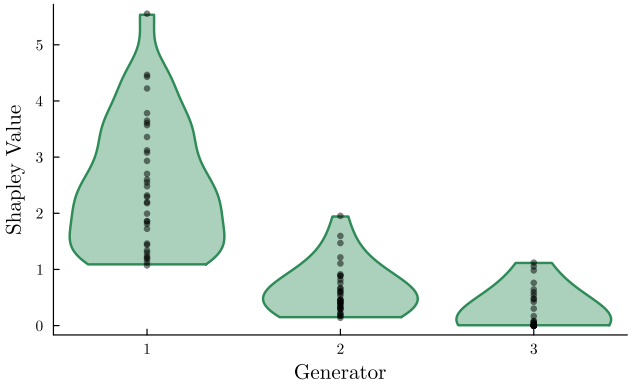

Figure 10.12: Distribution of Shapley values per generator over all trials.

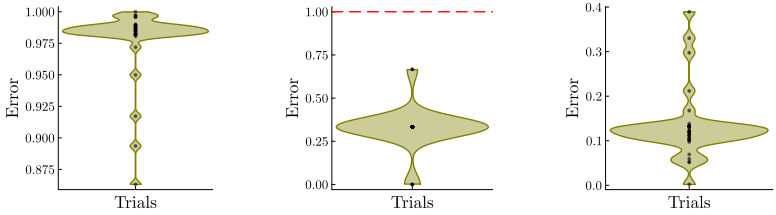

(a) Cosine Similarity. **(b)** Rank-Order Error. **(c)** MAE.

Figure 10.13: Error measures assess the sensitivity of the Shapley value to perturbations with respect to generators as players.

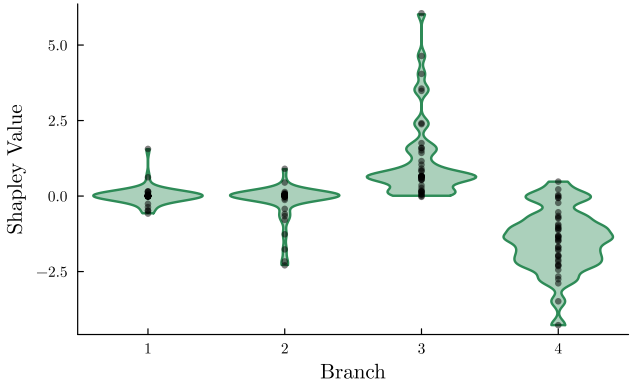

Figure 10.14: Distribution of Shapley values per branch over all trials.

outcomes. This is well reasoned with it being the cheapest generator and with 1 and 8 being closer to loads than the generator at bus 6.

Figure 10.13 presents sensitivity metrics for the Shapley values resulting from perturbations of generator parameters. The cosine similarity remains high across trials, indicating that the direction of the influence vector is well preserved. The rank-order error is also low, confirming that the relative importance of generators is robust to parameter changes. The MAE shows broader variability, implying that while the ranking of players remains consistent, their absolute contributions do shift, although all in a similar direction. This suggests that the Shapley value for generators is stable in terms of order, but not necessarily in magnitude.

Branch

Figure 10.14 displays the distribution of Shapley values for each branch in $\{1, 7, 10, 19\}$. As expected from the component-level analysis, most branches

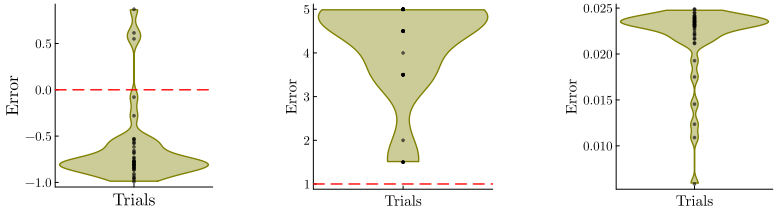

(a) Cosine Similarity. **(b)** Rank-Order Error. **(c)** MAE.

Figure 10.15: Error measures assess the sensitivity of the Shapley value to perturbations with respect to branches as players.

cluster around a zero Shapley value, reflecting their generally low impact. However, several branches show highly dispersed distributions, showing that in some grid configurations, they can exert considerable influence. As such, they are more critical to plan a storage unit.

Figure 10.15 shows how sensitive the Shapley values are to perturbations in the branch parameters. The cosine similarity values are surprisingly close to -1, indicating a strong counter-correlation. This means the Shapley vectors are pointing in opposite directions. The rank-order error also yields uncorrelated values; the order of the values is completely off. However, looking at the MAE, the absolute values are small in general, so the results from the other two error measures cannot be taken as very important, as small grid changes quickly alter these scores.

10.3 Discussion & Conclusion

This chapter examined the robustness of the Shapley value when grid parameters or player attributes are perturbed. We tested a range of scenarios to understand how much the value shifts under changing system conditions. Results show that the Shapley value generally behaves in a stable and interpretable manner, but the

degree of robustness depends strongly on the type of component and the form of perturbation.

The Shapley value behaves as expected continuously with respect to parameter changes, especially in the deterministic grid tests for BESS units. Increasing their efficiency or capacity raised the Shapley value, particularly for units near renewable injections. For the capacity and number of storage units there are saturation effects, and good efficiencies spread the utility more evenly across units. However, there is also the unexpected effect of lower use with very high RES shares of the unit close to RES generation. Hence, the utility increases mostly as expected and can be approximated with active power injections, although there might be potential in using the Shapley value in a planning simulation to bring additional insight into each unit's beneficialness. Also, there are slight differences between optimization with AC and DC OPF; Shapley values based on AC OPF yield slightly higher values with a slightly larger spread. This can mean that they are more sensitive to grid changes and can better help with the nonlinear constraints in an AC setting.

In the Monte Carlo simulations for system-wide perturbations, generators showed the highest and most consistent Shapley values. This makes sense, as the system costs are the generation costs. Storage units followed, with slightly lower values but good robustness. Branches had low mean values but wide variance, indicating high sensitivity to location. Error metrics like cosine similarity and rank-order error confirmed these patterns. The shape of Shapley vectors was preserved well across trials, but rankings—especially for branches—were unstable. This implies that absolute contributions are fairly robust, but relative importance is less obvious for branches. Hence, when planning a grid, branches are the more delicate component, while generators and storage units are less sensitive to their location and other added components.

Limitations

As mentioned, some components, especially branches, showed strong variability across trials. The wide spread in Shapley values for individual branches suggests they are more sensitive to topological changes in the grid. Since their relevance

is highly context-dependent, this complicates interpretation. Even if the overall vector remains similar, rankings can shift rapidly. This is a limitation if Shapley values are used for prioritization or investment planning.

Storage units, while stable in ranking, showed variation in magnitude under perturbations. This means that while their importance remains visible, the absolute value assigned can however fluctuate largely. This needs to be accounted for if the value is used for fine-grained decisions or payment allocation.

Another limitation is the use of only one grid. While the IEEE 14-bus system is common for testing, generalizability is limited. The results might look different for larger or differently structured networks. Moreover, only one objective—OPF cost—is used to define the Shapley value. Other system values might yield different Shapley distributions.

Despite these limitations, the overall findings indicate that the Shapley value retains much of its structure and meaning even under perturbations. It reacts as expected to parameter changes, and most types of players exhibit interpretable behavior. With this, the analysis provides a first step toward real-world applicability, offering guidance on where the method performs reliably and highlighting larger sensitivities that warrant deeper exploration.

11 Discussion & Outlook

Part II evaluates the use of the Shapley value as a fair and explainable allocation rule in power systems, moving from conceptual motivation to practical constraints. It assessed whether the value can capture the operational role of grid components such as generators, branches, and especially BESS units, in a transparent and robust way. Four aspects were addressed: privacy-preserving computation, AC realism, inclusion of storage, and robustness to perturbations. These steps reflect core challenges in real-world grid operation, where transparency and fairness are needed, but models must remain tractable, data cannot always be shared, and system conditions are constantly changing.

Contributions

Chapter 7 used a distributed Shapley computation based on the AC OPF model ALADIN to preserve model privacy when applying the Shapley value to congestions. Chapter 8 looked closer at the different outcomes of congestion and Shapley values based on DC and AC OPF computations and stated that they can be unexpectedly different. Chapter 9 used the Shapley value to define the utility of battery storage in a multi-period OPF setting, showing that the Shapley value can capture some effects better than default proportional methods. Chapter 10 conducted a robustness analysis using deterministic and stochastic perturbations to test how stable and meaningful the values remain under uncertainty.

Explainability The Shapley value offers additional insight into the complex interactions within power grids and supports more transparent infrastructure planning and fairer cost allocation. By quantifying individual component influence,

it can uncover technical drivers of system behavior that are otherwise hidden in aggregate results.

Relevance to practice Data privacy, physical accuracy (AC modeling), fair cost allocation, and robustness are key concerns in real-world grid operation. This work takes steps toward bridging theory and practice by addressing these challenges and demonstrating potential use cases. Also, it can serve as a starting point for practical adoption and inform further discussion on where and how such methods could be integrated into operational processes.

Limitations

Scope and scale Scalability, as well as the data basis, are clear limitations. All results are based on IEEE test grids, with only one chapter using a broader range of models. This means conclusions may not generalize to larger grids or different topologies. The computational cost of Shapley value estimation—especially in AC OPF—remains a bottleneck and is not explicitly benchmarked.

Missing integration into decision-making is another key gap. The Shapley value remains an interpretive tool here; no mechanisms are designed to act upon the results. There is no feedback from electricity price settings, incentives, or investment decisions to whether the value is useful in non-ideal assumptions.

Outlook

For practical deployment, the Shapley value approach should be embedded into larger frameworks to show its real benefits, e.g., pricing schemes, planning tools, or regulatory models. It could be tested whether it has an advantage in contrast to simpler values, test additional robustness under less ideal assumptions, see how scalable the approach has to be, and wether it can yield use case-specific insights.

Speaking of scalability, another open point is to model the Shapley value over a longer period of time to see how it behaves over the span of a year, for example.

12 Conclusion

This thesis looks at two increasingly critical aspects of modern transmission system operation: managing uncertainty from renewable energy sources and improving transparency about the influence of individual grid components. It combines optimization with cooperative game theory and demonstrates that both uncertainty management and transparency can be addressed with analytic and interpretable tools.

Part I addressed how BESS interact with uncertain RES generation and how they should be placed to maximize system benefit. The key contribution is a chance-constrained, multi-period DC-OPF that remains analytically exact under Gaussian uncertainty and includes affine control policies for storage. This model enabled a systematic evaluation of BESS on standard test systems and a realistic reconstruction of the Turkish transmission grid. Across all experiments, BESS reduced system costs, flattened generation profiles, and relieved transmission stress. The analysis also showed that BESS placement matters, with sites near load centers offering the highest systemic benefit.

Part II moves the Shapley value, suggested for redispatch cost allocation, towards practical application. A privacy-preserving distributed AC-OPF was embedded into the Shapley workflow, enabling cost allocations across large meshed grids without requiring the exchange of internal grid data. The comparison between DC and AC formulations revealed that DC-based allocations can be misleading, particularly in congested or reactive-power-constrained networks, highlighting the need for physical accuracy in attribution tasks. The concept of the Shapley value was further generalized toward assessing component utility, and applied to battery energy storage systems (BESS) in multi-period AC grids, capturing

their impact through both active and reactive power. To assess the robustness of Shapley-based allocations, a sensitivity analysis was conducted using both deterministic perturbations and Monte Carlo sampling. The results showed that Shapley values vary continuously with system changes and remain structurally stable for generators and storage units, while branches tend to be more sensitive to topological variations. Together, these contributions support a more transparent and physically grounded approach to evaluating component influence in power systems.

Limitations

There are several limitations to this work. Firstly, Part I relies on the DC approximation, which omits voltage magnitudes and reactive power. While necessary for analytical tractability, this limits realism, especially in voltage-constrained or distribution-level settings. Second, Gaussian uncertainty—though convenient—does not capture all forecast errors. Lastly, scalability remains restricted: horizons of 12 hours and systems beyond roughly 100 buses approach the computational limits of the model.

Part II also faces scalability issues, mainly due to the combinatorial complexity of the Shapley value, which grows exponentially with the number of players. Although the distributed AC-OPF generally enables larger systems, computing the full Shapley value is still expensive. To use the Shapley value as a utility metric, evaluation needs to be performed on larger grids to see how much it differs from the baseline of active power injections. Likewise, the robustness analysis has to be expanded to larger grids to see how the sensitivity of the Shapley values changes with different topologies.

Outlook

While the thesis advances analytical tools for flexibility and transparency, several research areas remain open. Extending the stochastic OPF to AC formulations—possibly through convex relaxations, hybrid DC–AC models, or data-driven surrogates—would enable more realistic uncertainty analysis. Also, scalability can be improved for both the OPF and Shapley framework; approaches can be to decompose the problem, for example into a hierarchical Shapley value, or to use learning-based approximations of the marginal contributions. Further, a large open question is where and how to integrate the Shapley value-based cost allocation; in the market environment, redispatch regulation, or investment planning, and model the surrounding system. For the Shapley value, fast approximation schemes and better baselines could make the approach more applicable in operational settings. Finally, as grids become more data-rich through PMUs, distributed sensors, and improved forecasting, combining these analytical tools with real-time observability may open the door to automated decision support systems.

In summary, this thesis contributes analytical methods that support both the operational management of uncertainty and the transparent evaluation of system influence. By combining tractable modeling and rigorous fairness concepts, it offers a step toward more explainable and resilient power system operation. However, further work is required to scale these methods and integrate them into real-world processes.

A Appendix

A.1 Turkish Transmission Grid Data

The following data for the Turkish transmission grid used in Chapter 4 and is given in the form of MATPOWER case files.

Further, there are default values for some components that are not contained in the tables: For the busses, the area is set to 1. For the branches, rateB, rateC, the ratio and angle are set to 0, and the status is 1. For the generators, the status is set to 1 as well, and Pc1, Pc2, Qc1min, Qc1max, Qc2min, Qc2max, ramp agc, ramp 10, ramp 30, ramp q, and apf are set to 0. The generator costs are complete.

Table A.1: Bus Data

Bus	Type	Pd	Qd	Gs	Bs	Vm	Va	BaseKV	Zone	Vmax	Vmin
1	3	758.07	168.46	0	0	1.015	0	345	1	1.06	0.94
2	1	0	0	0	0	0.9996	-3.038	345	1	1.06	0.94
3	1	0	0	0	0	0.9986	-3.348	345	1	1.06	0.94
4	1	0	0	0	0	0.9883	-4.081	345	1	1.06	0.94
5	1	0	0	0	0	0.9935	-3.294	345	1	1.06	0.94
6	1	0	0	0	0	0.9861	-4.178	345	1	1.06	0.94
7	1	0	0	0	0	0.9927	-3.489	345	1	1.06	0.94
8	1	0	0	0	0	1.0375	1.044	345	1	1.06	0.94

Continued on the next page

Bus	Type	Pd	Qd	Gs	Bs	Vm	Va	BaseKV	Zone	Vmax	Vmin
9	1	0	0	0	0	1.0112	3.225	345	1	1.06	0.94
10	1	0	0	0	0	1.0185	5.169	345	1	1.06	0.94
11	1	0	0	0	0	1.0063	3.408	345	1	1.06	0.94
12	1	0	0	0	0	0.9923	-14.53	345	1	1.06	0.94
13	1	0	0	0	0	0.9897	-8.987	345	1	1.06	0.94
14	1	0	0	0	0	0.9995	-6.196	345	1	1.06	0.94
15	1	0	0	0	0	1.016	-4.166	345	1	1.06	0.94
16	1	0	0	0	0	1.0045	-8.808	345	1	1.06	0.94
17	1	0	0	0	0	1.0001	-2.289	345	1	1.06	0.94
18	1	0	0	0	0	1.0137	-1.348	345	1	1.06	0.94
19	1	0	0	0	0	1.002	1.399	345	1	1.06	0.94
20	1	0	0	0	0	1.0058	-1.699	345	1	1.06	0.94
21	1	0	0	0	0	1.0232	-0.648	345	1	1.06	0.94
22	1	0	0	0	0	1.0052	-1.184	345	1	1.06	0.94
23	1	0	0	0	0	1.0125	4.470	345	1	1.06	0.94
24	1	0	0	0	0	0.9944	0.9564	345	1	1.06	0.94
25	1	0	0	0	0	1.0272	3.193	345	1	1.06	0.94
26	1	0	0	0	0	1.0209	6.588	345	1	1.06	0.94
27	1	0	0	0	0	1.0115	-6.806	345	1	1.06	0.94
28	1	0	0	0	0	1.017	-6.984	345	1	1.06	0.94
29	1	0	0	0	0	1.0246	-1.179	345	1	1.06	0.94
30	1	0	0	0	0	0.9938	-2.312	345	1	1.06	0.94
31	1	0	0	0	0	0.9638	-5.282	345	1	1.06	0.94
32	1	0	0	0	0	1.0088	-0.2473	345	1	1.06	0.94
33	2	0	0	0	0	1.0129	3.349	345	1	1.06	0.94

Continued on the next page

Bus	Type	Pd	Qd	Gs	Bs	Vm	Va	BaseKV	Zone	Vmax	Vmin
34	1	0	0	0	0	1.0109	2.575	345	1	1.06	0.94
35	1	0	0	0	0	1.0885	-10.39	345	1	1.06	0.94
36	2	510	136	0	0	1.01	-1.258	345	1	1.06	0.94
37	2	693	184.8	0	0	1.02	5.907	345	1	1.06	0.94
38	2	678	180.8	0	0	1.03	-0.7999	345	1	1.06	0.94
39	2	0	0	0	0	1.02	0.9894	345	1	1.06	0.94
40	2	555	148	0	0	1.02	1.126	345	1	1.06	0.94
41	1	0	0	0	0	1.02	0.98	345	1	1.06	0.94
42	2	514.5	137	0	0	1.01	1.881	345	1	1.06	0.94
43	2	960	256	0	0	1.02	6.14	345	1	1.06	0.94
44	2	1903	607.5	0	0	1.02	5.363	345	1	1.06	0.94
45	1	330	88	0	0	1.01	5.817	345	1	1.06	0.94
46	2	435	156	0	0	1.03	4.895	345	1	1.06	0.94
47	2	495	132	0	0	1.03	5.594	345	1	1.06	0.94
48	2	330	88	0	0	1.01	5.817	345	1	1.06	0.94
49	2	375	100	0	0	1.02	-12.02	345	1	1.06	0.94
50	2	0	0	0	0	1.01	-2.442	345	1	1.06	0.94
51	2	435	116	0	0	1.0117	1.202	345	1	1.06	0.94
52	2	250.5	-66.8	0	0	1.001	0.6819	345	1	1.06	0.94
53	1	0	0	0	0	1.0111	-0.2622	345	1	1.06	0.94
54	2	2100	560	0	0	1.011	1.364	345	1	1.06	0.94
55	1	0	0	0	0	1.011	-0.5653	345	1	1.06	0.94
56	2	474	126.4	0	0	1.02	-0.2161	345	1	1.06	0.94
57	2	1980	528	0	0	1.02	0.9146	345	1	1.06	0.94
58	2	1260	336	0	0	1.041	2.934	345	1	1.06	0.94

Continued on the next page

Bus	Type	Pd	Qd	Gs	Bs	Vm	Va	BaseKV	Zone	Vmax	Vmin
59	2	0	0	0	0	1.041	-0.4667	345	1	1.06	0.94
60	2	445.5	120	0	0	1.011	5.185	345	1	1.06	0.94
61	2	877.5	234	0	0	1.011	7.882	345	1	1.06	0.94

Table A.2: Branch Data

From	To	R (Ohms)	X (Ohms)	B (Mvar)	RateA	Angle Min	Angle Max
1	4	0.0001	0.0016	0	750	-60	60
1	38	0.0001	0.0014	0	750	-60	60
2	3	0.0001	0.0011	0	750	-60	60
2	5	0.0001	0.0013	0	750	-60	60
2	38	0.0001	0.0013	0	750	-60	60
2	54	0.0001	0.0014	0	750	-60	60
3	4	0.0001	0.0011	0	750	-60	60
3	38	0.0001	0.0012	0	750	-60	60
3	39	0.0001	0.0011	0	750	-60	60
4	5	0.0001	0.0012	0	1000	-60	60
4	6	0.0001	0.0012	0	750	-60	60
5	6	0.0001	0.0011	0	750	-60	60
5	7	0.0001	0.0011	0	750	-60	60
5	54	0.0001	0.0014	0	1000	-60	60
6	7	0.0001	0.0011	0	500	-60	60
7	20	0.0001	0.0019	0	1000	-60	60
7	40	0.0001	0.0016	0	500	-60	60

Continued on the next page

From	To	R (Ohms)	X (Ohms)	B (Mvar)	RateA	Angle Min	Angle Max
7	53	0.0001	0.0014	0	500	-60	60
8	40	0.0001	0.0017	0	750	-60	60
8	43	0.0001	0.0018	0	750	-60	60
9	41	0.0001	0.0015	0	500	-60	60
9	43	0.0001	0.0013	0	500	-60	60
10	11	0.0001	0.0013	0	750	-60	60
10	43	0.0001	0.0011	0	500	-60	60
10	45	0.0001	0.0012	0	500	-60	60
10	44	0.0001	0.0010	0	1000	-60	60
11	47	0.0001	0.0014	0	750	-60	60
12	34	0.0001	0.0017	0	750	-60	60
12	49	0.0001	0.0013	0	500	-60	60
13	14	0.0001	0.0013	0	500	-60	60
13	35	0.0001	0.0025	0	500	-60	60
14	15	0.0001	0.0013	0	500	-60	60
14	50	0.0001	0.0015	0	750	-60	60
15	59	0.0001	0.0013	0	500	-60	60
16	18	0.0001	0.0020	0	500	-60	60
16	35	0.0001	0.0014	0	500	-60	60
17	19	0.0001	0.0022	0	500	-60	60
17	20	0.0001	0.0011	0	500	-60	60
17	52	0.0001	0.0017	0	500	-60	60
18	57	0.0001	0.0024	0	1000	-60	60
19	33	0.0001	0.0022	0	500	-60	60
19	59	0.0001	0.0016	0	500	-60	60

Continued on the next page

From	To	R (Ohms)	X (Ohms)	B (Mvar)	RateA	Angle Min	Angle Max
20	18	0.0001	0.0023	0	1000	-60	60
20	25	0.0001	0.0022	0	750	-60	60
20	36	0.0001	0.0013	0	500	-60	60
20	54	0.0001	0.0019	0	1000	-60	60
20	55	0.0001	0.0017	0	500	-60	60
20	59	0.0001	0.0030	0	750	-60	60
21	25	0.0001	0.0019	0	750	-60	60
21	55	0.0001	0.0019	0	750	-60	60
22	55	0.0001	0.0012	0	500	-60	60
23	25	0.0001	0.0015	0	500	-60	60
23	37	0.0001	0.0014	0	750	-60	60
23	60	0.0001	0.0011	0	500	-60	60
24	27	0.0001	0.0029	0	1000	-60	60
24	60	0.0001	0.0019	0	1000	-60	60
25	26	0.0001	0.0017	0	750	-60	60
25	37	0.0001	0.0014	0	500	-60	60
26	61	0.0001	0.0013	0	750	-60	60
27	28	0.0001	0.0014	0	750	-60	60
27	29	0.0001	0.0019	0	750	-60	60
29	33	0.0001	0.0016	0	750	-60	60
30	31	0.0001	0.0014	0	750	-60	60
30	58	0.0001	0.0014	0	750	-60	60
31	32	0.0001	0.0022	0	750	-60	60
32	57	0.0001	0.0013	0	750	-60	60
33	58	0.0001	0.0014	0	500	-60	60

Continued on the next page

From	To	R (Ohms)	X (Ohms)	B (Mvar)	RateA	Angle Min	Angle Max
33	58	0.0001	0.0013	0	500	-60	60
33	61	0.0001	0.0016	0	750	-60	60
34	45	0.0001	0.0016	0	750	-60	60
34	46	0.0001	0.0015	0	750	-60	60
35	49	0.0001	0.0014	0	500	-60	60
35	51	0.0001	0.0023	0	500	-60	60
36	53	0.0001	0.0016	0	500	-60	60
40	41	0.0001	0.0010	0	500	-60	60
40	53	0.0001	0.0016	0	500	-60	60
41	42	0.0001	0.0014	0	500	-60	60
42	51	0.0001	0.0012	0	500	-60	60
45	46	0.0001	0.0016	0	750	-60	60
45	51	0.0001	0.0022	0	500	-60	60
46	47	0.0001	0.0012	0	500	-60	60
46	48	0.0001	0.0010	0	500	-60	60
50	56	0.0001	0.0012	0	750	-60	60
50	57	0.0001	0.0014	0	750	-60	60
51	52	0.0001	0.0012	0	500	-60	60
52	53	0.0001	0.0014	0	500	-60	60
53	54	0.0001	0.0010	0	750	-60	60
54	55	0.0001	0.0013	0	750	-60	60
56	57	0.0001	0.0013	0	500	-60	60
57	58	0.0001	0.0017	0	500	-60	60
57	59	0.0001	0.0017	0	750	-60	60

Table A.3: Generator Data

Bus	Pg	Qg	Pmin	Pmax	Qmin	Qmax	Vg	mBase
1	610	0	0	732	-100	100	1.0658	100
33	1125	0	0	1350	-100	100	1.0133	100
36	394	0	0	472.8	-100	100	0.8986	100
37	262	0	0	314.4	-100	100	1.0509	100
38	445	0	0	534	-100	100	1.1265	100
39	9975	0	0	11970	-100	100	0.9842	100
40	365	0	0	438	-100	100	0.9101	100
42	156	0	0	187.2	-100	100	0.8882	100
43	576	0	0	691.2	-100	100	0.8758	100
44	1449	0	0	1738.8	-100	100	1.0398	100
46	350	0	0	420	-100	100	1.0339	100
47	297	0	0	356.4	-100	100	0.9216	100
48	182	0	0	218.4	-100	100	1.0754	100
49	250	0	0	300	-100	100	0.8934	100
50	1032	0	0	1238.4	-100	100	1.1487	100
51	262	0	0	314.4	-100	100	0.7872	100
52	167	0	0	200.4	-100	100	0.9726	100
54	1704	0	0	2044.8	-100	100	1.0753	100
56	416	0	0	499.2	-100	100	1.0012	100
57	1320	0	0	1584	-100	100	1.0049	100
58	840	0	0	1008	-100	100	0.9491	100
59	273	0	0	327.6	-100	100	1.1965	100
60	200	0	0	240	-100	100	0.954	100
61	536.66	0	0	643.992	-100	100	1.0698	100

Table A.4: Generator Cost

Model	Startup	Shutdown	n	c_{n-1}	c_{n-2}	c_0
2	0	0	3	0.01	0.3	0.2
2	0	0	3	0.01	0.3	0.2
2	0	0	3	0.01	0.3	0.2
2	0	0	3	0.01	0.3	0.2
2	0	0	3	0.01	0.3	0.2
2	0	0	3	0.01	0.3	0.2
2	0	0	3	0.01	0.3	0.2
2	0	0	3	0.01	0.3	0.2
2	0	0	3	0.01	0.3	0.2
2	0	0	3	0.01	0.3	0.2
2	0	0	3	0.01	0.3	0.2
2	0	0	3	0.01	0.3	0.2
2	0	0	3	0.01	0.3	0.2
2	0	0	3	0.01	0.3	0.2
2	0	0	3	0.01	0.3	0.2
2	0	0	3	0.01	0.3	0.2
2	0	0	3	0.01	0.3	0.2
2	0	0	3	0.01	0.3	0.2
2	0	0	3	0.01	0.3	0.2
2	0	0	3	0.01	0.3	0.2
2	0	0	3	0.01	0.3	0.2
2	0	0	3	0.01	0.3	0.2
2	0	0	3	0.01	0.3	0.2
2	0	0	3	0.01	0.3	0.2
2	0	0	3	0.01	0.3	0.2
2	0	0	3	0.01	0.3	0.2
2	0	0	3	0.01	0.3	0.2

A.2 Additional results for IEEE case39

These results refer to Chapter 3.

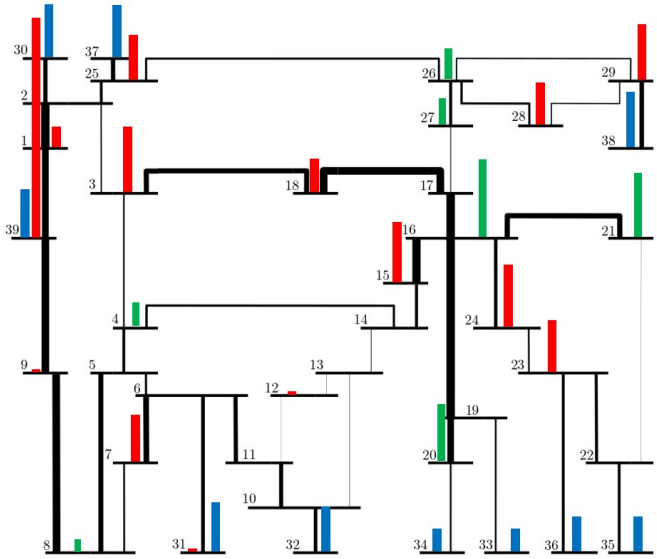

Figure A.1: ieee case39: Network state without (upper) and with (lower) storage at time $t = 9$, with generation (dark blue), wind generation (light blue), loads (red), storage (green) and line flows (black).

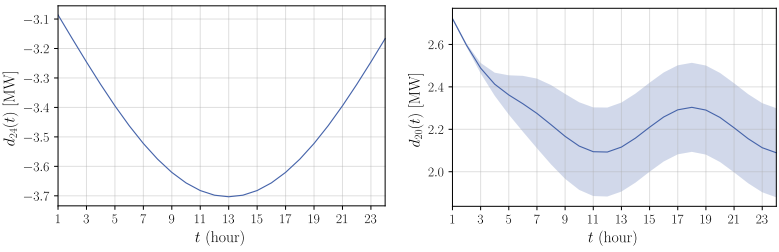

(a) Left: fixed load d_{20}; right: the uncertain load d_{24}.

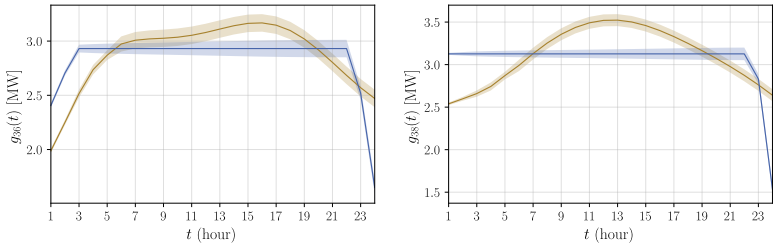

(b) Power injections of generators $\{g_{36}, g_{38}\}$.

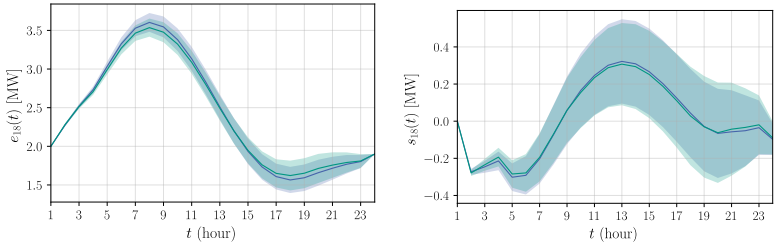

(c) Left: Power injections of storage s_{18}; right: respective change of power.

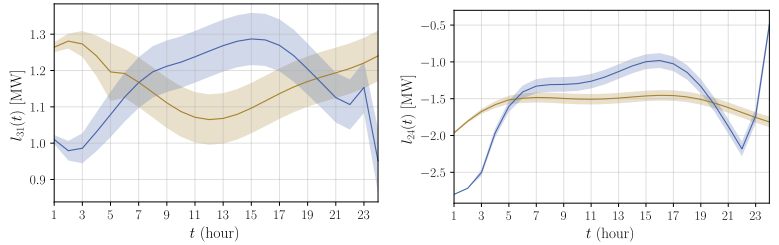

(d) Line flows of lines $\{l_{31}, l_{24}\}$.

Figure A.2: OPF results for the IEEE 39-bus grid with real-world wind generation without storage (S1, brown), with storage (S2, blue), and with storage and variance constraints (S3, green). The random variables x are depicted with their mean $\mathbb{E}(\mathsf{x})$ (solid) and scaled standard deviation $\mathbb{E}(\mathsf{x}) \pm \lambda(0.05)\sqrt{\mathbb{V}(\mathsf{x})}$ (shaded).

A.3 Modifications of IEEE test cases

These modifications refer to the grids used in Chapter 8.

Table A.5: Modifications for Various IEEE and PGLib Case Files.

Case	Parameter	Changes
IEEE case9	**Loads**	$\{90, 100, 125\}\ \forall i \in \{5, 7, 9\}$
	RateA	$\{70, 40\}\ \forall i \in \{1, 4\}$
	Gen Cost	$\{32, 25, 20\}\ \forall i \in \{1, 2, 3\}$
	Plim	$1000\ \forall i \in \mathcal{L}$
	RateB/C	$0\ \forall i \in \mathcal{L}$
IEEE case39	**RateA**	$\{100, 30, 90\}\ \forall i \in \{1, 2, 4\}$
	Loads	$\{0, 0, 0, 0, 90, 0, 100, 0, 125, 0\}$ $\forall i \in \{1, 2, 3, 4, 5, 6, 7, 8, 9, 10\}$
PGLib case118	**-**	-
IEEE case300	**RateA**	$1000\ \forall i \in \mathcal{L}$
PGLib case793	**RateA**	$\cdot 1.4$
PGLib case1354	**RateA**	$\cdot 1.2$
IEEE case2383	**RateA**	Increase several rateA values by 10 to 200
	Load	Reduce load by $\cdot 0.9$

A.4 Additional results for the IEEE case14

These results refer to Chapter 10. They give the comparison of AC and DC OPF-based Shapley value computation for three storage units in the IEEE 14-bus test grid.

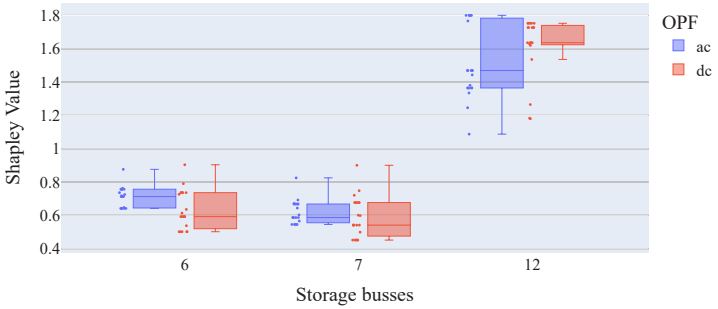

Figure A.3: Distribution of Shapley values for storage units at buses 6, 7, and 12 under capacity perturbations.

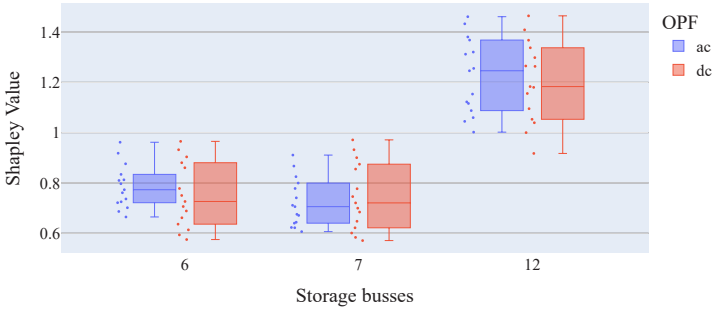

Figure A.4: Distribution of Shapley values for storage units at buses 6, 7, and 12 under efficiency perturbations.

List of Figures

List of Tables

List of Publications

Rebecca Bauer, Tillmann Mühlpfordt, Nicole Ludwig, and Veit Hagenmeyer. Analytical uncertainty propagation and storage usage in a high RES Turkish transmission grid scenario. In *Proceedings of the Thirteenth ACM International Conference on Future Energy Systems*, e-Energy '22, pages 489–495, New York, NY, USA, 2022. Association for Computing Machinery. doi: 10.1145/3538637.3539762.

Rebecca Bauer, Xinliang Dai, and Veit Hagenmeyer. A Shapley value-based Distributed AC OPF Approach for Redispatch Congestion Cost Allocation. In *Proceedings of the 14th ACM International Conference on Future Energy Systems*, e-Energy '23, pages 109–113, New York, NY, USA, 2023a. Association for Computing Machinery. doi: 10.1145/3575813.3576881.

Rebecca Bauer, Tillmann Mühlpfordt, Nicole Ludwig, and Veit Hagenmeyer. Analytical uncertainty propagation for multi-period stochastic optimal power flow. *Sustainable Energy, Grids and Networks*, 33:100969, 2023b. doi: 10.1016/j.segan.2022.100969.

Rebecca Bauer, Xinliang Dai, and Veit Hagenmeyer. Industrial Application of the Shapley value-based Redispatch Cost Allocation to Large-Scale Power Grids requires AC Optimal Power Flow. In *2024 IEEE Power & Energy Society General Meeting (PESGM)*, pages 1–5, 2024. doi: 10.1109/PESGM51994.2024.10688852.

Rebecca Bauer, Xinliang Dai, Frederik Zahn, and Veit Hagenmeyer. Shapley value-based cost allocation for Battery Energy Storage Systems in Power Grids with a High Share of Renewables. In *Proceedings of the 16th ACM International*

Conference on Future and Sustainable Energy Systems, E-Energy '25, pages 650–655, New York, NY, USA, 2025. Association for Computing Machinery. doi: 10.1145/3679240.3734664.

Bibliography

Quake in Turkey highlights the hazard in the East Bay, 2020. URL https://seismo.berkeley.edu/blog/2020/01/26/quake-in-turkey-highlights-the-hazard-in-the-east-bay.html.

50Hertz, TenneT, TransnetBW, and Amprion. Netzentwicklungsplan 2037/2045 (2023), 2023. URL https://www.netzentwicklungsplan.de/nep-aktuell/netzentwicklungsplan-20372045-2023.

AFAD. AFAD Press Bulletin - Izmir Turkey Earthquake Report as of 6 November 2020 - Türkiye | ReliefWeb, 2020. URL https://reliefweb.int/report/turkey/afad-press-bulletin-izmir-turkey-earthquake-report-6-november-2020.

International Energy Agency. Turkey 2021 Energy Policy Review. *IEA Energy Policy Reviews*, 2021. doi: 10.1787/0633467f-en. URL https://www.oecd.org/en/publications/turkey-2021-energy-policy-review_0633467f-en.html.

Khaled Alshehri, Ji Liu, Xudong Chen, and Tamer Başar. A Game-Theoretic Framework for Multiperiod-Multicompany Demand Response Management in the Smart Grid. *IEEE Transactions on Control Systems Technology*, 29:1019–1034, 2021. doi: 10.1109/TCST.2020.2989272.

Joel A. E. Andersson, Joris Gillis, Greg Horn, James B. Rawlings, and Moritz Diehl. CasADi: a software framework for nonlinear optimization and optimal control. *Mathematical Programming Computation*, 11(1):1–36, 2019. doi: 10.1007/s12532-018-0139-4.

Ayesha, Muhammad Numan, Musaed Alhussein, Muhammad Faisal Baig, and Khursheed Aurangzeb. Enhancing grid flexibility with coordinated battery storage and smart transmission technologies. *Journal of Energy Storage*, 100: 113607, 2024. doi: 10.1016/j.est.2024.113607.

Flavio Azevedo, Sam Parsons, and Leticia Micheli. Robustness (analyses). URL `https://forrt.org/glossary/english/robustness/`.

S. Babaeinejadsarookolaee, A. Birchfield, R. Christie, Carleton Coffrin, C. DeMarco, R. Diao, M. Ferris, S. Fliscounakis, Scott Greene, Renke Huang, C. Josz, R. Korab, B. Lesieutre, J. Maeght, D. Molzahn, T. Overbye, P. Panciatici, Byungkwon Park, Jonathan Snodgrass, and R. Zimmerman. The Power Grid Library for Benchmarking AC Optimal Power Flow Algorithms. *ArXiv*, 2019. doi: arXiv:1908.02788.

Kyri Baker. Solutions of DC OPF are Never AC Feasible. pages 264–268, 2021. doi: 10.1145/3447555.3464875.

R. Baldick, B.H. Kim, C. Chase, and Yufeng Luo. A fast distributed implementation of optimal power flow. *IEEE Transactions on Power Systems*, 14(3): 858–864, 1999. doi: 10.1109/59.780896.

Halil Burak Bart. Turkey's Electricity Trade Relations with Europe: The Role of the EU and the Impact on the Environment. 2020. URL `http://www.iceee2020.com/docs/Conference_Proceedings.pdf`.

Rebecca Bauer, Tillmann Mühlpfordt, Nicole Ludwig, and Veit Hagenmeyer. Analytical uncertainty propagation and storage usage in a high RES Turkish transmission grid scenario. pages 489–495, 2022. doi: 10.1145/3538637.3539762.

Rebecca Bauer, Xinliang Dai, and Veit Hagenmeyer. A Shapley value-based Distributed AC OPF Approach for Redispatch Congestion Cost Allocation. pages 109–113, 2023a. doi: 10.1145/3575813.3576881.

Rebecca Bauer, Tillmann Mühlpfordt, Nicole Ludwig, and Veit Hagenmeyer. Analytical uncertainty propagation for multi-period stochastic optimal power

flow. *Sustainable Energy, Grids and Networks*, 33:100969, 2023b. doi: 10.1016/j.segan.2022.100969.

Rebecca Bauer, Xinliang Dai, and Veit Hagenmeyer. Industrial Application of the Shapley value-based Redispatch Cost Allocation to Large-Scale Power Grids requires AC Optimal Power Flow. pages 1–5, 2024. doi: 10.1109/PESGM51994.2024.10688852.

Rebecca Bauer, Xinliang Dai, Frederik Zahn, and Veit Hagenmeyer. Shapley value-based cost allocation for Battery Energy Storage Systems in Power Grids with a High Share of Renewables. pages 650–655, 2025. doi: 10.1145/3679240.3734664.

J. Bialek. Tracing the flow of electricity. *IEE Proceedings - Generation, Transmission and Distribution*, 143(4):313, 1996. doi: 10.1049/ip-gtd:19960461.

Daniel Bienstock and Abhinav Verma. Strong NP-Hardness of AC power flows feasibility. *Operations Research Letters*, 47(6):494–501, 2019. doi: 10.1016/j.orl.2019.08.009.

Daniel Bienstock, Michael Chertkov, and Sean Harnett. Chance Constrained Optimal Power Flow: Risk-Aware Network Control under Uncertainty. *SIAM Review*, 56, 2012. doi: 10.1137/130910312.

Nate Blair, Chad Augustine, Wesley Cole, Paul Denholm, Will Frazier, Madeline Geocaris, Jennie Jorgenson, Kevin McCabe, Kara Podkaminer, Ashreeta Prasanna, and Ben Sigrin. Storage Futures Study: Key Learnings for the Coming Decades. 2022. doi: 10.2172/1863547.

M. Blum and M. Riedmiller. Electricity demand forecasting using gaussian processes. *Proceedings of Twenty-seventh AAAI Conference on Artificial Intelligence (AAAI-13)*, pages 10–13, 2013.

BMWK. Electricity Storage Strategy. 2023a. URL `https://www.bundeswirtschaftsministerium.de/Redaktion/DE/Publikationen/Energie/electricity-storage-strategy.pdf?__blob=publicationFile&v=4`.

BMWK. Roadmap Systemstabilität. 2023b. URL https://www.bundeswirtschaftsministerium.de/Redaktion/DE/Dossier/roadmap-systemstabilitaet.html.

Matthias A. Bucher, Miguel A. Ortega-Vazquez, Daniel S. Kirschen, and Göran Andersson. Robust allocation of reserves considering different reserve types and the flexibility from HVDC. *IET Generation, Transmission & Distribution*, 11(6):1472–1478, 2017. doi: 10.1049/iet-gtd.2016.1014.

Sylvain Béal, Sylvain Ferrières, Eric Rémila, and Philippe Solal. The proportional Shapley value and applications. *Games and Economic Behavior*, 108:93–112, 2018. doi: 10.1016/j.geb.2017.08.010.

Florin Capitanescu, Stéphane Fliscounakis, Patrick Panciatici, and Louis Wehenkel. Cautious Operation Planning Under Uncertainties. *IEEE Transactions on Power Systems*, 27(4):1859–1869, 2012. doi: 10.1109/TPWRS.2012.2188309.

André Casajus and Frank Huettner. The Coleman–Shapley index: being decisive within the coalition of the interested. *Public Choice*, 181(3):275–289, 2019. doi: 10.1007/s11127-019-00654-y.

Jean-François Caulier, Alexandre Skoda, and Emily Tanimura. Allocation Rules for Networks Inspired by Cooperative Game-Theory. *Revue d'économie politique*, 127(4):517–558, 2017. doi: 10.3917/redp.274.0517.

N. Chen, Z. Qian, I.T. Nabney, and X. Meng. Wind power forecasts using gaussian processes and numerical weather prediction. *IEEE Transactions on Power Systems*, 29(2):656–665, 2014. doi: 10.1109/tpwrs.2013.2282366.

A.J. Conejo, J.M. Arroyo, N. Alguacil, and A.L. Guijarro. Transmission loss allocation: a comparison of different practical algorithms. *IEEE Transactions on Power Systems*, 17(3):571–576, 2002. doi: 10.1109/TPWRS.2002.800894.

Antonio J. Conejo, Javier Contreras, Delberis A. Lima, and Antonio Padilha-Feltrin. Z-bus Transmission Network Cost Allocation. *IEEE Transactions on Power Systems*, 22(1):342–349, 2007. doi: 10.1109/TPWRS.2006.889138.

Xinliang Dai, Yichen Cai, Yuning Jiang, and Veit Hagenmeyer. Rapid scalable distributed power flow with open-source implementation. *IFAC-PapersOnLine*, 55(13):145–150, 2022. doi: 10.1016/j.ifacol.2022.07.250.

Xinliang Dai, Yi Guo, Yuning Jiang, Colin N. Jones, Gabriela Hug, and Veit Hagenmeyer. Real-time coordination of integrated transmission and distribution systems: Flexibility modeling and distributed NMPC scheduling. *Electric Power Systems Research*, 234:110627, 2024. doi: 10.1016/j.epsr.2024.110627.

Xinliang Dai, Junyi Zhai, Yuning Jiang, Yi Guo, Colin N. Jones, and Veit Hagenmeyer. Advancing Distributed AC Optimal Power Flow for Integrated Transmission-Distribution Systems. *IEEE Transactions on Network Science and Engineering*, 12:1210–1223, 2025. doi: 10.1109/TNSE.2025.3526206.

Morton Davis and Michael Maschler. The kernel of a cooperative game. *Naval Research Logistics Quarterly*, 12(3):223–259, 1965. doi: 10.1002/nav.3800120303.

Matteo De Felice. ENTSO-E Actual Generation of Wind units: data from 21-12-2014 to 11-04-2021, 2021. URL `https://zenodo.org/records/4682697`.

Ehsan Dehnavi, Farrokh Aminifar, and Saeed Afsharnia. Congestion management through distributed generations and energy storage systems. *International Transactions on Electrical Energy Systems*, 29(6):e12018, 2019. doi: 10.1002/2050-7038.12018.

Huajie Ding, Pierre Pinson, Zechun Hu, and Yonghua Song. Optimal Offering and Operating Strategies for Wind-Storage Systems With Linear Decision Rules. *IEEE Transactions on Power Systems*, 31(6):4755–4764, 2016. doi: 10.1109/TPWRS.2016.2521177.

David Duvenaud. Automatic model construction with Gaussian processes. 2014. doi: 10.17863/CAM.14087. URL `https://www.repository.cam.ac.uk/handle/1810/247281`.

Alexander Engelmann, Yuning Jiang, Tillmann Mühlpfordt, Boris Houska, and Timm Faulwasser. Toward Distributed OPF Using ALADIN. *IEEE Transactions on Power Systems*, 34:584–594, 2019. doi: 10.1109/TPWRS.2018.2867682.

ENTSO-E. Ten-Year Network Development Plan (TYNDP) 2020, 2020. URL https://consultations.entsoe.eu/system-development/tyndp2020/.

ENTSO-E. PICASSO, 2022. URL https://www.entsoe.eu/network_codes/eb/picasso/.

ENTSO-E. ENTSO-E TYNDP 2022 High-Level Report – Final Version May 2023. 2023. URL https://eepublicdownloads.blob.core.windows.net/public-cdn-container/tyndp-documents/TYNDP2022/public/high-level-report.pdf.

Tomaso Erseghe. Distributed Optimal Power Flow Using ADMM. *IEEE Transactions on Power Systems*, 29:2370–2380, 2014. doi: 10.1109/TPWRS.2014.2306495.

EU. Review of current national rules and practices relating to risk preparedness in the area of security of electricity supply – final report. 2014. doi: doi/10.2832/778934.

EUROPEAN, European Commission, and Directorate-General for Neighbourhood and Enlargement Negotiations. Türkiye Report 2024 - European Commission, 2024. URL https://enlargement.ec.europa.eu/turkiye-report-2024_en.

Luca Fabietti, Tomasz T. Gorecki, Emil Namor, Fabrizio Sossan, Mario Paolone, and Colin N. Jones. Dispatching active distribution networks through electrochemical storage systems and demand side management. pages 1241–1247, 2017. doi: 10.1109/CCTA.2017.8062629.

Luca Fabietti, Tomasz T. Gorecki, Faran A. Qureshi, Altuğ Bitlislioğlu, Ioannis Lymperopoulos, and Colin N. Jones. Experimental Implementation of Frequency Regulation Services Using Commercial Buildings. *IEEE Transactions on Smart Grid*, 9(3):1657–1666, 2018. doi: 10.1109/TSG.2016.2597002.

M. Gloria Fiestras-Janeiro, Ignacio García-Jurado, and Manuel A. Mosquera. Cooperative games and cost allocation problems. *TOP*, 19(1):1–22, 2011. doi: 10.1007/s11750-011-0200-1.

BMWK-Federal Ministry for Economic Affairs and Climate. First rules of new 2023 RES Act enter into force: renewable energy first and higher remuneration for solar power, 2022. URL https://www.bmwk.de/Redaktion/EN/Pressemitteilungen/2022/07/20220729-first-rules-of-new-2023-res-act-enter-into-force-renewable-energy-first-and-higher-remuneration-for-solar-power.html.

Stephen Frank and Steffen Rebennack. An introduction to optimal power flow: Theory, formulation, and examples. *IIE Transactions*, 48(12):1172–1197, 2016. doi: 10.1080/0740817X.2016.1189626.

Frederik Geth, Carleton Coffrin, and David Fobes. A Flexible Storage Model for Power Network Optimization. pages 503–508, 2020. doi: 10.1145/3396851.3402121.

Philipp Godron, Mahmut Erkut Cebeci, Osman Bülent Tör, and Deger Saygin. Increasing the Share of Renewables in Turkey's Power System: Options for Transmission Expansion and Flexibility, 2018. URL https://www.google.com/url?sa=t&rct=j&q=&esrc=s&source=web&cd=&cad=rja&uact=8&ved=2ahUKEwjcwvj62q72AhVSMewKHYhuCMMQFnoECAkQAQ&url=https%3A%2F%2Fwww.shura.org.tr%2Fwp-content%2Fuploads%2F2018%2F12%2FSHURA_Increasing-the-Share-of-Renewables-in-Turkeys-Power-System_Report.pdf&usg=AOvVaw3G08fND2D_UHI1W-yEO3Qx.

Alkım Bağ Gullu. SHURA-2024-07-Battery-Energy_yo_eng, 2024. URL https://shura.org.tr/wp-content/uploads/2024/12/SHURA-2024-07-Battery-Energy_YO_ENG.pdf?utm_source=chatgpt.com.

Georg Gutermuth and Marco Giuntoli. Network operator owned storages as an option for congestion management. pages 1074–1078, 2020. doi: 10.1109/ISGT-Europe47291.2020.9248825.

Osman Gürses. Türkiye'nin enerji alanındaki stratejik konumu, 2022. URL https://el-aziz.com/haber/9666460/turkiyenin-enerji-alanindaki-stratejik-konumu.

Reza Hemmati, Hedayat Saboori, and Saeid Saboori. Stochastic risk-averse coordinated scheduling of grid integrated energy storage units in transmission constrained wind-thermal systems within a conditional value-at-risk framework. *Energy*, 113:762–775, 2016. doi: 10.1016/j.energy.2016.07.089.

Samuel K. R. Homberg, Malte L. Modlich, Janosch Menke, Garrett M. Morris, Benjamin Risse, and Oliver Koch. Interpreting Graph Neural Networks with Myerson Values for Cheminformatics Approaches. 2024. doi: 10.26434/chemrxiv-2023-1hxxc-v2.

Jens Leth Hougaard. *An Introduction to Allocation Rules*. Springer, Berlin, Heidelberg, 2009. doi: 10.1007/978-3-642-01828-2.

B. Houska and Y. Jiang. Distributed Optimization and Control with ALADIN. pages 135–163, 2021. doi: 10.1007/978-3-030-63281-6_6.

Boris Houska, Janick Frasch, and Moritz Diehl. An augmented Lagrangian based algorithm for distributed nonconvex optimization. *SIAM J. Optim.*, 26(2):1101–1127, 2016. doi: 10.1109/TNSE.2025.3526206.

Yu Hu, Miguel Armada, and María Jesús Sánchez. Potential utilization of battery energy storage systems (BESS) in the major European electricity markets. *Applied Energy*, 322:119512, 2022. doi: 10.1016/j.apenergy.2022.119512.

Gabriela Hug-Glanzmann and GÖran Andersson. Decentralized Optimal Power Flow Control for Overlapping Areas in Power Systems. *IEEE Transactions on Power Systems*, 24:327–336, 2009. doi: 10.1109/TPWRS.2008.2006998.

Jonas Hörsch, Henrik Ronellenfitsch, Dirk Witthaut, and Tom Brown. Linear Optimal Power Flow Using Cycle Flows. *Electric Power Systems Research*, 158, 2017. doi: 10.1016/j.epsr.2017.12.034.

Marija Ilic, Francisco Galiana, and Lester Fink. *Power Systems Restructuring: Engineering and Economics*. Springer US, Boston, MA, 1998. doi: 10.1007/978-1-4757-2883-5.

International Energy Agency. *Electricity Grids and Secure Energy Transitions: Enhancing the Foundations of Resilient, Sustainable and Affordable Power Systems*. OECD, 2023. doi: 10.1787/455dd4fb-en.

IRENA. Energy Profile Turkey, 2021. URL https://www.google.com/url?sa=t&rct=j&q=&esrc=s&source=web&cd=&cad=rja&uact=8&ved=2ahUKEwjRmPLE2672AhUkwAIHHdFfDc4QFnoECA4QAQ&url=https%3A%2F%2Fwww.irena.org%2FIRENADocuments%2FStatistical_Profiles%2FEurasia%2FTurkey_Eurasia_RE_SP.pdf&usg=AOvVaw0ElYJNnuw6e1rz-k5M2jGG.

Japan International cooperation agency. The study on optimal power generation for peak demand in Turkey, 2011. URL https://openjicareport.jica.go.jp/pdf/12019808_01.pdf.

S. Prabhakar Karthikeyan, B. Saravanan, Aman Jain, Indrajit Ranu, I. Jacob Raglend, and D. P. Kothari. A comparative study on transmission network cost allocation methodologies. pages 145–152, 2013. doi: 10.1109/ICPEC.2013.6527640.

Timo Kern and Christian Wendlinger. Added Value of Providing Transmission Grid Congestion Management via Bidirectionally Chargeable Electric Vehicles. pages 1–9, 2022. doi: 10.1109/EEM54602.2022.9921051.

P. Kou, F. Gao, and X. Guan. Sparse online warped gaussian process for wind power probabilistic forecasting. *Applied Energy*, 108:410–428, 2013. doi: 10.1016/j.apenergy.2013.03.038.

Mehmet Kurban and Ummuhan Basaran Filik. Parameters and Power Flow Analysis of the 380 -kV Interconnected Power System in Turkey. pages 235–239, 2006. doi: 10.1109/PECON.2006.346653.

Francois Lamothe and Sandra Ulrich Ngueveu. Approximating the Shapley Value with Sampling: Survey and New Stratification Techniques. 2025. doi: 10.2139/ssrn.5093818.

D.J. Leith, M. Heidl, and J.V. Ringwood. Gaussian process prior models for electrical load forecasting. pages 112–117, 2004. doi: 10.1109/PMAPS.2004.242921.

Bowen Li and Johanna L. Mathieu. Analytical reformulation of chance-constrained optimal power flow with uncertain load control. pages 1–6, 2015. doi: 10.1109/PTC.2015.7232803.

Stan Lipovetsky. Handbook of the Shapley Value: by Encarnación Algaba, Vito Fragnelli, and Joaquín Sánchez-Soriano, editors. Boca Raton, FL: Chapman and Hall/CRC, Taylor & Francis Group, 2020, xxix + 576 pp., $160.00, ISBN: 978-0-8153-7468-8. *Technometrics*, 62(2):1–280, 2020. doi: 10.1080/00401706.2020.1744904.

Bingqing Liu, Ivan Kiskin, and Stephen Roberts. An Overview of Gaussian process Regression for Volatility Forecasting. pages 681–686, 2020. doi: 10.1109/ICAIIC48513.2020.9065045.

J.R. Lloyd. GEFCom2012 hierarchical load forecasting: Gradient boosting machines and gaussian processes. *International Journal of Forecasting*, 30(2):369–374, 2014. doi: 10.1016/j.ijforecast.2013.07.002.

Raphael Louca and Eilyan Bitar. Stochastic AC optimal power flow with affine recourse. pages 2431–2436, 2016. doi: 10.1109/CDC.2016.7798626.

F. McLoughlin, A. Duffy, and M. Conlon. Evaluation of time series techniques to characterise domestic electricity demand. *Energy*, 50:120–130, 2013. doi: 10.1016/j.energy.2012.11.048.

Georgios Mitrentsis and Hendrik Lens. Probabilistic Dynamic Model of Active Distribution Networks Using Gaussian Processes. pages 1–6, 2021. doi: 10.1109/PowerTech46648.2021.9494816.

H. Mori and M. Ohmi. Probabilistic short-term load forecasting with gaussian processes. pages 452–457, 2008. doi: 10.1109/isap.2005.1599306.

Daniel Munoz-Alvarez, Eilyan Bitar, Lang Tong, and Jianhui Wang. Piecewise affine dispatch policies for economic dispatch under uncertainty. pages 1–5, 2014. doi: 10.1109/PESGM.2014.6939369.

Tillmann Mühlpfordt. Uncertainty Quantification via Polynomial Chaos Expansion – Methods and Applications for Optimization of Power Systems. 2020. doi: 10.5445/IR/1000104661.

Tillmann Mühlpfordt, Timm Faulwasser, and Veit Hagenmeyer. Solving stochastic AC power flow via polynomial chaos expansion. pages 70–76, 2016. doi: 10.1109/CCA.2016.7587824.

Tillmann Mühlpfordt, Timm Faulwasser, Line Roald, and Veit Hagenmeyer. Solving optimal power flow with non-Gaussian uncertainties via polynomial chaos expansion. pages 4490–4496, 2017. doi: 10.1109/CDC.2017.8264321.

Tillmann Mühlpfordt, Timm Faulwasser, and Veit Hagenmeyer. A generalized framework for chance-constrained optimal power flow. *Sustainable Energy, Grids and Networks*, 16:231–242, 2018. doi: 10.1016/j.segan.2018.08.002.

Tillmann Mühlpfordt, Xinliang Dai, Alexander Engelmann, and Veit Hagenmeyer. Distributed power flow and distributed optimization—Formulation, solution, and open source implementation. *Sustainable Energy, Grids and Networks*, 26:100471, 2021. doi: 10.1016/j.segan.2021.100471.

Ramasuri Narayanam and Yadati Narahari. A Shapley Value-Based Approach to Discover Influential Nodes in Social Networks. *IEEE Transactions on Automation Science and Engineering*, 8(1):130–147, 2011. doi: 10.1109/TASE.2010.2052042.

Hung Cuong Nguyen, Quoc Tuan Tran, and Yvon Besanger. Effectiveness of BESS in Improving Frequency Stability of an Island Grid. *IEEE Transactions on Industry Applications*, 60:8203–8212, 2024. doi: 10.1109/TIA.2024.3443241.

Nhi T. A. Nguyen, Duong D. Le, Cristian Bovo, and Alberto Berizzi. Optimal Power Flow with energy storage systems: Single-period model vs. multi-period model. pages 1–6, 2015. doi: 10.1109/PTC.2015.7232438.

Brian A. Nosek and Timothy M. Errington. What is replication? *PLOS Biology*, 18(3):e3000691, 2020. doi: 10.1371/journal.pbio.3000691.

Meltem Peker, Ayse Kocaman, and Bahar Kara. A real data set for a 116-node power transmission system. 1, 2018. doi: 10.17632/dv3vjnwwf9.1.

Bezalel Peleg and Peter Sudhölter. *Introduction to the Theory of Cooperative Games*, volume 34 of *Theory and Decision Library*. Springer, Berlin, Heidelberg, 2007. doi: 10.1007/978-3-540-72945-7.

Hans Peters and Hans J. M. Peters. *Game theory: a multi-leveled approach*. Springer, Berlin Heidelberg, 2008. doi: 10.1007/978-3-540-69291-1.

Eléa Prat, Richard M. Lusby, Juan Miguel Morales, Salvador Pineda, and Pierre Pinson. How long is long enough? Finite-horizon approximation of energy storage scheduling problems. 2024. doi: 10.48550/arXiv.2411.17463.

Carl Edward Rasmussen and Christopher K. I. Williams. *Gaussian Processes for Machine Learning*. Adaptive Computation and Machine Learning. The MIT Press, Cambridge, MA, USA, 2005. doi: 10.7551/mitpress/3206.001.0001.

Line Roald, Frauke Oldewurtel, Thilo Krause, and Göran Andersson. Analytical reformulation of security constrained optimal power flow with probabilistic constraints. pages 1–6, 2013. doi: 10.1109/PTC.2013.6652224.

S. Roberts, M. Osborne, M. Ebden, S. Reece, N. Gibson, and S. Aigrain. Gaussian processes for time-series modelling. *Philosophical Transactions of the Royal Society A: Mathematical, Physical and Engineering Sciences*, 371(1984): 20110550–20110550, 2012. doi: 10.1098/rsta.2011.0550.

A. Rogers, S. Maleki, S. Ghosh, and N.R. Jennings. Adaptive home heating control through gaussian process prediction and mathematical programming. pages 71–78, 2011. URL https://files.core.ac.uk/download/pdf/1511823.pdf.

Alvin E. Roth. The Shapley Value - Essays in honor of Lloyd S. Shapley, 1988. URL https://catdir.loc.gov/catdir/samples/cam031/88002983.pdf.

David Schmeidler. The Nucleolus of a Characteristic Function Game. *SIAM Journal on Applied Mathematics*, 17(6):1163–1170, 1969. URL https://www.jstor.org/stable/2099196.

Mirja Schröder, Marc Oliver Bettzüge, and Wolfgang Wessels, editors. *Turkey as an energy hub? Contributions on Turkey's role in EU energy supply*. Number volume 1 in Turkey and European Union studies. Nomos, Baden-Baden, 1. auflage 2017 edition, 2017. doi: 10.5771/9783845282190.

Eric Schulz, Maarten Speekenbrink, and Andreas Krause. A tutorial on Gaussian process regression: Modelling, exploring, and exploiting functions. *Journal of Mathematical Psychology*, 85:1–16, 2018. doi: 10.1016/j.jmp.2018.03.001.

Erfang Shan, Zeguang Cui, and Wenrong Lyu. Gain–loss and new axiomatizations of the Shapley value. *Economics Letters*, 228:111168, 2023. doi: 10.1016/j.econlet.2023.111168.

Lloyd S. Shapley. A Value for N-Person Games. 1952. doi: 10.1515/9781400881970-018.

Lloyd S. Shapley. *Additive and Non-Additive Set Functions - ProQuest*. PhD thesis, Princeton University, 1953. URL https://perso.uclouvain.be/pierre.dehez/Shapley/Shapley-Thesis.pdf.

Satish Sharma and A.R. Abhyankar. Loss Allocation for Weakly Meshed Distribution System Using Analytical Formulation of Shapley Value. *IEEE Transactions on Power Systems*, 32:1369–1377, 2017. doi: 10.1109/TPWRS.2016.2571980.

H. Sheng, J. Xiao, Y. Cheng, Q. Ni, and S. Wang. Short-term solar power forecasting based on weighted gaussian process regression. *IEEE Transactions on Industrial Electronics*, 65(1):300–308, 2018. doi: 10.1109/tie.2017.2714127.

Yuge Shi. Gaussian Processes, not quite for dummies. *The Gradient*, 2019. URL https://thegradient.pub/machine-learning-ancient-japan/.

Martin Shubik. Incentives, Decentralized Control, the Assignment of Joint Costs and Internal Pricing. *Management Science*, 8(3):325–343, 1962. doi: 10.1287/mnsc.8.3.325.

Kadri SIMSON. European Commission Recommendations on Energy Storage – Underpinning a decarbonised and secure EU energy system, 2023. URL https://eur-lex.europa.eu/legal-content/EN/TXT/PDF/?uri=CELEX:32023H0320(01).

Emma Sjödin, Dennice F. Gayme, and Ufuk Topcu. Risk-mitigated optimal power flow for wind powered grids. pages 4431–4437, 2012. doi: 10.1109/ACC.2012.6315377.

Tyler Summers, Joseph Warrington, Manfred Morari, and John Lygeros. Stochastic optimal power flow based on conditional value at risk and distributional robustness | Elsevier Enhanced Reader. 72:116–125, 2015. doi: 10.1016/j.ijepes.2015.02.024.

Mahnoor Syed. Deep Dive: Turkey's Ambitious Renewable Energy Grid Modernisation, 2024. URL https://climateinsider.com/2024/11/04/deep-dive-turkeys-ambitious-renewable-energy-grid-modernisation/.

TEIAS. TEIAS Electrictiy Map, 2004. URL https://docplayer.biz.tr/4784458-Teias-turkiye-elektrik-iletim-a-s.html.

TEIAS. Turkey Blackout 2015 Report TEIAS, 2015. URL https://www.google.com/url?sa=t&rct=j&q=&esrc=s&source=web&cd=&cad=rja&uact=8&ved=2ahUKEwit1oPg2672AhUHwAIHHZC2CAQQFnoECAsQAQ&url=https%3A%2F%2Fwww.entsoe.eu%2FDocuments%2FSOC%2520documents%2FRegional_Groups_Continental_Europe%2F20150921_Black_Out_Report_v10_w.pdf&usg=AOvVaw3zISJVNGezjgIWugQD3t9r.

TenneT. Netzbooster Audorf, 2024. URL https://tennet-drupal.s3.eu-central-1.amazonaws.com/default/2025-01/TenneT_Factsheet_Netzbooster_Audorf.pdf.

TenneT and TransnetBW. Hybrides Redisptach-Modell: Integration von Kleinanlagen und Optionen für den Umgang mit Marktmacht und Inc-Dec-Gaming, 2024. URL https://www.transnetbw.de/_Resources/Persistent/2/1/4/4/2144f33f644f0e00fb772377109561c30dce3b0e/2024-Frontier-Marktbasierter%20Redispatch.pdf.

Inc. The MathWorks. MathWorks, 2021. URL https://www.mathworks.com/products/matlab.html.

Maurizio Titz, Sebastian Pütz, and Dirk Witthaut. Identifying drivers and mitigators for congestion and redispatch in the German electric power system with explainable AI. *Applied Energy*, 356:122351, 2024. doi: 10.1016/j.apenergy.2023.122351.

Menekse Tokyay. Turkish industry copes with abrupt cut of gas flow from Iran, 2022. URL https://arab.news/m2zja.

Mahsa Bagheri Tookanlou, Mostafa Malekpour, Rasoul Azizipanah Abarghooee, Mazaher Karimi, and Bahaa Eltahawy. Battery Energy Storage System Performance during Black-Start, Voltage and Frequency Disturbances. pages 1–6, 2023. doi: 10.1109/FES57669.2023.10182694.

TransnetBW. Netzbooster Kupferzell, 2024. URL https://www.transnetbw.de/de/netzentwicklung/projekte/netzbooster-kupferzell.

Muhammad Usman and Florin Capitanescu. A Stochastic Multi-period AC Optimal Power Flow for Provision of Flexibility Services in Smart Grids. pages 1–6, 2021. doi: 10.1109/PowerTech46648.2021.9495045.

Tjeerd van Campen, Herbert Hamers, Bart Husslage, and Roy Lindelauf. A new approximation method for the Shapley value applied to the WTC 9/11 terrorist attack. *Social Network Analysis and Mining*, 8(1):3, 2017. doi: 10.1007/s13278-017-0480-z.

Eric van Damme. On the State of the Art in Game Theory: An Interview with Robert Aumann. *Games and Economic Behavior*, 24(1):181–210, 1998. doi: 10.1006/game.1997.0612.

Ivo A. M. Varenhorst, Johann Hurink, and Marco E. T. Gerards. Quantifying Device Flexibility With Shapley Values in Demand Side Management. 2024. doi: 10.1145/3632775.3661950.

Simon Voswinkel. Simplifying the Computation of Shapley Values for Allocating Congestion Costs in Large Power Grid Models. *SSRN Electronic Journal*, 2023. doi: 10.2139/ssrn.4449794.

Simon Voswinkel, Jonas Höckner, Abuzar Khalid, and Christoph Weber. Sharing congestion management costs among system operators using the Shapley value. *Applied Energy*, 317:119039, 2022. doi: 10.1016/j.apenergy.2022.119039.

Maria Vrakopoulou and Ian A. Hiskens. Optimal policy-based control of generation and HVDC lines in power systems under uncertainty. pages 1–6, 2017. doi: 10.1109/PTC.2017.7981262.

Maria Vrakopoulou, Kostas Margellos, John Lygeros, and Göran Andersson. A Probabilistic Framework for Reserve Scheduling and \rm N-1 Security Assessment of Systems With High Wind Power Penetration. *IEEE Transactions on Power Systems*, 28(4):3885–3896, 2013. doi: 10.1109/TPWRS.2013.2272546.

Andy Walker and National Renewable Energy Laboratory (NREL). Battery Energy Storage System Evaluation Method. *National Renewable Energy Laboratory (NREL)*, 2023. doi: 10.2172/2279165.

Zhi-Yuan Wang and Hsiao-Dong Chiang. On the Feasibility of AC and DC Optimal Power Flow Models: Analytics and Comparison. pages 1–5, 2021. doi: 10.1109/PESGM46819.2021.9638005.

Joseph Warrington, Paul Goulart, Sébastien Mariéthoz, and Manfred Morari. Policy-Based Reserves for Power Systems. *IEEE Transactions on Power Systems*, 28(4):4427–4437, 2013. doi: 10.1109/TPWRS.2013.2269804.

Allen J Wood, Bruce F Wollenberg, eacute Shebl&amp, and Gerald B . Power Generation, Operation and Control. 2014. doi: 10.1016/0140-6701(96)88715-7.

Andreas Wächter and Lorenz T. Biegler. On the implementation of an interior-point filter line-search algorithm for large-scale nonlinear programming. *Mathematical Programming*, 106(1):25–57, 2006. doi: 10.1007/s10107-004-0559-y.

Weijun Xie and Shabbir Ahmed. Distributionally Robust Chance Constrained Optimal Power Flow with Renewables: A Conic Reformulation. *IEEE Transactions on Power Systems*, 33(2):1860–1867, 2018. doi: 10.1109/TPWRS.2017.2725581.

yWorks GmbH. yEd Graph Editor, 2019. URL `https://www.yworks.com/products/yed`.

Junyi Zhai, Xinliang Dai, Yuning Jiang, Ying Xue, Veit Hagenmeyer, Colin N. Jones, and Xiao-Ping Zhang. Distributed Optimal Power Flow for VSC-MTDC Meshed AC/DC Grids Using ALADIN. *IEEE Transactions on Power Systems*, 37(6):4861–4873, 2022. doi: 10.1109/TPWRS.2022.3155866.

Yiling Zhang, Siqian Shen, and Johanna L. Mathieu. Distributionally Robust Chance-Constrained Optimal Power Flow With Uncertain Renewables and Uncertain Reserves Provided by Loads. *IEEE Transactions on Power Systems*, 32(2):1378–1388, 2017. doi: 10.1109/TPWRS.2016.2572104.

Jizhong Zhu. *Optimization of Power System Operation*. 2nd edition, 2015. ISBN 978-1-118-85415-0.